9-24-2015 12:00 AM

Nanostructured Carbon Materials for Active and Durable Electrocatalysts and Supports in Fuel Cells

Adam Riese, *The University of Western Ontario*

Supervisor: Dr. Xueliang Sun, *The University of Western Ontario*

A thesis submitted in partial fulfillment of the requirements for the Master of Engineering Science degree in Mechanical and Materials Engineering

NANOSTRUCTURED CARBON MATERIALS FOR ACTIVE AND DURABLE ELECTROCATALYSTS AND SUPPORTS IN FUEL CELLS

(Integrated Article Format)

by

Adam Riese

Graduate Program in Mechanical & Materials Engineering

A thesis submitted in partial fulfillment
of the requirements for the degree of
Masters of Engineering Science

The School of Graduate and Postdoctoral Studies
The University of Western Ontario
London, Ontario, Canada

Abstract

Meeting the energy demands of the future will require a breadth of technologies and materials for generating and converting electricity. Increasing activity and reducing costs of electrocatalysts for fuel cells is among the most important challenges for the technology. With advances in nanomaterials there has been increased interest in creating novel catalysts with both high activity and excellent long-term durability. This thesis aims to understand how modification of nanostructured carbons can be used to improve the activity and durability of catalysts and supports for the oxygen reduction reaction (ORR). Using an integrating approach to synthesis, characterization, and electrochemical testing, it is shown that modifications via heteroatom doping and surface functionalization can improve upon the catalytic properties of nanostructured carbons. This work includes successful co-doping of nitrogen and phosphorus into carbon nanotubes for metal-free catalysis, improving Pt catalyst support properties of carbon black via ozone treatment, and evaluating popular test protocols for studying carbon corrosion in fuel cells.

Keywords

Nanomaterials, electrocatalysts, fuel cell, oxygen reduction, nanotubes, carbon black, carbon nanomaterials, renewable energy,

Co-Authorship Statement

For Chapter 3

PNCNT synthesis was done by A. Riese after initial help from Dr. Jian Liu. Biwei Xiao helped with Raman measurement. XPS analysis was done my Mark Biersinger at Western Surface Science. TEM was done by a Dr. Carmen Andrei at McMaster University.

For Chapter 4

NH_3 treatment, Pt deposition, gas sorption, SEM, and all electrochemical measurements were done by Adam Riese. Mohammed Norouzi Banis did ALD ozone treatment and performed XRD measurements, and with analysis of XANES. Other contributors to this work include: Yang Zhao for ICP analysis. Dr. Jian Liu for XANES experiments conducted at ALS. TEM was done by Dr. Carmen Andrei at McMaster University. XPS analysis was done my Mark Biersinger at Western Surface Science. CB and Pt/CB materials were provided by Ballard Power Systems, Inc.

For Chapter 5

A. Riese, D. Banham, S. Ye, and X. Sun, "Accelerated Stress Testing by Rotating Disk Electrode for Carbon Corrosion in Fuel Cell Catalyst Supports," *J. Electrochem. Soc.*, vol. 162, no. 7, pp. F783–F788, 2015.

All experimental work was carried out by A. Riese with the exception of Figure 1 which was referenced from another work (see Chapter 4). D. Banham and S. Ye guided the design of the study, supervised the work, and helped with interpreting results. D. Banham also aided in the writing of the manuscript. Supervision and consultation support was provided by D. Banham, S. Ye, and X. Sun.

Acknowledgments

Firstly I would like to acknowledge and thank Dr. Xueliang Sun (Andy). From our initial contact throughout my time at Western, he has been extremely supportive and steered me towards highly successful research. Dr. Sun's drive is admirable and his long-term vision for the group and for future energy applications using the latest nanomaterials has inspired me. Besides being a supervisor, I consider him an important mentor for me and a friend. My appreciation also goes to Kathy Li, without whom our group would not have achieved what is has to date. Thanks for being a mother-figure for us all and making sure we had everything we needed to get results.

Though the fuel cell group was small, I was lucky to be a part of a competent team including Dr. Niancai Cheng and Dr. Mohammed Norouzi Banis. My sincerest thanks to both of them. Niancai and I shared many long discussions about the state of fuel cells and he helped me to grow my skills in electrochemistry. And Mohammed, for his tremendous expertise in so many analysis techniques, and frequent guidance in interpreting results. Much of my research (and that of all our group members!) would be impossible without Mohammed.

I would like to extend my appreciation to Dr. Siyu Ye and Dr. Dustin Banham of Ballard Power Systems, Inc. I owe them both a great deal for the invaluable industrial experience I had at Ballard. Dr. Banham, in particular, mentored me directly and taught me the nuances of several electrochemical techniques which were instrumental to my work at Western, as well as extensive consultation and advice on research conducted both at Ballard and Western.

Finally, many thanks go to Biwei Xiao for Raman spectroscopy; Jian Liu for consulting, training on CVD, and experiments with ALD and synchrotron; Prof. Jianshe Wang for consultation and advice with experiments; Xia Li for support with gas-sorption analysis. Stephen, Craig, and Andrew for balance and a good laugh, all my friends and colleagues in Dr. Sun's group and, perhaps most importantly, to my girlfriend Anastasia for her love and full-time support.

Table of Contents

List of Tables

List of Figures

Glossary

ALD – atomic layer deposition

AST – accelerated stress test

C_O – concentration of oxygen

CB – carbon black

CE – counter electrode

CL – catalyst layer

CNT – carbon nanotubes

CV – cyclic voltammetry

D – diffusion coefficient

DOE – United States Department of Energy

E_0 – standard reaction potential

ECSA – electrochemically active surface area

EDS – energy dispersive X-ray spectroscopy

EXAFS – extended X-ray absorption fine structure

F – Faraday's constant

GDL – gas diffusion layer

HSC – high surface area carbon

LSC – low surface area carbon

MA – mass activity

MEA – membrane electrode assembly

MOR – methanol oxidation reaction

ORR – oxygen reduction reaction

PEM – proton exchange membrane *or* polymer electrolyte membrane

PEMFC – PEM fuel cell

Q – charge in Coulombs

RDE – rotating disk electrode

RE – reference electrode

SEM – scanning electron microscope

TEM – transmission electron microscope

VC – Vulcan carbon black

WE – working electrode

XAS – X-ray absorption spectroscopy

XPS – X-ray photoelectron spectroscopy

XANES – X-ray absorption near edge structure

XRD – X-ray diffraction

ν – kinematic viscosity of water

ω – rotation rate

1 Introduction & Literature Review

1.1 Proton Exchange Membrane (PEM) Fuel Cells

Fuel cells (FC) are energy devices that convert chemical energy directly to electrical energy. While several types of FCs exist, the proton exchange membrane (PEM) FC is the most popular and widely used because of its low temperature operation, scalability, and high energy density. These properties also make PEMFCs useful for applications in light-duty vehicles, transit vehicles, backup power generation, and consumer electronics. With increasing global demand for energy, and a shift towards cleaner, more reliable sources, PEMFCs have regained attention in the last several years because they have no operating emissions and the hydrogen used to power them can be renewably generated. Additionally, for automotive applications FCs have some key advantages over battery powered vehicles including longer range, faster refueling time, and simple vehicle integration. FCs, however, have struggled to gain traction in commercial applications as a result of their high cost, poor long-term durability, and lacking hydrogen infrastructure.

A PEMFC is a galvanic cell meaning it generates electricity by drawing electrons from a spontaneous chemical reaction [1], specifically the combination of hydrogen and oxygen to form water. The heart of a PEMFC is called the membrane electrode assembly (MEA). The MEA is a sandwich structure with several layers. In the center is the proton conducting PEM, which is a perfluorinated-sulfonic acid (the most widely used is called Nafion, from Dupont). Directly in contact with this, on either side, are the catalyst layers (CL) which typically consist of platinum (Pt) nanoparticles supported by high surface area carbon black, with a proton conducting ionomer dispersed throughout. On the outside of each catalyst layer is a gas diffusion layer (GDL) made of conducting carbon fiber, through which fuel and oxygen diffuse to the CL. A schematic of the working principle of a PEMFC, and a highlight of the electrode structure is shown in Figure 1-1. The PEM is on the order of 10-50 μm in thickness and the CL is generally no more than 2 μm thick [2]. The MEA is held between two plates called bipolar plates, which have small channels that direct the fuel and oxidant across the back of the GDL. Bipolar plates are made of graphite or metal alloys as they need to be good conductors and resistant to corrosion [3]. An MEA

between a pair of bipolar plates makes a single fuel cell. An FC stack consists of many cells placed together in series.

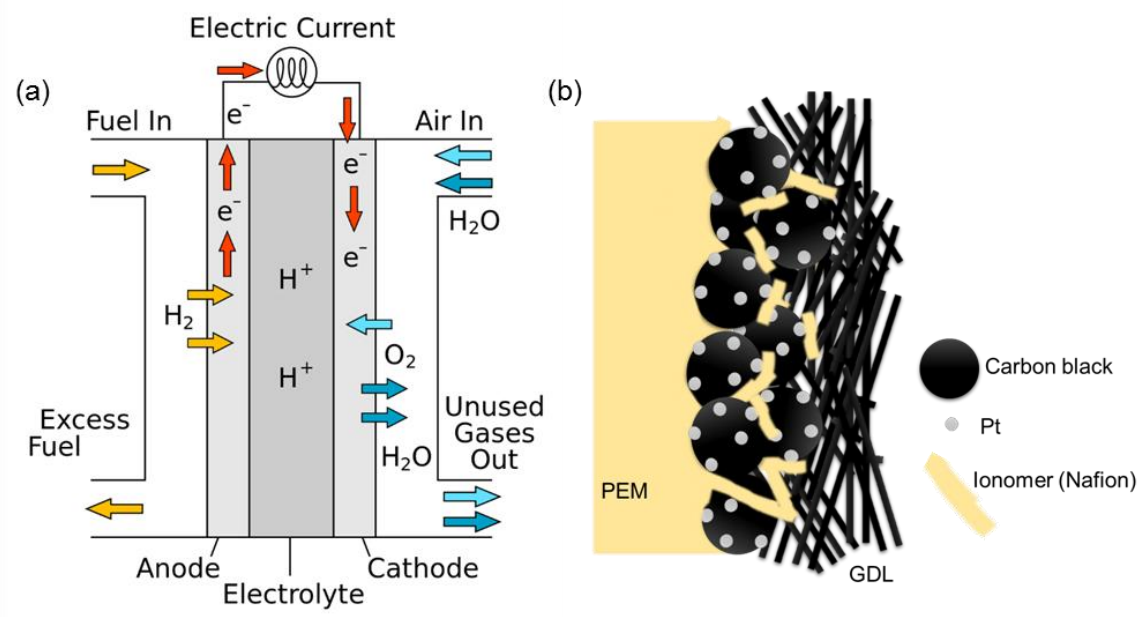

Figure 1-1. Schematic of PEMFC operation (a) and a schematic of an electrode structure showing the catalyst layer between the PEM and GDL (b). The GDL represents a carbon fiber structure that is commonly used.

At the anode, H_2 gas is introduced, passing through the GDL to the anodic catalyst layer. Here, the H_2 is split into a pair of H^+ ions, (i.e.: protons), and two electrons are split from the H_2 molecule. Because the PEM is a proton conductor, but not an electron conductor, H^+ ions pass through the PEM, while the electrons pass through an external circuit, where a load is connected. At the cathode, oxygen is introduced in the form of air, or pure O_2. As O_2 diffuses to the cathodic catalyst layer, it meets protons that have passed through the PEM and electrons that have passed through the external circuit. These combine at the so-called triple point to form water in a reaction known as the oxygen reduction reaction (ORR). The reactions occurring at the anode and cathode are hydrogen oxidation reaction (HOR) and ORR respectively. They are shown here:

$$\text{Anode: HOR} \qquad H_2 \rightarrow 2H^+ + 2e^- \qquad E_0 = 0\ \text{V} \qquad \textbf{(1-1)}$$

$$\text{Cathode: ORR} \qquad O_2 + 4H^+ + 4e^- \rightarrow 2H_2O \qquad E_0 = +1.23\ \text{V} \qquad \textbf{(1-2)}$$

While the anodic HOR reaction also requires a catalyst, its kinetics are orders of magnitude fast than the ORR so that it is not a limitation to FC performance. So, anode catalysts can have considerably lower Pt loading than the cathode catalyst [4].

The thermodynamic reaction potential for the ORR, that is, for PEMFC operation, is 1.23 V. However, a real PEMFC at open circuit potential (OCV) – the potential at zero current – will have a voltage closer to 1.0 V. These losses are due to parasitic reactions at each electrode resulting from fuel crossover and lowering the equilibrium electrode potential. The voltage difference between the theoretical reaction potential and the real potential at which the reaction proceeds is called the overpotential, η [1]. The overpotential is one of the fundamental challenges with FC technology, which would ideally have an output of 1.23 V, but operates closer to 0.7 V [5]. The reason for this are several types of voltage loss that occur in FCs. At potentials near the OCV, the losses are called activation overpotential, $\eta_{activation}$, and are due the sluggish reaction kinetics of the ORR. This is the main reason for using the Pt catalyst, as the overpotential from kinetic losses would otherwise be much greater without such a catalyst. In addition to kinetic losses, PEMFCs also suffer from ohmic losses and mass transport losses [4]. Ohmic losses, η_{iR}, occur across the entire range of operation for a FC and become more noticeable as the current density increases. These losses are a product of electrical resistances in the FC system, especially between the CL, GDL, bipolar plates, and current collectors. Ohmic losses become worse at higher current densities, following Ohm's law. Mass transport losses, η_{MT}, occur primarily at high current densities and result from the imperfect diffusion of reactants across the GLD to the CLs. For very high current densities a large volume of oxygen needs to be fed to the cathode. Getting this oxygen to the catalyst layer evenly and effectively is facilitated by the bipolar plate channel design, the GDLs, and increased feed pressure, but it is still difficult [4]. Figure 1-2 shows a polarization curve measured for a real PEMFC with the different loss regions highlighted. In addition to getting fuel and oxygen to the CL, there is water management to consider. Too much water will flood the MEA, blocking the gasses from reaching the CL. Too little water can cause the membrane to dry out, drastically decreasing its proton conductivity and leading to poor cell performance [2].

The current of an FC stack depends on the total area of the MEAs, which is given in A/cm^2. The stack voltage, meanwhile, scales with the number of cells, since any single cell is limited by the electrochemical reaction and overpotentials just described. Most PEMFCs operate at 0.6~0.7 V so that they can produce a meaningful current density (see Figure 1-2). For vehicles, FC stacks consist of up to 300 cells to achieve voltages of 200-300 V and total power around 80-100 kW [6].

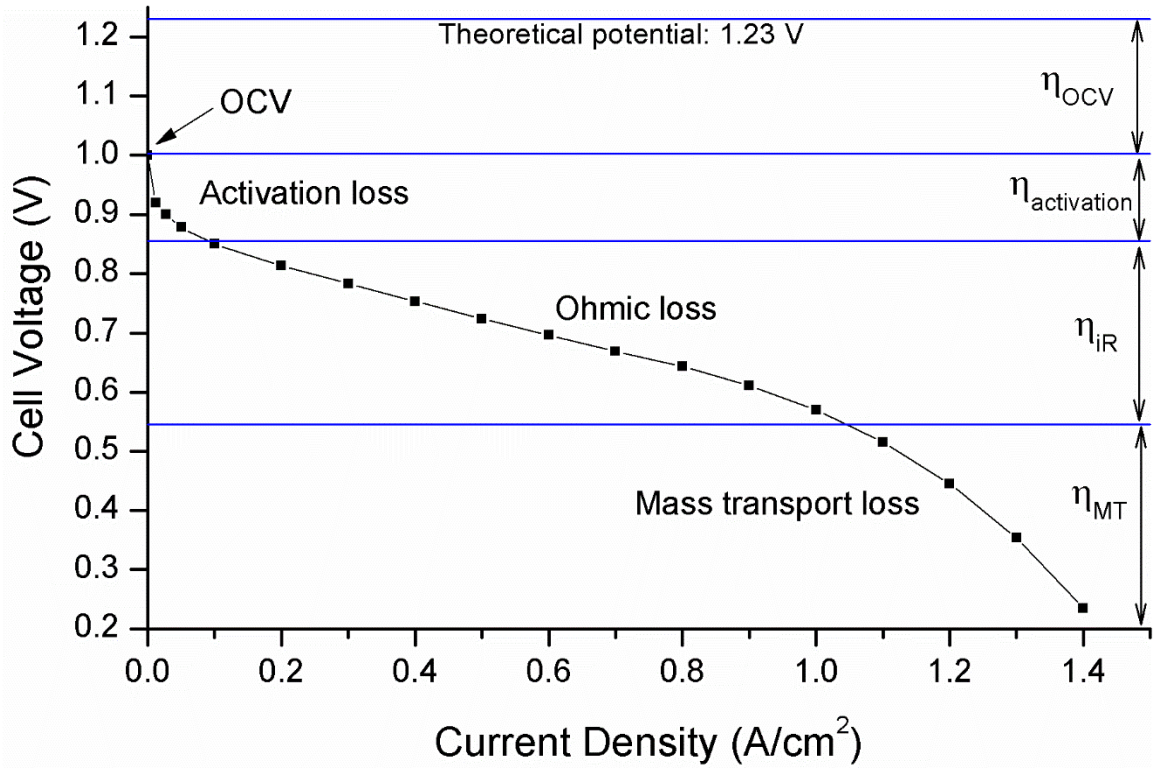

Figure 1-2. Polarization curve of a PEMFC under typical operating conditions showing regions of potential loss.

1.1.1 Catalyst Durability

Durability remains one of the primary challenges facing fuel cells today. The loss of performance with operation time is a serious barrier to the real-world use of PEMFCs where they must compete against much more mature technologies, such as gasoline engines in vehicles and diesel generators for backup power applications. Great strides have been made to improve the durability of FCs in the last decade as significant studies have been

conducted in this regard by industry, government, and academia. The United States Department of Energy (DOE) has been among the most active in terms of organizing and support FC research and studies published through their Fuel Cell Technologies Program have become valuable guides for researchers and industry [7]. Since the mid-2000s there have been durability targets for PEMFC durability. Currently, the targets for 2020 are 5000 hours of operation with <10% loss of performance for automotive applications and 60,000 hours operation for stationary power systems [7], [8]. In addition, the objectives include efficiencies of 65% and 45% for automotive and small-stationary uses.

Though there are a number of degradation pathways related to system or stack components, the main reason for loss of FC performance is degradation of the catalysts and membrane [9]–[11]. For the sake of this thesis, only catalyst and support durability is considered. Some of the main mechanisms of catalyst degradation include poisoning, Pt dissolution and Ostwald ripening, migration and agglomeration, and carbon support corrosion. Poisoning is a result of impurities in the hydrogen or air feeds such as sulfur dioxides which block catalytic Pt sites [12]. A similar loss of activity can be observed if species formed by the oxidation or decomposition of the catalyst support or membrane, such as CO, adsorb onto the Pt. Pt dissolution occurs via the repeated oxidation and reduction at the Pt surface which slowly erodes the nanoparticle surface. At potentials above 0.8 V, Pt oxide will form and this formation may involve the penetration of oxygen and even water. This results in Pt ions being dissolved in the electrolyte and a loss of performance. Ostwald ripening is migration of single atoms from one particle to another resulting from the trend to minimize Gibb's free energy in high-surface area system of particles. Agglomeration and migration occur due to electrode potential changes and the corrosion of the Pt support.

Support corrosion is one of the most common pathways to performance degradation as the electrode environment is very harsh for carbon. The presence of excess water, low pH, high electrode potentials, and elevated temperature all lead to a highly corrosive environment. Carbon corrosion is a result of oxidation to, primarily, CO_2:

$$C + 2H_2O \rightarrow CO_2 + 4H^+ + 4e^- \quad \textbf{(1-3)}$$

This can happen thermodynamically at potentials as low as 0.2 V, though it is relatively slow. However, at elevated temperatures this oxidation is increased, and in the presence of Pt can proceed quickly above 0.6 V [13]. A second mechanism, the direct oxidation to CO, also happens at elevated potential and includes the possibility of poisoning the Pt catalyst. Support corrosion is exacerbated during start-up and shut-down of the FC when voltages can nearly double the OCV, reaching as high as 1.8 V [14]. A number of system engineering strategies have been employed by FC manufacturers for mitigating this effect [10], but the development of a more durable support is still highly desirable.

1.1.2 Costs

FC cost is undoubtedly one of the most significant challenges impeding the commercial feasibility and success of the technology. The DOE has a 2020 target price of $40/kW and ultimate, long term target of $30/kW. They report current prices (2014 technology) as $55/kW based on mass production of 500,000 units per year and calculated using a bottom-up approach from component costs [7]. Meanwhile, Oak Ridge National Lab conducted a study with major PEMFC OEMS and estimates a current price of PEMFCs systems at $280/kW based on 20,000 systems per year [5]. Shown in Figure 1-3 is a breakdown of FC stack costs by component type at low and high manufacturing rates of 1000 and 500,000 units per year. These costs are calculated using the state-of-the art technology and information from the DOE and compiled by the Oak Ridge National Lab [5].

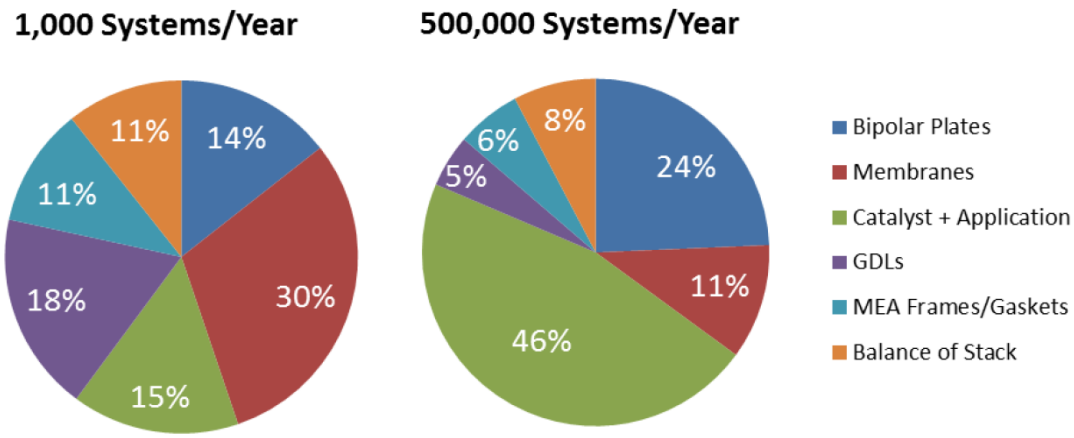

Figure 1-3. Fuel cell stack costs by component at 1000 and 500,000 systems per year manufacturing rate [15].

The current state of the FC industry is on the order of 1000 units per year. At this rate, costs are relatively evenly spread among various stack components, with membranes, GDLs, and catalysts, and gaskets (all part of the MEA) making up 74% of the costs. The catalyst is only 15% of the total stack at the current production rates. Meanwhile at 500000 units per year, the components of the MEA makeup 68% of the total, a slight reduction. However, the most startling fact illustrated by these charts is that at high production rates the catalyst constitutes 46% of total stack costs. Rather than decreasing with economies of scale, the cost of the catalyst for PEMFCs increases considerably when moving from 1000 to 500,000 units per year. In part, the apparent increase is due to the decreasing costs of all other FC components with large scale manufacturing, contrasted against the price of Pt, which will not decrease with scale, nor is it likely to decrease with time. Thus, although tremendous advances in FC technology and Pt reduction in particular has been achieved in the last decade [16], there is significant work ahead to achieve ultra-low Pt loading and ultimately move away from Pt containing catalysts. These steps are needed to meet the ultimate target price for PEMFCs of $30/kW.

1.1.3 ORR in Alkaline Media

Alkaline fuel cells (AFC) are similar to PEMFCs in that they use hydrogen and oxygen as fuel and create electricity through the HOR and ORR. In contrast to PEMFCs, hydroxyl ions (OH^-) pass from the cathode towards the anode, rather than protons moving from anode to cathode. Rather than a polymeric membrane, AFCs use a liquid electrolyte of potassium hydroxide (KOH) which has a very good OH^- conductivity. The reactions at the anode and cathode are HOR and ORR, as in a PEMFC, but in alkaline media the reactions are slightly different:

Anode: HOR $\quad 2H_2 + 4OH^- \rightarrow 4H_2O + 4e^-$ $\quad E_0 = 0.83$ **(1-4)**

Cathode: ORR $\quad O_2 + 2H_2O + 4e^- \rightarrow 4OH^-$ $\quad E_0 = 0.40$ **(1-5)**

Famously, alkaline fuel cells were used by NASA for a number of space missions including providing power for the Shuttles. They boast a higher current density than PEMFCs and have been shown to have good performance with very low loading of precious metal catalysts. McLean outlines two of the major challenges have hindered the terrestrial use of AFCs [17]. One is the liquid electrolyte which makes packaging difficult and presents problems in terms of maintaining the right electrolyte level. The more important and difficult challenge is their sensitivity to impurities in the gas stream, particularly CO and CO_2 (both of which are in air). These can react with the electrolyte to form undesirable products such as K_2CO_3, which quickly reduce cell performance. In the mid-2000s, a solid polymer based anion exchange membrane was proposed for AFC [18]. Anion exchange membranes offer several advantages including a solid-state FC stack, and good tolerance to carbonates compared with liquid KOH [19]. Direct alcohol fuel cells (DAFCS) use fuels such as ethanol (DEFC) and methanol (DMFC) instead of hydrogen. They often have an alkaline electrolyte, too, since anion conductivity is very important to their performance.

1.2 Electrochemical Half-Cell Evaluation of Fuel Cell Catalysts

1.2.1 Cyclic Voltammetry

Cyclic voltammetry (CV) is one of the most useful experimental techniques for studying electrochemical phenomena. It can be used to examine catalysis, redox reactions, plating and etching, and more. In the context of FCs, CV is extremely useful for studying the ORR under simulated operating conditions. This can be an effective method for screening new catalyst materials and understanding their catalytic activity, and durability.

CVs for FCs are done with a three-electrode electrochemical cell. This involves a cell containing the electrolyte, plus a working electrode (WE), reference electrode (RE), and counter electrode (CE). Potential is measured between the WE and RE, and current flows between the WE and CE. The RE is the point which the WE is measured against to determine the cell potential. The reference electrode must have a known potential, and be a species which is near impossible to polarize [1]. Some examples include the reversible hydrogen electrode (RHE), saturated calomel electrode (SCE), Ag/AgCl, Hg/Hg_2SO_4. These electrodes each have a known potential which is given relative to the standard hydrogen electrode (SHE). A reference electrode should be chosen whose reactants will not contaminate or poison the cell electrolyte or working electrode. For example, many groups studying Pt-based catalyst for fuel cells will not use an Ag/AgCl or calomel RE because of the dissolution of Pt with chloride ions [20]. In fact, many groups use perchloric acid ($HClO_4$) instead of H_2SO_4 electrolyte since it has been shown that the bisulfate ions in the latter adsorb to Pt and reduce the ORR performance and limiting current [21]. For any reaction taking place at the WE, an opposing reaction will be taking place at the CE, as dictated by the current flow between the two. The CE should be a material that will not produce any electrolytic products that might interfere with the WE [1]. Typically Pt or graphite are chosen. An important consideration is that the surface area of the CE should be much larger than the area of the WE, to ensure that the reaction (and current flow) is never limited by the CE. Often a Pt wire or Pt mesh is used for this reason.

Understanding the characteristic of CV curve for Pt catalysts is important for identifying trends and comparing several samples of interest. A typical CV of a Pt/C catalyst measured at room temperature in N_2 saturated 0.5 M H_2SO_4, is shown in Figure 1-4. The CV was recorded at 20 mV/s from 0.05 V to 1.0 V. In the plot are highlighted a number of important features which are characteristic of catalysts studied in this thesis. At the lower potential region, from roughly 0.05-0.4 V are the hydrogen adsorption and desorption regions. Here, a current is generated at the WE by the adsorption of hydrogen on the Pt surface. This region is often referred as the hydrogen under-potential deposition (H_{UPD}) region, where H_{UPD} occurs at potentials above the $H_2 \rightarrow 2H^+ + 2e^-$ standard reaction potential ($E^0_{H^+/H_2} = 0\ V$) [22]. The highlighted peaks correspond to certain crystal faces of Pt, (111) and (100), on which hydrogen adsorbs at slightly lower and higher potentials, respectively.

In the region from 0.4~0.7 V, there is a low current density region known as the double layer region. Here, the charge arises from the capacitance created at the electric double layer of the electrode surface. For an electrode at some non-zero potential, oppositely charged ionic species in the electrolyte solution will be attracted towards the surface. Only a certain number of these ion will physically reach the electrode surface. This leaves a residual electrostatic charge at the electrode as a single layer of ionic species cannot compensate for this electrode charge. Thus, more ions from the solution will move towards the electrode surface, held at long range by the electrostatic force. The combination of that first, adjacent layer of ions, plus the longer range species which are pulled in, is referred to as the electric double layer, and is a function of the electrode surface area and potential, plus the type of ionic species in the electrolyte [1]. This region will show a higher current density with increasing electrode surface area.

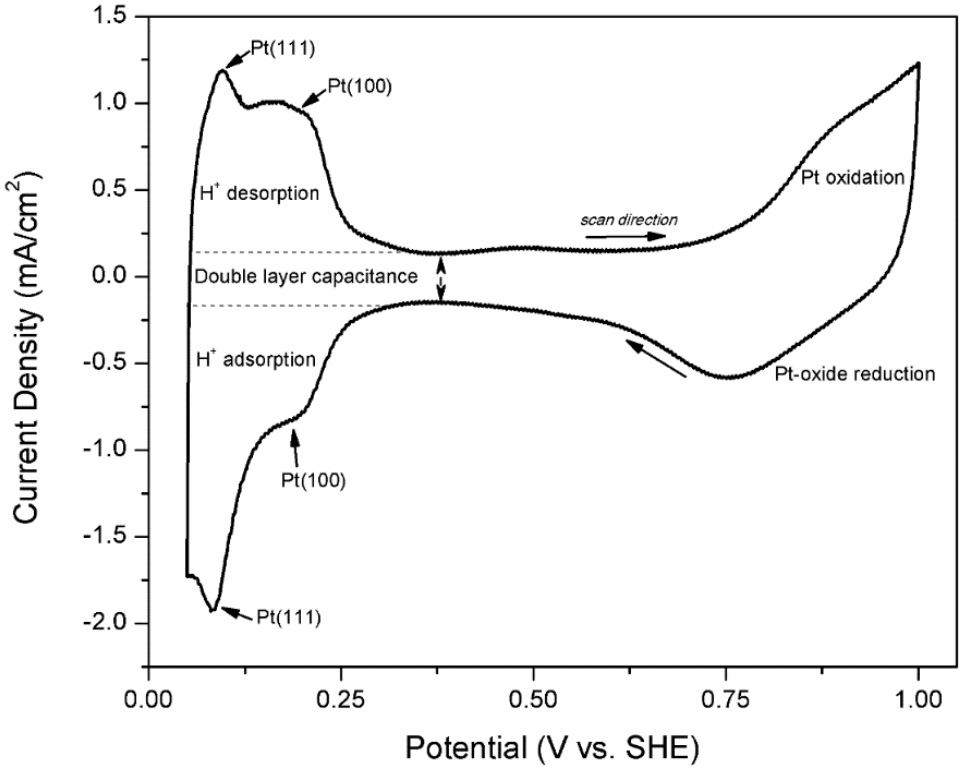

Figure 1-4. A typical CV curve of a Pt/C catalyst in 0.5 M H_2SO_4. Labels indicating several regions of the curve where formation of electrochemical species creates easily identifiable peaks.

The electrochemical surface area (ECSA) is an important metric for quantifying and comparing catalysts. It refers to the mass normalized surface area that is available for participating in an electrochemical reaction; in this case, that will be active in catalyzing the ORR reaction. Determination of the ECSA of Pt can be done in several ways, but perhaps the most common is using the by calculating the charge in the H_{UPD} region. Integrating the curve from 0~0.3 V (0~0.4 in $HClO_4$), and using the double layer region as a baseline, will give a total charge, Q, in Coulombs. Using a known quantity of 210 μC/cm^2, representing a monolayer of adsorbed hydrogen on the Pt surface [23], we can determine the total electrochemically active surface by:

$$ECSA = \frac{Q_{H_{UPD}}\,(C)}{210\,\frac{\mu C}{cm^2} * Mass_{Pt}\,(g)} \qquad \textbf{(1-6)}$$

A couple of important assumptions that are made for this method. The first is that a perfect monolayer of hydrogen with total Pt coverage is adsorbed. Further it should be noted that the value of 210 μC/cm^2 is an average for an assumed polycrystalline Pt surface. In reality each single crystal face of Pt will have different hydrogen adsorption properties, as mentioned earlier. Another assumption is that a total charge transfer occurs between the H and Pt. In fact, it is likely that the charge transfer is not perfect and thus some error exists in the method [23]. Nevertheless, using the H adsorption region for determination of ECSA is effective for quantifying the active surface area of catalysts and has been widely accepted in the community and shown to be reproducible across multiple labs [24], [25].

As the potential is scanned above 0.8 V in the forward direction, another large peak appears. This peak is a result of the formation of Pt oxides. The reaction $Pt + \frac{1}{2}O_2 \rightarrow PtO$ is the main oxide formation, however some PtO_2 can also form. [2]. Using an upper potential limit (UPL) of 1.0 V limits the formation of oxide, which results in a smaller ORR peak around 0.8 V in the negative direction. It is also common to scan up to a UPL of 1.2 V which results in more complete formation of Pt oxide. The size and position of the ORR peak under N_2 conditions is important although performing a CV in O_2 saturated electrolyte with a rotating disk electrode (RDE) is a more meaningful test of the ORR activity.

1.2.2 Determining ORR Activity by Rotating Disk Electrode (RDE)

Thin-film RDE is a particular type of CV measurement which uses a spinning electrode to increase the diffusion of reactants to the electrode surface. An RDE electrode is structured with a flat disk of electrode material surrounded by a sheath of polytetrafluoroethylene (PTFE) material. The electrode is typically Pt, Au, or glassy carbon. The electrode is connected to a shaft inside a rotator which can rotate at a set speed. During rotating, a vortex of electrolyte solution flows towards the electrode surface, ensuring an excess of reactants is available. At a given, rotation rate, then there is a theoretical maximum current density that can be achieved for a given experimental setup. A very thin layer of electrolyte directly adjacent to the catalyst layer, called the Levich layer, will rotate with the electrode. The result of this is a steady state at the catalyst layer

surface with the current limited by the diffusion of O_2 across the Levich layer [1]. That limiting current is described by the Levich equation:

$$i_{lim} = 0.201nFAD^{\frac{2}{3}}\nu^{-\frac{1}{6}}C_O\omega^{\frac{1}{2}} \quad \textbf{(1-7)}$$

Here, n is the number of electrons transferred in the reaction, F is Faraday's constant (96458 C/mol) A is the electrode area in cm^2, ω is the rotation rate in RPM. C_O is the concentration of oxygen in the electrolyte in mol/cm^3. D is the diffusion coefficient and ν the kinematic viscosity of the reactant in the electrolyte (both in cm^2/s). The value for the kinematic viscosity of water, 0.01 cm^2/s, is often used for aqueous electrolytes [26]. The values of each parameter for our testing conditions is given in Table 1-1.

Table 1-1. Parameters for the Levich equation for ORR at 25°C, 1 atm.

Electrolyte	Parameter	Symbol	Value	Units	Ref.
0.5 M H_2SO_4					
	Solubility of O_2	C	1.18×10^{-6}	mol/cm^3	[27]
	Diffusion Coefficient	D	1.4×10^{-4}	cm^2/s	[27]
0.1 M KOH					
	Solubility of O_2	C	1.10×10^{-6}	mol/cm^3	[28]
	Diffusion Coefficient	D	1.4×10^{-4}	cm^2/s	[28]

A typical ORR curve for Pt/C in acidic electrolyte is shown in Figure 1-5. Recalling Figure 1-2, the FC polarization curve, the ORR plot is analogous although with the axis switched. The region from 0.8-1.0 V is the kinetic region, where activation losses occur. This is an area of particular interest as the activity of a catalyst is generally measured here, around 0.9 V vs RHE. The onset potential is an often cited metric when referring to ORR curves. Onset potential is the potential at which current density begins to increase as the reaction begins. A higher onset potential indicates that the reaction has a lower overpotential, which is preferred. The linear portion from 0.6~0.8 is a mixed kinetic and diffusion regime and the plateau from 0~0.6 V is known as the diffusion limited region. In this region the limiting current (or Levich current) is determined by parameters in the Levich equation, as discussed.

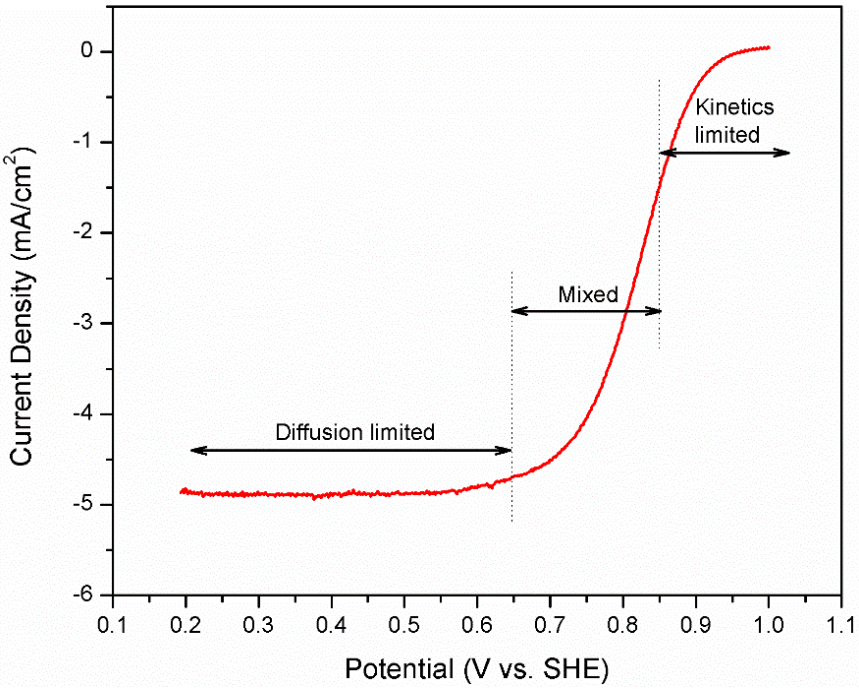

Figure 1-5. ORR polarization curve of Pt/C catalyst recorded using RDE at 1600 RPM in O_2 saturated H_2SO_4 at 25°C, scan rate 20 mV/s. The kinetic and diffusion limited regions are highlighted on the curve.

The RDE method is inherently complicated and thus some amount of error can be expected between measurements and between labs. The community has, to date, accepted a number of norms for measuring Pt-based catalyst, though it remains difficult to compare results from one lab to another. That is changing, however. Researchers at several national labs in the US, as well as the Army Research Center have been working towards standardizing RDE methods so that meaningful comparisons of ORR activity can be made from one lab to another. A small group has made considerable contributions in the last five years, in this respect. The impacts of catalyst ink composition [29] and of the thin-film drying method [30] have been explored. In an effort towards unified standards, the same groups have reported best practices for RDE measurements, benchmarked the performance of commercial catalysts, and demonstrated good repeatability [24], [25], [30], [31]. The DOE has also hosted several webinars on this in 2013 and 2014 [32], [33]. These efforts are an encouraging sign for the FC electrocatalyst research community.

1.3 Nanostructured Carbons for Electrocatalysts & Supports

For decades, fuel cells have utilized the unique properties of nanoscale materials in the catalyst layer. In particular, the high surface to volume ratio of such make them excellent for this application, where mass transport of reactants in different phases is critical to overall performance. Carbon is one of the most abundant elements on earth. Carbon nanomaterials are excellent candidates for electrocatalysts and supports not only for their high surface area, but for their electrical conductivity, their ability to support metal catalyst particles, and their potential to be modified for specific functionality. In this section, several families of nanostructured carbon materials are reviewed including a brief discussion of synthesis methods, typical characteristics, and advantages or disadvantages for use in catalysts and supports.

1.3.1 Carbon Black

By far the most common FC catalyst support material is carbon black (CB). Carbon black is a general name for a family of carbon materials such as acetylene black, furnace black, and more. Besides being used as a fuel cell catalyst support material, CB is used as an additive in rubber, pigment in paints and inks, and as a polymer additive. CBs are synthesized via several methods but most popular is the partial combustion of oil with natural gas followed by quenching in water [34], [35]. Among the most popular types of CB are Vulcan from Cabot Corp and Ketjenblack from AkzoNobel. One of the most attractive reasons that CBs continue to be used in FC catalysts is their low cost; with which more novel nanostructures like CNTs and graphene still cannot compare.

CBs can have a wide range of surface areas from 15-2000 m^2/g. They consist of primary particles in the range of 5-30 nm which form larger agglomerate units with dimensions on the order of tens of microns. A scanning electron microscope (SEM) image of a high surface area CB (800 m^2/g) is shown in Figure 1-6. The images, at 50000x and 100000x magnification, show the large agglomerates and the joined primary particles of roughly spherical shape. For use in FC catalysts, CB has a host of properties that make them good support materials including electrical conductivity, high surface area, and low

cost. Furthermore, their agglomerate structure allows for both homogenous dispersion of catalyst particles and accessible contact with ionomer in the catalyst layer [2]. The chemical structure of CB includes many small graphitic crystal phases several nanometers in dimension. Their surface may have dangling hydrogenated bonds or oxygen containing groups due to their synthesis conditions [36], and contamination from sulfur and nitrogen is not uncommon, resulting from the oil used to make CB.

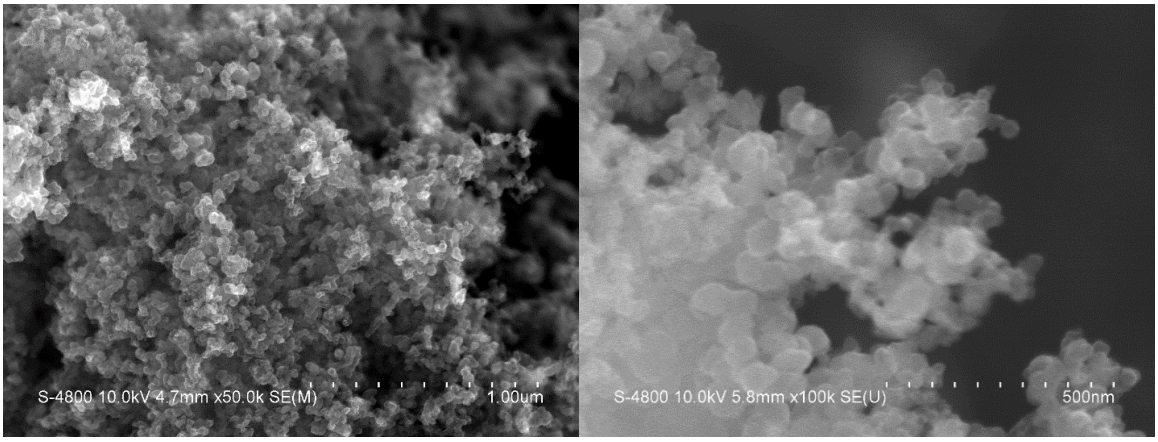

Figure 1-6. SEM image of high surface area CB showing aggregates and primary particles.

Although CB possesses a number of excellent qualities for use as a catalyst support, there are some significant drawbacks to its use. The most important challenge for CBs is their poor corrosion resistance. As discussed in the preceding section, a FC catalyst layer is a highly corrosive environment with temperatures as high as 120°C, low pH, and electrode potentials well above 0.6 V. Though CB contains small graphitic phases, overall it has a highly amorphous structure with a surface that is prone to corrosion via oxidation [37]. Graphitization by extended high temperature treatment is known to be an effective method of hindering carbon corrosion by oxidation [2].

1.3.2 Carbon Nanotubes

Carbon nanotubes (CNTs) are an allotrope of carbon; essentially a rolled up sheet of graphene. CNTs are the 1-dimensional manifestation of sp^2 carbon, with the 0D and 2D versions being fullerenes and graphene, respectively. The first report of CNTs was by IIjima in 1991 [38], although CNTs were originally conceived and may even have been

observed years before then [39]. CNTs appear in several forms including single walled (SWCNT) and multi-walled (MWCNT) and can have a number of orientations depending on which bond configuration lies in the axial direction. Each of configuration possesses slightly different characteristics as a result of their physical form. For example, SWCNTs have metallic-level conductivity and theoretical strength higher than steel. In general, all CNTs exhibit either metallic or semiconducting electrical conductivity which has made them highly attractive for a number of applications in sensing devices and microelectronics [40]–[42].

CNT synthesis falls under three main categories including laser ablation, arc-discharge, and chemical vapor deposition (CVD). Laser ablation and arc discharge both involve heating of graphite to several thousand degrees Celsius, through a high voltage arc or high energy laser, and collecting the nanotubes from the soot produced [43]. These two methods can produce extremely thin SWCNTs, but their orientation is random and the process always yields a variety of other carbon types at the same time. CVD has become more popular because of the excellent control over the CNT growth and relative ease of scale up. CNTs are grown via the decomposition of a vapor phase carbon precursor with the help of a transition metal catalyst which helps to nucleate the growth [43], [44]. CVD growth requires temperatures in the range of 500-900°C and a carbon source and metallic catalyst. Carbon sources are often gaseous hydrocarbons such as methane, ethane, or carbon monoxide [45], as well as many other solid and liquid precursors [44]. Metal catalysts for CNT growth can include Ni, Fe, and other transition metals. Their size and shape have a strong effect on the morphology of CNTs [46], [47]. Growth from catalyst particles proceeds via base-growth or tip-growth mechanisms where the catalyst stays at the substrate or moves along at the top of the tube, respectively. This will depend largely on the strength of interaction between the catalyst particle and substrate. Base-growth of CNTs is shown schematically in Figure 1-7, along with an SEM image of MWCNTs grown via CVD on carbon fiber. SWCNTs can be produce by CVD method but require very small and well dispersed catalyst particles [48]. In addition to conventional CVD, plasmas enhanced CVD (PECVD) and microwave-assisted PECVD have been used to grow CNTs [49]–[51]. The use of plasma and microwaves enhance the growth rate and alignment of CNTs.

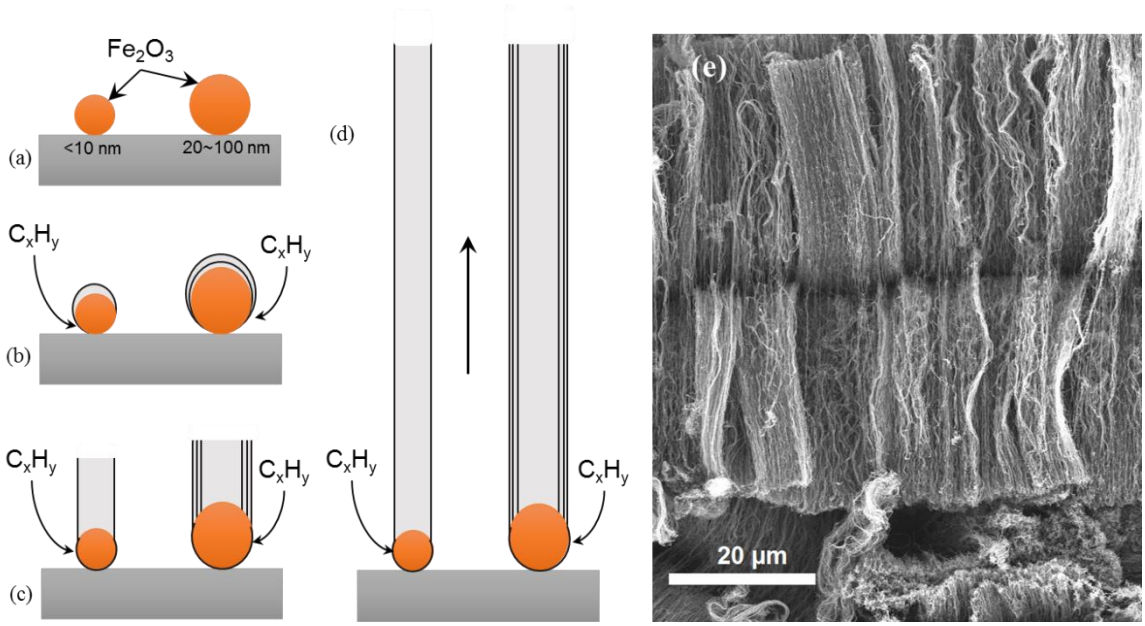

Figure 1-7. (a-d) Base-growth of CNTs (SW and MW) via CVD. (a) Fe catalyst particles are deposited on the substrate. (b) The catalyst becomes saturated with carbon from the decomposition of hydrocarbon gas on the particle. As they become saturated, nucleation of the CNT begins with a layer of graphitic carbon around the catalyst particle. (c) Continued influx of carbon precursors results in the growth of the CNT. On the larger catalyst, multiple layers are formed and grow as MWCNT. (d) CNT growth continues as long as carbon is provided and reaction conditions are maintained. (e) Aligned MWCNTs grown on carbon paper using ferrocene as catalyst precursor. The dark horizontal line is the axis of the carbon fiber. CNTs have grown normal to the fiber.

CNTs have become increasingly popular in research and some commercial application. Mass production of various lengths and diameters has been achieved so that CNTs are available for purchase from myriad suppliers. Besides being used in logic, memory, and sensing devices, CNTs have been used for FCs for several years. In one capacity, CNTs are being used as an electrode micro-porous layer (MPL). The MPL is the side of the GDL adjacent to the CL. It has smaller and more disperse pore structure than the GDL as it is meant to evenly distribute fuel gases across the CL, at the micron scale. Besides this, CNTs have bene studied at length for use as catalyst supports and metal-free catalysts. It is well known that the good electrical conductivity, high surface area, and graphitic nature of CNTs make them excellent candidates for catalyst supports [2], [16].

1.3.3 Graphene

Graphene is a 2-dimensional material comprised of sp^2 hybridized carbon atoms, first physically discovered in 2004 [52]. Graphene has become very popular due to its remarkable electrical conductivity, mechanical strength, and thermal conductivity. It has a super-high specific surface area (theoretically >2600 m^2/g) which makes graphene excellent for facilitating chemical reactions; although it's relatively inert basal plane surface means that further functionalization is necessary for many applications. Graphene has been used in a variety of applications including composite materials [53], fuel cell catalysts[54], batteries [55], and more. In a broad sense, two categories of graphene materials may be classified. The first is pristine, single layer graphene. This type can be synthesized via mechanical exfoliation [52], or by chemical vapor deposition on a metal catalyst substrate [56]. The second class of graphene materials is often referred to as graphene nano-platelets (GNP) or reduced graphene oxide (rGO). This material is mostly synthesized via intercalation or oxidation of graphite followed by exfoliation and/or reduction, yielding small particles of graphene sheets with 2-100 layers stacked together and lateral dimensions on the order of 0.1-100 μm [57]. The properties of GNPs are not as remarkable as pristine graphene, but it can be made at large scales of tons per year [58].

Until recently, graphene was plagued by the fact that production in large quantities is very difficult and expensive. In the recent years, after significant investments and efforts by academia, industry, and government, a number of processes have emerged for mass production of graphene. Roll to roll processing has allowed for continuous CVD synthesis of pristine graphene and its facile transfer from metal substrate to usable polymeric or other substrates [59]. Researchers at Sony reported single layer graphene of more than 100 m in length [60]. Similarly, GNPs have been produced in large quantities by various methods including high shear mixing [61], and by exfoliation and reduction of graphene oxide (GO) [62].

1.4 Modified Carbon Nanomaterials as Catalyst Supports

Heteroatom doping has been used in a variety of nanostructured carbon materials, including graphene and CNTs, to enhance their electrical, chemical, and mechanical properties. Among the most common dopants are nitrogen, boron, sulfur, and phosphorus. N-doping has been by far the most common in the last decade due to the relative ease of synthesizing N-doped carbons and its beneficial effects. Doping with atoms such as B, S, and P can also have notable effects on the carbon structure. The creation of charged sites, the stretching of carbon bonds, and the disruption of local electronic structure in the otherwise neutral sp^2 lattice can enhance ORR activity and binding of metal particles. These phenomena are discussed here in the context of several types of modification, along with a brief review of synthesis methods.

1.4.1 Oxidizing Treatments

Oxygen functionality on carbon surfaces has been studied for several decades and its effect on both metal catalyst particle dispersion and on ORR activity of the carbon itself has been promising. The earliest reports are with CB or activated carbon, but CNTs and graphene have been the subjects of similar studies. Oxidation with a strong acid is among the most common methods of introducing surface groups [36], [63], [64], but treatment with ozone [65]–[67], and annealing in air [68] have also been reported. There are a variety of surface oxides that may form including carboxyl, hydroxyl, lactones, ethers, ketones, quinones, and more [36]. The presence of any particular species will depend on the carbon used and the type of oxidation. It has been shown that presence of surface oxides can modify the pH of the carbon surface, which may have an impact on the deposition of metallic particles on the surface [63], [65], [68], [69]. In fact, several reports have shown that surface oxides improve the dispersion of metallic nanoparticles [63], [67], [70], [69]. Additionally, some oxygen containing species can improve the catalytic activity of carbon to ORR and other reactions [69], [71], [72]. One of the main drawbacks of increased oxygen-containing surface groups is that carbon corrosion at elevated potential and temperature can be intensified as a result.

1.4.2 Nitrogen Doping

Nitrogen has received by far the most attention as a heteroatom dopant in carbon. There has been a growing body of literature published, focusing on synthesis, theoretical studies, characterization, and applications [73], [74]. N-doping is an excellent way to tune or modify the properties of carbon nanostructures. The inclusion of N-sites in the carbon lattice effects the electronic structure of the material and increases the activity around the dopant sites. Much of the change in the properties of N-doped carbons are associated with the difference in electronegativity between nitrogen ($\chi = 3.05$) and carbon ($\chi = 2.55$) [75]. This difference creates a polarized charge density within the sp^2 bonding structure. N-dopants also bring an additional electrons to the carbon lattice which promotes π-π bonding. There have been several theoretical studies on the electronic effects of N-doping in graphene, though with conflicting results [73]. Some have suggested that the electron donating nature of N dopants is the reason for excellent ORR activity in N-doped carbons [76]–[78], contradicting the explanation of difference in electronegativity between N and C. N-graphene and NCNTs have been used as metal catalyst supports [79]–[81], and some have calculated that the changes in electronic structure resulting from N dopants can double the binding energy of Pt–C bonds [82].

The ways in which N-dopants exist in a carbon lattice is of significant interest and has been studied extensively. Commonly, three types of N-dopants are referred to. These are pyrrolic, pyridinic, and graphitic type N. Pyrrolic and pyridinic N are bonded to two carbon atoms in five and six sided rings, respectively, and exist at edge sites within the carbon lattice. Graphitic nitrogen is substitutionally bonded to three carbons within the sp^2 structure, away from edges. Depending on the type of synthesis, one type of N species may be more prevalent than others. Because of their bonding nature, pyridinic and pyrrolic N are more reactive than graphitic N. In addition to the three species mentioned, other N-type bonding can also occur though they are referred to infrequently in the literature and are assumed to make up a small percent of the doped species in N-graphene. Figure 1-8 shows the various types of N-dopants as they might exist in an sp^2 carbon lattice.

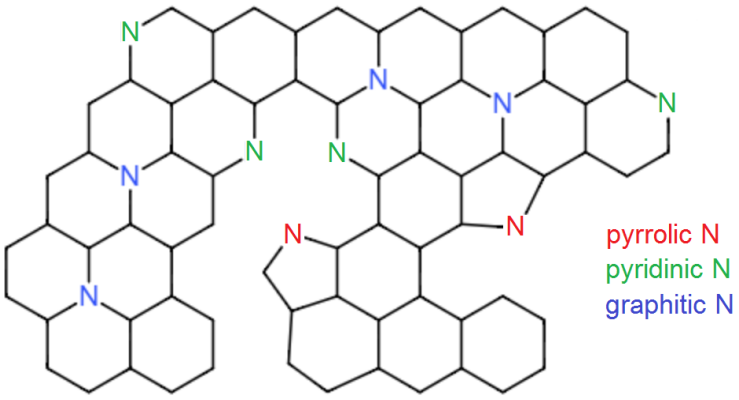

Figure 1-8. N-type dopants in sp^2 carbon

N-doping has proven useful for improving both the activity and durability of ORR catalysts [83]. The activity of N-doped carbon is greater than that of unmodified carbons for a number of reasons including the change in spin and charge densities in the vicinity of the dopants [84]. Compared to graphene or other un-doped carbon supports, N-graphene reduces the energy for O_2 dissociation, and destabilizes the ORR intermediate species on the Pt surface, pushing the reaction forward [85]. In a review by the O'Hayre group [83] they summarize the reaction pathways of ORR on N-doped carbons. In addition to the direct enhancement of ORR, N-dopant sites act as good anchoring sites for Pt nanoparticle and the strong bonds between the doped support and catalyst particles prevents migration and aggregation that otherwise lead to loss in activity. This was shown by theoretical calculations by Groves et al, who concluded that the "increase in binding energy is proportional to the number and proximity of N atoms to the C–Pt bond and is a result of the N atoms locally destabilizing the delocalized double bond present in the pure C structure" [82]. The inherent properties of nanostructured carbon, and the added functionality of N-dopants such as modified electronic structure and enhanced activity near N-sites make N-doped carbon excellent materials for electrochemical devices.

Nitrogen doped carbon nanotubes (NCNTs) are an increasingly popular N-doped material. Among the first to synthesize NCNTs were Stephan in 1994 [86] and Sen in 1997 [87]. Synthesis is often done via pyrolysis of a nitrogen and carbon containing complex with some catalyst particles. Combinations could include iron(II) phthalocyanine [88], or Fe(III)(acetylacetonate)$_3$, acetonitrile, and tetrahydrofuran [89], or ferrocene and imidazole

[90]. Liming Dai, one of the leading researchers in the field, published a report in Science [88] on NCNT arrays used as catalysts in both alkaline and acidic media, claiming that they could achieve higher current density in alkaline FCs than even a Pt/C catalyst. They also suggest that pyrrolic N-dopants result in more positive neighboring carbons than pyridinic N. Saha et. al. grew NCNTs on carbon paper and showed that Pt nanoparticles dispersed better on NCNTs than on CNTs and that the performance of the NCNT supported catalyst was superior in RDE and MEA testing [89].

Single layer Nitrogen-doped graphene was first synthesized in 2009 via CVD growth with ammonia [91]. Since then, N-graphene has been studied as a Pt catalyst support in a number of reports. Some of have shown that Pt deposited on N-graphene is more uniform than on un-doped graphene, and demonstrated its durability by imaging using TEM before and after durability cycling, which shows minimal change in particle size [92]. The Sun group used ZrO_2 nano-cages to anchor Pt nanoparticles even more strongly to an N-graphene support, which resulted in remarkable stability [93]. Geng et al synthesized N-graphene material with a flower-like morphology and deposited Pt nanoparticles via impregnation [94]. They studied the durability of that catalyst compared with a commercial Pt on Vulcan carbon (Pt/C) catalyst and found that commercial Pt/C and Pt/N-graphene to had dropped to 32% and 50% of their initial values, demonstrating the improved durability of Pt/N-graphene. Jafri et al [81] used plasma treatment to doped graphene to an N concentration of 3 at.%. Pt nanoparticles were deposited by a reduction with $NaBH_4$ and a MEA was prepared using Pt/N-graphene as the cathode catalyst. They found the power densities of Pt/N-graphene and Pt/graphene to be 440 and 390 mW/cm^2, respectively. N-graphene also performs well as a metal-free ORR catalyst in alkaline conditions [95]. Other non-precious catalysts have also been deposited onto N-graphene for ORR in alkaline solution, such as Mn_3O_4 Fe, Co, and Fe–CO [96], [97]. These materials showed excellent activity and durability compared with conventional Pt catalysts. For alkaline solutions, though, N-graphene is most often proposed as a metal-free catalyst, where it's tremendous catalytic activity has been well documented.

1.4.3 Phosphorus Doping

Phosphorus is commonly used as an *n*-type dopant in materials such as silicon. As a dopant in carbon, its excess valence electrons make it interesting for modifying electrical properties. P can be more difficult to incorporate into a carbon lattice due to its significantly larger size compared with the carbon and with nitrogen or boron, for example. Synthesis of P-doped CNTs has been reported as early as 2005 [98] via CVD with triphenylphosphine (TPP). Since then P-doping of carbon nitride [99], graphite [100], [101], graphene [102]–[104], and mesoporous carbon [105] have been reported. Concentrations of 1-2 at. % P are most common in the literature [90], [105], [106].

P-doped species may exist in a number of bonding configurations consisting of different P-C and P-O bonds [103]. Compared with other atoms such as sulfur, phosphorus dopant atoms come with a wide spread of the lone pair states, and the lowest unoccupied molecular orbital (LUMO) state is more distributed which increases the reactivity, an attractive feature for ORR enhancement [107]. Modelling of P-doped nanotubes have shown that P-C bonds are greatly stretched compared to C-C bonds which introduces considerable strain in the sp2 rings [109]. Similarly, P-graphene would include an out-of-plane deformation caused by the presence of the P atoms. The excess lattice strain caused by this deformation also increases reactivity of the site.

RDE tests of P-graphene and graphene demonstrate the improved catalytic efficiency of the doped material towards ORR in alkaline media. In alkaline media, P-doped graphene and CNTs have been successfully demonstrated as metal-free catalysts [101], [105], [106] Even at relatively low P-doping levels, P-CNTs have demonstrated better ORR activity than even Pt/C catalysts in 0.1 M KOH [106]. Pt nanoparticles supported on P-doped mesoporous carbon have also shown excellent performance for methanol oxidation [110], and ORR in acidic media [111], [112]. Some have suggested that the P-sites act as good anchoring sites for Pt nanoparticle dispersed on P-CNTs and shown that their performance is even better than Pt/C and Pt/CNTs [113].

1.4.4 Sulfur, Boron Doping

Sulfur doping has become perhaps the most studied following nitrogen. There have been a flurry of reports published on the subject, especially since 2012. Synthesis of S-graphene has been done in a variety of ways. Thermal treatment of GO in a solid state reaction is popular using benzyl disulfide [114] or phenyl disulfide [115] as the dopant precursor. Also commonly reported is the use of a gas phase dopant such as CS_2 [116]. The large difference in electronegativity between N, B, or P and carbon creates significant charge density in local doping regions. In the case of sulfur and carbon the difference in electronegativity is relatively small, suggesting that other factors lead to the increased activity observed with S-graphene catalysts. Good catalytic properties of S-doped carbon have been attributed to the large size of sulfur compared with carbon and N creates strain and defect sites in the carbon lattice, and to a difference in the spin density of sulfur [116], [117]. S-graphene has been found to have higher metal-free ORR activity in alkaline solution than graphene, with both the onset potential and total current density being higher for the doped sample [114]. Chen's group report improved performance of Pt catalysts when using S-graphene as a support material [115]. They conducted both experimental and computational investigations as to the effect of S doping in graphene for ORR catalysts. Compared to Pt/graphene and Pt/C catalysts, Pt/S-graphene had higher current density and dramatically improved durability, retaining 87% of its ECSA after durability testing via RDE.

Boron is widely used as a dopant atom in silicon based electronics where its electronic structure makes it perfect for creating *p*-type semiconductors. Its small size also lends itself to facile doping into an sp^2 carbon lattice. Synthesis of B doped carbon usually involves a solid state reaction of GO with boric acid (B_2O_3) though gaseous dopant precursor materials such as BCl_3 have also be used [118]–[120]. Reported dopant levels are on the order of 1-5 at. % [120]. The lower electronegativity of B creates a positively charged site on the B atom. O_2 molecules which hold a slightly negative charge are therefore chemisorbed directly to the B dopant sites [121]. This promotes the ORR and helps explain the good activity of B-doped carbon catalysts. In the case of graphene prepared by reduction or exfoliation of GO, it should be expected that there are residual

oxygen species on the graphene and thus, oxidized states of B will account for some of the overall B content. While few experimental test have been done with Pt on B-graphene, DFT studies show that Pt absorption is increased significantly when in very close proximity to the dopant atom [122], suggesting that B-graphene could also be a highly durable catalyst support.

1.4.5 Multi-atom Doping

As heteroatom doping gained popularity among researchers and the remarkable performance of these materials became clear, it was only natural that co-doped carbons should be explored. With the prospect of adding functionalities from two different dopant atoms, a number of research groups set out to investigate the potential of co-doped carbons and, particularly, their applicability for fuel cell catalysts. In most cases, the dopant pair consists of N plus one of B, S, P, which may be a result of the relatively better understanding regarding N-doping.

N-B- and N-P-carbon have also been studied as metal free catalysts [119]. Electrochemical evaluation of each catalyst suggests that both co-doped varieties are superior to N-graphene for ORR performance. The mass activities of the N-, N-B-, and N-P-graphene catalysts as tested were 0.45, 0.53, 0.80 mA/mg, respectively. The authors attribute the improved performance over N-graphene to additional asymmetric spin density resulting from the extra dopant species (B or P). They also suggest, however that nitrogen plays a critical role in the co-doped graphene performance. Their results show that samples of B- and P-graphene synthesized by the same method as their respective co-doped equivalents but without the N source had lower ORR activity compared with N-graphene. Liang et al synthesized N and S dual doped mesoporous graphene (N-S-graphene) by solid state reaction of GO with melamine and benzyl disulfide [123]. They claim N and S concentrations of 4.5 at. % and 2.0 at. %, respectively, which compare closely to the individually N- and S-doped samples they prepared for their study. ORR results clearly show that the metal-free dual doped graphene performs better than either N- or S-graphene in alkaline solution, with an earlier onset potential and greater current density.

1.5 Thesis Objectives

As stated, there is tremendous promise for FC technology presently and in the future. Especially as world energy demand continues to grow, and the need for renewable and highly resilient energy systems is bolstered, FCs stand poised to play an important role. In order to improve the activity, stability, and costs of PEM fuel cell catalysts, it is clear that a materials-based solution can be highly effective, as has been shown. The ORR cathode catalyst remains the most pressing challenge for meeting near-future goals. Understanding the requirements for these catalyst and the ways in which to test them is critical for development. Controlling and exploiting the properties of materials at the nanoscale is a skill that researchers and engineers continue to hone. In this spirit, and with an understanding of the requirements for active and durable FC catalysts, we look to carbon nanostructures. These novel materials, and modifications thereof, have already proven to be highly valuable in a number of electrochemical device applications and particularly in PEMFCs. In my thesis work I have aimed to study the modification of carbon nanostructured materials and to evaluate their ORR activity and durability under simulated FC conditions. Specifically, the thesis aims to address two main issues:

I: To create novel catalyst support materials through synthesis and modification of nanoscale carbons

This is achieved through two studies. The first included synthesizing phosphorus and nitrogen co-doped nanotubes and examines how synthesis parameters effect nanotube growth and morphology as well as doping characteristics. By characterizing the PNCNTs, several conclusions can be drawn about their chemical and physical nature and these are correlated to CV measurements of their ORR activity. Comparison of the co-doped PNCNTs to NCNTs is also done to identify specific advantages of the additional phosphorus dopants.

Secondly, a study of surface treated carbon black supports was done. Using inexpensive, commercially available support materials, I hoped to examine the benefits of

using a simple, one-step treatment process via ozone or ammonia for use improving support characteristics and catalyst activity. Determining the effects of pre-treatment by either method can provide useful insight on improved particle-support interactions and in-turn any subsequent improvement in ORR activity and durability. This is done physically by gas sorption and XPS, followed by XRD and XANES analysis to examine the Pt, and finally electrochemical testing to compare catalyst activity.

II: To measure and understand the catalytic activity and durability of FC catalysts using RDE voltammetry

In addition to RDE studies as a part of the modified carbon studies, which are critical to evaluating their ORR activity and understand their electrochemical characteristics, this aim of this work was to provide insight on RDE testing and its effectiveness for understanding real FC performance. The fifth chapter provides insights into two popular degradation protocols for studying carbon corrosion in the FCs catalyst. The goal was to highlight the need for well-designed protocols for accelerated stress testing by demonstrating clear inconsistencies between RDE and MEA data, using well known carbons. This work is important for the relevance of academic research efforts on FC catalysts which heavily rely on RDE as a screening and evaluation method. It is necessary for the success of novel catalysts that their performance translate from the half-cell to full scale MEA testing.

1.6 Thesis organization

This thesis contains six chapters (two introductory, three articles, and one conclusive chapter), which are organized in an "integrated article" format per the *Thesis Regulation Guide* from the School of Graduate and Postdoctoral Studies at Western University. The outline of each chapter is as follows:

Chapter 1 is an introduction to PEMFCs including their working principle and main technological challenges. This is followed by a review of the catalyst materials used in modern FCs, especially functionalized and doped carbons. The use of these materials as

both Pt support and metal-free catalyst is discussed. Finally, the research objectives and thesis structure are outlined.

Chapter 2 describes in greater detail the experimental methods used for synthesis and surface modification of nanomaterials, methods of physical characterization, and parameters for electrochemical testing of nanomaterials especially for ORR activity.

Chapter 3 is a report on the synthesis of phosphorus and nitrogen co-doped nanotubes (PNCNT) and their potential as metal-free catalysts. Specifically, PNCNTs are grown via CVD and characterized by several methods to determine their physical and chemical structure. Synthesis parameters are varied and their effects documented. Furthermore, the ORR activity of PNCNTs are compared to NCNTs to demonstrate the benefits of co-doping with phosphorus and nitrogen.

Chapter 4 is a study of modified CB used as a Pt catalyst support for PEMFCs. Through a one-step method of either ozone or ammonia treatment, the catalytic activity and durability of Pt/CB catalyst can be improved. The chemical and structural differences in the modified and unmodified CB are investigated, as well as the support Pt characteristics. These changes are discussed in the context of improved activity towards ORR and durability after CV cycling.

Chapter 5 is a report focused on the testing of carbon support corrosion via RDE. The effects of testing temperature, scan rate, and scan speed are evaluated and results compared to MEA data for three well known carbons. In particular, the article aims to highlight the need for robust testing protocols for accelerated stress tests which are meant to represent real fuel cell durability data. This chapter is, in a sense, a red flag for this research community to ensure meaningful results – ones that are likely to translate to real FC systems – can be drawn using when using RDE.

Chapter 6 summarizes the work presented in the thesis and draws overarching conclusions, tying the articles together. A brief prospective is given on future avenues of research in this field.

1.7 References

[1] Bard and Faulkner, *Electrochemical Methods: Fundamentals & Applications*, 2nd ed. John Wiley & Sons, 2001.

[2] J. Zhang, Ed., *PEM Fuel Cell Electrocatalysts and Catalyst Layers*. London: Springer London, 2008.

[3] Department of Energy, *Fuel Cell Handbook*, no. November. 2002.

[4] R. P. O'Hayre, S.-W. Cha, W. Colella, and F. B. Prinz, *Fuel cell fundamentals*. John Wiley & Sons New York, 2006.

[5] D. L. Greene and G. Duleep, "Status and Prospects of the Global Automotive Fuel Cell Industry and Plans for Deployment of Fuel Cell Vehicles and Hydrogen Refueling Infrastructure," 2013.

[6] P. Davis, "DOE Hydrogen and Fuel Cells Program Record 14006: Cradle to Grave Lifecycle Analysis of Vehicle and Fuel Pathways," 2014.

[7] D. Papageorgopoulos, "Fuel Cells Program," in *2015 Annual Merit Review Proceedings*, 2015.

[8] US Department of Energy, "USDRIVE Fuel Cell Technical Team Roadmap, June 2013," 2013.

[9] P. Pei and H. Chen, "Main factors affecting the lifetime of Proton Exchange Membrane fuel cells in vehicle applications: A review," *Appl. Energy*, vol. 125, pp. 60–75, 2014.

[10] Y. Yu, H. Li, H. Wang, X.-Z. Yuan, G. Wang, and M. Pan, "A review on performance degradation of proton exchange membrane fuel cells during startup and shutdown processes: Causes, consequences, and mitigation strategies," *J. Power Sources*, vol. 205, pp. 10–23, May 2012.

[11] W. Schmittinger and A. Vahidi, "A review of the main parameters influencing long-term performance and durability of PEM fuel cells," *J. Power Sources*, vol. 180, pp. 1–14, 2008.

[12] R. Borup, J. Meyers, B. Pivovar, Y. S. Kim, R. Mukundan, N. Garland, D. Myers, M. Wilson, F. Garzon, D. Wood, P. Zelenay, K. More, K. Stroh, T. Zawodzinski, X. J. Boncella, J. E. Mcgrath, O. M. Inaba, K. Miyatake, M. Hori, K. Ota, Z. Ogumi, S. Miyata, A. Nishikata, Z. Siroma, Y. Uchimoto, K. Yasuda, K. Kimijima, and N. Iwashita, "Scientific Aspects of Polymer Electrolyte Fuel Cell Durability and Degradation," pp. 3904–3951, 2007.

[13] L. M. Roen, C. H. Paik, and T. D. Jarvi, “Electrocatalytic Corrosion of Carbon Support in PEMFC Cathodes,” *Electrochem. Solid-State Lett.*, vol. 7, no. 1, p. A19, 2004.

[14] Y. Shao, G. Yin, and Y. Gao, “Understanding and approaches for the durability issues of Pt-based catalysts for PEM fuel cell,” *J. Power Sources*, vol. 171, no. 2, pp. 558–566, 2007.

[15] J. Spendelow and J. Marcinkoski, “DOE Fuel Cell Technologies Office Record 14012: Fuel Cell System Costs,” 2014.

[16] M. K. Debe, “Electrocatalyst approaches and challenges for automotive fuel cells.,” *Nature*, vol. 486, no. 7401, pp. 43–51, Jun. 2012.

[17] G. McLean and T. Niet, “An assessment of alkaline fuel cell technology,” *Int. J. ...*, vol. 27, pp. 507–526, 2002.

[18] G. Merle, M. Wessling, and K. Nijmeijer, “Anion exchange membranes for alkaline fuel cells: A review,” *J. Memb. Sci.*, vol. 377, no. 1–2, pp. 1–35, 2011.

[19] M. M. Doeff, *Encyclopedia of Sustainability Science and Technology*. New York, NY: Springer New York, 2012.

[20] H. W. H. Li and X.-Z. YUan, *PEM Fuel Cell Failure Mode Analysis*. CRC Press, 2011.

[21] U. A. Paulus, T. J. Schmidt, H. A. Gasteiger, and R. J. Behm, “Oxygen reduction on a high-surface area Pt/Vulcan carbon catalyst: a thin-film rotating ring-disk electrode study,” *J. Electroanal. Chem.*, vol. 495, no. 2, pp. 134–145, Jan. 2001.

[22] G. Jerkiewicz, “Electrochemical Hydrogen Adsorption and Absorption. Part 1: Under-potential Deposition of Hydrogen,” *Electrocatalysis*, vol. 1, no. 4, pp. 179–199, 2010.

[23] S. Trasatti and O. A. Petrii, “Real surface area measurements in electrochemistry,” *Pure Appl. Chem.*, vol. 63, no. 5, Jan. 1991.

[24] Y. Garsany, O. a Baturina, K. E. Swider-Lyons, and S. S. Kocha, “Experimental methods for quantifying the activity of platinum electrocatalysts for the oxygen reduction reaction.,” *Anal. Chem.*, vol. 82, no. 15, pp. 6321–8, Aug. 2010.

[25] Y. Garsany, J. Ge, J. St-Pierre, R. Rocheleau, and K. E. Swider-Lyons, “Analytical Procedure for Accurate Comparison of Rotating Disk Electrode Results for the Oxygen Reduction Activity of Pt/C,” *J. Electrochem. Soc.*, vol. 161, no. 5, pp. F628–F640, Mar. 2014.

[26] S. Treimer, A. Tang, and D. C. Johnson, “A consideration of the application of Kouteck??-Levich plots in the diagnoses of charge-transfer mechanisms at rotated disk electrodes,” *Electroanalysis*, vol. 14, no. 3, pp. 165–171, 2002.

[27] K.-L. Hsueh, E. R. Gonzalez, and S. Srinivasan, “Electrolyte effects on oxygen reduction kinetics at platinum: A rotating ring-disc electrode analysis,” *Electrochimica Acta*, vol. 28, no. 5. pp. 691–697, 1983.

[28] K. E. Gubbins and R. D. Walker, “The Solubility and Diffusivity of Oxygen in Electrolytic Solutions,” *J. Electrochem. Soc.*, vol. 112, no. 5, p. 469, 1965.

[29] S. S. Kocha, J. W. Zack, S. M. Alia, K. C. Neyerlin, and B. S. Pivovar, “Influence of Ink Composition on the Electrochemical Properties of Pt/C Electrocatalysts,” *ECS Trans.*, vol. 50, no. 2, pp. 1475–1485, Mar. 2013.

[30] Y. Garsany, J. Ge, J. St-Pierre, R. Rocheleau, and K. Swider-Lyons, “Standardizing Thin-Film Rotating Disk Electrode Measurements of the Oxygen Reduction Activity of Pt/C,” *ECS Trans.*, vol. 58, no. 1, pp. 3–14, Oct. 2013.

[31] Y. Garsany, J. Ge, J. St-Pierre, R. Rocheleau, and K. Swider-Lyons, “ORR Measurements Reproducibility Using a RRDE,” *ECS Trans.*, vol. 58, no. 1, pp. 1233–1241, 2013.

[32] S. S. Kocha, Y. Garsany, and D. Myers, “Testing Oxygen Reduction Reaction Activity with the Rotating Disc Electrode Technique,” *DOE Webinar*, 2013.

[33] S. Kocha, “Best Practices and Benchmark Activities for ORR Measurements by the Rotating Disk Electrode Technique,” *Natl. Renew. Energy Labs*, vol. Dept. of E, 2014.

[34] “Carbon Black,” *Chem. Week*, vol. 171, no. 2, p. 34, Jan. 2009.

[35] A. Lavacchi, H. Miller, and F. Vizza, *Nanotechnology in Electrocatalysis for Energy*, vol. 170. New York, NY: Springer New York, 2013.

[36] H. Boehm, “Some aspects of the surface chemistry of carbon blacks and other carbons,” *Carbon N. Y.*, vol. 32, no. 5, pp. 759–769, 1994.

[37] S. C. Ball, S. L. Hudson, D. Thompsett, and B. Theobald, “An investigation into factors affecting the stability of carbons and carbon supported platinum and platinum/cobalt alloy catalysts during 1.2V potentiostatic hold regimes at a range of temperatures,” *J. Power Sources*, vol. 171, no. 1, pp. 18–25, Sep. 2007.

[38] S. Iijima, “Helical microtubules of graphitic carbon,” *Nature*, vol. 354, no. 6348, pp. 56–58, 1991.

[39] P. J. F. Harris, *Carbon Nanotubes and Related Structures*. publisherNameCambridge University Press, 1999.

[40] P. G. Collins, K. Bradley, M. Ishigami, and A. Zettl, “Extreme Oxygen Sensitivity of Electronic Properties of Carbon Nanotubes,” *Sci.* , vol. 287 , no. 5459 , pp. 1801–1804, Mar. 2000.

[41] A. Bachtold, P. Hadley, T. Nakanishi, and C. Dekker, “Logic Circuits with Carbon Nanotube Transistors,” *Sci.* , vol. 294 , no. 5545 , pp. 1317–1320, Nov. 2001.

[42] M. F. L. De Volder, S. H. Tawfick, R. H. Baughman, and a J. Hart, “Carbon nanotubes: present and future commercial applications.,” *Science*, vol. 339, no. 6119, pp. 535–9, Feb. 2013.

[43] H. Dai, “Carbon nanotubes: synthesis, integration, and properties.,” *Acc. Chem. Res.*, vol. 35, no. 12, pp. 1035–44, Dec. 2002.

[44] E. T. Thostenson, Z. Ren, and T.-W. Chou, “Advances in the science and technology of carbon nanotubes and their composites: a review,” *Compos. Sci. Technol.*, vol. 61, no. 13, pp. 1899–1912, 2001.

[45] P. Nikolaev, M. J. Bronikowski, R. K. Bradley, F. Rohmund, D. T. Colbert, K. a Smith, and R. E. Smalley, “Gas-phase catalytic growth of single-walled carbon nanotubes from carbon monoxide,” *Chem. Phys. Lett.*, vol. 313, no. 1–2, pp. 91–97, 1999.

[46] Y. Li, W. Kim, Y. Zhang, M. Rolandi, D. Wang, and H. Dai, “Growth of Single-Walled Carbon Nanotubes from Discrete Catalytic Nanoparticles of Various Sizes,” *J. Phys. Chem. B*, vol. 105, no. 46, pp. 11424–11431, Nov. 2001.

[47] Y. Zhang, Y. Li, W. Kim, D. Wang, and H. Dai, “Imaging as-grown single-walled carbon nanotubes originated from isolated catalytic nanoparticles,” *Appl. Phys. A*, vol. 74, no. 3, pp. 325–328, 2002.

[48] S. Y. Tsareva, X. Devaux, E. McRae, L. Aranda, B. Gregoire, C. Carteret, M. Dossot, E. Lamouroux, Y. Fort, B. Humbert, and J.-Y. Mevellec, “A step towards controlled-diameter single walled carbon nanotubes,” *Carbon N. Y.*, pp. 1–13, Nov. 2013.

[49] M. Okai, T. Muneyoshi, T. Yaguchi, and S. Sasaki, “Structure of carbon nanotubes grown by microwave-plasma-enhanced chemical vapor deposition,” *Appl. Phys. Lett.*, vol. 77, no. 21, p. 3468, 2000.

[50] Y. C. Choi, D. J. Bae, Y. H. Lee, B. S. Lee, I. T. Han, W. B. Choi, N. S. Lee, and J. M. Kim, “Low temperature synthesis of carbon nanotubes by microwave plasma-enhanced chemical vapor deposition,” *Synth. Met.*, vol. 108, no. 2, pp. 159–163, 2000.

[51] H. Cui, O. Zhou, and B. R. Stoner, “Deposition of aligned bamboo-like carbon nanotubes via microwave plasma enhanced chemical vapor deposition,” *J. Appl. Phys.*, vol. 88, no. 10, p. 6072, 2000.

[52] K. S. Novoselov, A. K. Geim, S. V Morozov, D. Jiang, Y. Zhang, S. V Dubonos, I. V Grigorieva, and A. A. Firsov, "Electric field effect in atomically thin carbon films.," *Science*, vol. 306, no. 5696, pp. 666–9, Oct. 2004.

[53] S. Stankovich, D. a Dikin, G. H. B. Dommett, K. M. Kohlhaas, E. J. Zimney, E. a Stach, R. D. Piner, S. T. Nguyen, and R. S. Ruoff, "Graphene-based composite materials.," *Nature*, vol. 442, no. 7100, pp. 282–6, Jul. 2006.

[54] E. Antolini, "Graphene as a new carbon support for low-temperature fuel cell catalysts," *Appl. Catal. B Environ.*, vol. 123–124, pp. 52–68, Jul. 2012.

[55] S. Chen, P. Bao, L. Xiao, and G. Wang, "Large-scale and low cost synthesis of graphene as high capacity anode materials for lithium-ion batteries," *Carbon N. Y.*, vol. 64, pp. 158–169, Jul. 2013.

[56] K. S. Novoselov, V. I. Fal'ko, L. Colombo, P. R. Gellert, M. G. Schwab, and K. Kim, "A roadmap for graphene.," *Nature*, vol. 490, no. 7419, pp. 192–200, Oct. 2012.

[57] C. N. R. Rao, a K. Sood, K. S. Subrahmanyam, and a Govindaraj, "Graphene: the new two-dimensional nanomaterial.," *Angew. Chem. Int. Ed. Engl.*, vol. 48, no. 42, pp. 7752–77, Jan. 2009.

[58] W. Ren and H.-M. Cheng, "The global growth of graphene.," *Nat. Nanotechnol.*, vol. 9, no. 10, pp. 726–730, Oct. 2014.

[59] Y. P. Chen and Q. Yu, "Nanomaterials: Graphene rolls off the press.," *Nat. Nanotechnol.*, vol. 5, no. 8, pp. 559–60, Aug. 2010.

[60] T. Kobayashi, M. Bando, N. Kimura, K. Shimizu, K. Kadono, N. Umezu, K. Miyahara, S. Hayazaki, S. Nagai, Y. Mizuguchi, Y. Murakami, and D. Hobara, "Production of a 100-m-long high-quality graphene transparent conductive film by roll-to-roll chemical vapor deposition and transfer process," *Appl. Phys. Lett.*, vol. 102, no. 2, p. 023112, 2013.

[61] Y. Hernandez, V. Nicolosi, M. Lotya, F. M. Blighe, Z. Sun, S. De, I. T. McGovern, B. Holland, M. Byrne, Y. K. Gun'Ko, J. J. Boland, P. Niraj, G. Duesberg, S. Krishnamurthy, R. Goodhue, J. Hutchison, V. Scardaci, A. C. Ferrari, and J. N. Coleman, "High-yield production of graphene by liquid-phase exfoliation of graphite.," *Nat. Nanotechnol.*, vol. 3, no. 9, pp. 563–8, Sep. 2008.

[62] A. Zurutuza and C. Marinelli, "Challenges and opportunities in graphene commercialization.," *Nat. Nanotechnol.*, vol. 9, no. 10, pp. 730–734, Oct. 2014.

[63] A. Guha, W. Lu, T. a. Zawodzinski, and D. a. Schiraldi, "Surface-modified carbons as platinum catalyst support for PEM fuel cells," *Carbon N. Y.*, vol. 45, no. 7, pp. 1506–1517, 2007.

[64] V. V. Strelko, N. T. Kartel, I. N. Dukhno, V. S. Kuts, R. B. Clarkson, and B. M. Odintsov, "Mechanism of reductive oxygen adsorption on active carbons with various surface chemistry," *Surf. Sci.*, vol. 548, no. 1–3, pp. 281–290, 2004.

[65] I. Sutherland, E. Sheng, R. H. Bradley, and P. K. Freakley, "Effects of ozone oxidation on carbon black surfaces," *J. Mater. Sci.*, vol. 31, no. 21, pp. 5651–5655, 1996.

[66] A. Lushington, J. Liu, Y. Tang, R. Li, and X. Sun, "Surface modification of nitrogen-doped carbon nanotubes by ozone via atomic layer deposition," *J. Vac. Sci. Technol. A Vacuum, Surfaces, Film.*, vol. 32, no. 1, p. 01A124, 2014.

[67] Z.-B. Wang, G.-P. Yin, and P.-F. Shi, "Effects of ozone treatment of carbon support on Pt–Ru/C catalysts performance for direct methanol fuel cell," *Carbon N. Y.*, vol. 44, no. 1, pp. 133–140, 2006.

[68] X. Chen, M. Farber, Y. Gao, I. Kulaots, E. M. Suuberg, and R. H. Hurt, "Mechanisms of surfactant adsorption on non-polar, air-oxidized and ozone-treated carbon surfaces," *Carbon N. Y.*, vol. 41, no. 8, pp. 1489–1500, 2003.

[69] C. Prado-Burguete, a. Linares-Solano, F. Rodriguez-Reinoso, and C. Salinas-Martinez de Leca, "The Effect of Oxygen Surface Groups of the Support Dispersion in Pt / Carbon Catalysts on Platinum," *J. Catal.*, vol. 115, pp. 98–106, 1989.

[70] a. Guerrero-Ruiz, P. Badenes, and I. Rodríguez-Ramos, "Study of some factors affecting the Ru and Pt dispersions over high surface area graphite-supported catalysts," *Appl. Catal. A Gen.*, vol. 173, no. 2, pp. 313–321, 1998.

[71] P. Ehrburger, O. P. Mahajan, and P. L. Walker, "32. Carbon as a support for catalysis—effect of surface heterogeneity of carbon on dispersion of platinum," *Carbon*, vol. 14, no. 5. p. 295, 1976.

[72] H. Wang, R. Côté, G. Faubert, D. Guay, and J. P. Dodelet, "Effect of the Pre-Treatment of Carbon Black Supports on the Activity of Fe-Based Electrocatalysts for the Reduction of Oxygen," *J. Phys. Chem. B*, vol. 103, no. 12, pp. 2042–2049, 1999.

[73] K. N. Wood, R. O'Hayre, and S. Pylypenko, "Recent progress on nitrogen/carbon structures designed for use in energy and sustainability applications," *Energy Environ. Sci.*, vol. 7, no. 4, p. 1212, 2014.

[74] H. Wang, T. Maiyalagan, and X. Wang, "Review on Recent Progress in Nitrogen-Doped Graphene: Synthesis, Characterization, and Its Potential Applications," *ACS Catal.*, vol. 2, no. 5, pp. 781–794, May 2012.

[75] J. Zhang, Z. Wang, and Z. Zhu, "A density functional theory study on oxygen reduction reaction on nitrogen-doped graphene.," *J. Mol. Model.*, Nov. 2013.

[76] N. P. Subramanian, X. Li, V. Nallathambi, S. P. Kumaraguru, H. Colon-Mercado, G. Wu, J. W. Lee, and B. N. Popov, "Nitrogen-modified carbon-based catalysts for oxygen reduction reaction in polymer electrolyte membrane fuel cells," *J. Power Sources*, vol. 188, no. 1, pp. 38–44, 2009.

[77] Y. Shao, J. Sui, G. Yin, and Y. Gao, "Nitrogen-doped carbon nanostructures and their composites as catalytic materials for proton exchange membrane fuel cell," *Appl. Catal. B Environ.*, vol. 79, no. 1, pp. 89–99, Feb. 2008.

[78] G. Wu, D. Li, C. Dai, D. Wang, and N. Li, "Well-dispersed high-loading Pt nanoparticles supported by shell-core nanostructured carbon for methanol electrooxidation," *Langmuir*, vol. 24, no. 7, pp. 3566–3575, 2008.

[79] L. F. Mabena, S. Sinha Ray, S. D. Mhlanga, and N. J. Coville, "Nitrogen-doped carbon nanotubes as a metal catalyst support," *Appl. Nanosci.*, vol. 1, no. 2, pp. 67–77, May 2011.

[80] Y. Chen, J. Wang, H. Liu, M. N. Banis, R. Li, X. Sun, T. Sham, S. Ye, and S. Knights, "Nitrogen Doping Effects on Carbon Nanotubes and the Origin of the Enhanced Electrocatalytic Activity of Supported Pt for Proton-Exchange Membrane Fuel Cells," *J. Phys. Chem. C*, vol. 115, no. 9, pp. 3769–3776, Mar. 2011.

[81] R. Imran Jafri, N. Rajalakshmi, and S. Ramaprabhu, "Nitrogen doped graphene nanoplatelets as catalyst support for oxygen reduction reaction in proton exchange membrane fuel cell," *J. Mater. Chem.*, vol. 20, no. 34, p. 7114, 2010.

[82] M. N. Groves, a. S. W. Chan, C. Malardier-Jugroot, and M. Jugroot, "Improving platinum catalyst binding energy to graphene through nitrogen doping," *Chem. Phys. Lett.*, vol. 481, no. 4–6, pp. 214–219, Oct. 2009.

[83] Y. Zhou, K. Neyerlin, T. S. Olson, S. Pylypenko, J. Bult, H. N. Dinh, T. Gennett, Z. Shao, and R. O'Hayre, "Enhancement of Pt and Pt-alloy fuel cell catalyst activity and durability via nitrogen-modified carbon supports," *Energy Environ. Sci.*, vol. 3, no. 10, p. 1437, 2010.

[84] L. Zhang, J. Niu, L. Dai, and Z. Xia, "Effect of microstructure of nitrogen-doped graphene on oxygen reduction activity in fuel cells.," *Langmuir*, vol. 28, no. 19, pp. 7542–50, May 2012.

[85] E. Gracia-Espino, X. Jia, and T. Wågberg, "Improved Oxygen Reduction Performance of Pt–Ni Nanoparticles by Adhesion on Nitrogen-Doped Graphene," *J. Phys. Chem. C*, p. 140128161103004, Jan. 2014.

[86] O. Stephan, P. M. Ajayan, C. Colliex, P. Redlich, J. M. Lambert, P. Bernier, and P. Lefin, "Doping Graphitic and Carbon Nanotube Structures with Boron and Nitrogen," *Sci.* , vol. 266 , no. 5191 , pp. 1683–1685, Dec. 1994.

[87] R. Sen, B. C. Satishkumar, A. Govindaraj, K. R. Harikumar, M. K. Renganathan, and C. N. R. Rao, "Nitrogen-containing carbon nanotubes," vol. 1, no. c, pp. 2335–2337, 1997.

[88] K. Gong, F. Du, Z. Xia, M. Durstock, and L. Dai, "Nitrogen-doped carbon nanotube arrays with high electrocatalytic activity for oxygen reduction.," *Science*, vol. 323, no. 5915, pp. 760–4, Feb. 2009.

[89] M. S. Saha, R. Li, X. Sun, and S. Ye, "3-D composite electrodes for high performance PEM fuel cells composed of Pt supported on nitrogen-doped carbon nanotubes grown on carbon paper," *Electrochem. commun.*, vol. 11, no. 2, pp. 438–441, 2009.

[90] J. Liu, H. Liu, Y. Zhang, R. Li, G. Liang, M. Gauthier, and X. Sun, "Synthesis and characterization of phosphorus–nitrogen doped multiwalled carbon nanotubes," *Carbon N. Y.*, vol. 49, no. 15, pp. 5014–5021, Dec. 2011.

[91] X. Wang, X. Li, L. Zhang, Y. Yoon, P. K. Weber, H. Wang, J. Guo, and H. Dai, "N-doping of graphene through electrothermal reactions with ammonia.," *Science*, vol. 324, no. 5928, pp. 768–71, May 2009.

[92] J. Choi, D. Lee, and Z. Chen, "Nitrogen-doped Activated Graphene Supported Platinum Electrocatalyst for Oxygen Reduction Reaction in PEM Fuel Cells," *Ecs Trans.*, vol. 50, no. 2, pp. 1815–1822, 2013.

[93] N. Cheng, J. Liu, M. N. Banis, D. Geng, R. Li, S. Ye, S. Knights, and X. Sun, "High stability and activity of Pt electrocatalyst on atomic layer deposited metal oxide/nitrogen-doped graphene hybrid support," *Int. J. Hydrogen Energy*, pp. 2–9, Feb. 2014.

[94] D. Geng, Y. Hu, Y. Li, R. Li, and X. Sun, "One-pot solvothermal synthesis of doped graphene with the designed nitrogen type used as a Pt support for fuel cells," *Electrochem. commun.*, vol. 22, pp. 65–68, Aug. 2012.

[95] H. Zhao, K. S. Hui, and K. N. Hui, "Synthesis of nitrogen-doped multi-layer graphene from milk powder with melamine and their application to fuel cells," *Carbon N. Y.*, Apr. 2014.

[96] H. Ghanbarlou, S. Rowshanzamir, B. Kazeminasab, and M. J. Parnian, "Non-precious metal nanoparticles supported on nitrogen-doped graphene as a promising catalyst for oxygen reduction reaction: Synthesis, characterization and electrocatalytic performance," *J. Power Sources*, Oct. 2014.

[97] S. Bag, K. Roy, C. S. Gopinath, and C. R. Raj, "A Facile Single-Step Synthesis of Nitrogen-Doped Reduced Graphene Oxide-Mn3O4 Hybrid Functional Material for the Electrocatalytic Reduction of Oxygen," *ACS Appl. Mater. Interfaces*, p. 140129071105005, Jan. 2014.

[98] E. Cruz-Silva, D. A. Cullen, L. Gu, J. M. Romo-Herrera, E. Muñoz-Sandoval, F. López-Urías, B. G. Sumpter, V. Meunier, J. Charlier, D. J. Smith, H. Terrones, and M. Terrones, "Heterodoped nanotubes: theory, synthesis, and characterization of phosphorus-nitrogen doped multiwalled carbon nanotubes.," *ACS Nano*, vol. 2, no. 3, pp. 441–8, Mar. 2008.

[99] Y. Zhang, T. Mori, J. Ye, and M. Antonietti, "Phosphorus-doped carbon nitride solid: enhanced electrical conductivity and photocurrent generation.," *J. Am. Chem. Soc.*, vol. 132, no. 18, pp. 6294–5, May 2010.

[100] I. Shimoyama, T. Hakoda, A. Shimada, and Y. Baba, "Influence of configuration at dopant sites on catalytic activity of phosphorus-doped graphite," *Carbon N. Y.*, pp. 1–12, Sep. 2014.

[101] Z.-W. Liu, F. Peng, H.-J. Wang, H. Yu, W.-X. Zheng, and J. Yang, "Phosphorus-Doped Graphite Layers with High Electrocatalytic Activity for the O2 Reduction in an Alkaline Medium," *Angew. Chemie*, vol. 123, no. 14, pp. 3315–3319, Mar. 2011.

[102] C. Zhang, N. Mahmood, H. Yin, F. Liu, and Y. Hou, "Synthesis of phosphorus-doped graphene and its multifunctional applications for oxygen reduction reaction and lithium ion batteries.," *Adv. Mater.*, vol. 25, no. 35, pp. 4932–7, Sep. 2013.

[103] R. Li, Z. Wei, X. Gou, and W. Xu, "Phosphorus-doped graphene nanosheets as efficient metal-free oxygen reduction electrocatalysts," *RSC Adv.*, vol. 3, no. 25, p. 9978, 2013.

[104] X. Ma, G. Ning, C. Qi, C. Xu, and J. Gao, "Phosphorus and nitrogen dual-doped few-layered porous graphene: a high-performance anode material for lithium-ion batteries.," *ACS Appl. Mater. Interfaces*, vol. 6, no. 16, pp. 14415–22, Aug. 2014.

[105] D.-S. Yang, D. Bhattacharjya, S. Inamdar, J. Park, and J.-S. Yu, "Phosphorus-doped ordered mesoporous carbons with different lengths as efficient metal-free electrocatalysts for oxygen reduction reaction in alkaline media.," *J. Am. Chem. Soc.*, vol. 134, no. 39, pp. 16127–30, Oct. 2012.

[106] Z. Liu, F. Peng, H. Wang, H. Yu, J. Tan, and L. Zhu, "Novel phosphorus-doped multiwalled nanotubes with high electrocatalytic activity for O2 reduction in alkaline medium," *Catal. Commun.*, vol. 16, no. 1, pp. 35–38, Nov. 2011.

[107] A. G. Garcia, S. E. Baltazar, A. H. R. Castro, J. F. P. Robles, and A. Rubio, "Influence of S and P Doping in a Graphene Sheet," *J. Comput. Theor. Nanosci.*, vol. 5, no. 11, pp. 2221–2229, Nov. 2008.

[108] D. Geng, S. Yang, Y. Zhang, J. Yang, J. Liu, R. Li, T.-K. Sham, X. Sun, S. Ye, and S. Knights, "Nitrogen doping effects on the structure of graphene," *Appl. Surf. Sci.*, vol. 257, no. 21, pp. 9193–9198, Aug. 2011.

[109] E. Cruz-Silva, F. López-Urías, E. Muñoz-Sandoval, B. G. Sumpter, H. Terrones, J. Charlier, V. Meunier, and M. Terrones, "Electronic transport and mechanical properties of phosphorus- and phosphorus-nitrogen-doped carbon nanotubes.," *ACS Nano*, vol. 3, no. 7, pp. 1913–21, Jul. 2009.

[110] P. Song, L. Zhu, X. Bo, A. Wang, G. Wang, and L. Guo, *Pt nanoparticles incorporated into phosphorus-doped ordered mesoporous carbons: enhanced catalytic activity for methanol electrooxidation*. Elsevier Ltd, 2014.

[111] Z. Liu, J. Qu, X. Fu, Q. Wang, G. Zhong, and F. Peng, "Low Pt content catalyst supported on nitrogen and phosphorus-codoped carbon nanotubes for electrocatalytic O2 reaction in acidic medium," *Mater. Lett.*, vol. 142, pp. 115–118, Mar. 2015.

[112] Z. Liu, Q. Shi, R. Zhang, Q. Wang, G. Kang, and F. Peng, "Phosphorus-doped carbon nanotubes supported low Pt loading catalyst for the oxygen reduction reaction in acidic fuel cells," *J. Power Sources*, vol. 268, pp. 171–175, Dec. 2014.

[113] J. Zhu, G. He, L. Liang, Q. Wan, and P. K. Shen, "Direct anchoring of platinum nanoparticles on nitrogen and phosphorus-dual-doped carbon nanotube arrays for oxygen," *Elsevier Ltd*, 2015.

[114] Z. Yang, Z. Yao, G. Li, G. Fang, H. Nie, Z. Liu, X. Zhou, X. Chen, and S. Huang, "Sulfur-doped graphene as an efficient metal-free cathode catalyst for oxygen reduction.," *ACS Nano*, vol. 6, no. 1, pp. 205–11, Jan. 2012.

[115] D. Higgins, M. A. Hoque, M. H. Seo, R. Wang, F. Hassan, J.-Y. Choi, M. Pritzker, A. Yu, J. Zhang, and Z. Chen, "Development and Simulation of Sulfur-doped Graphene Supported Platinum with Exemplary Stability and Activity Towards Oxygen Reduction," *Adv. Funct. Mater.*, p. n/a–n/a, Mar. 2014.

[116] J.-E. Park, Y. J. Jang, Y. J. Kim, M.-S. Song, S. Yoon, D. H. Kim, and S.-J. Kim, "Sulfur-doped graphene as a potential alternative metal-free electrocatalyst and Pt-catalyst supporting material for oxygen reduction reaction.," *Phys. Chem. Chem. Phys.*, Nov. 2013.

[117] L. Zhang, J. Niu, M. Li, and Z. Xia, "Catalytic Mechanisms of Sulfur-Doped Graphene as Efficient Oxygen Reduction Reaction Catalysts for Fuel Cells," *J. Phys. Chem. C*, vol. 118, no. 7, p. 140129142225009, Jan. 2014.

[118] X. Xu, T. Yuan, Y. Zhou, Y. Li, J. Lu, X. Tian, D. Wang, and J. Wang, "Facile synthesis of boron and nitrogen-doped graphene as efficient electrocatalyst for the oxygen reduction reaction in alkaline media," *Int. J. Hydrogen Energy*, pp. 1–10, Jan. 2014.

[119] C. H. Choi, M. W. Chung, H. C. Kwon, S. H. Park, and S. I. Woo, "B, N- and P, N-doped graphene as highly active catalysts for oxygen reduction reactions in acidic media," *J. Mater. Chem. A*, vol. 1, no. 11, p. 3694, 2013.

[120] Z.-H. Sheng, H.-L. Gao, W.-J. Bao, F.-B. Wang, and X.-H. Xia, "Synthesis of boron doped graphene for oxygen reduction reaction in fuel cells," *J. Mater. Chem.*, vol. 22, no. 2, p. 390, 2012.

[121] L. Yang, S. Jiang, Y. Zhao, L. Zhu, S. Chen, X. Wang, Q. Wu, J. Ma, Y. Ma, and Z. Hu, "Boron-doped carbon nanotubes as metal-free electrocatalysts for the oxygen reduction reaction.," *Angew. Chem. Int. Ed. Engl.*, vol. 50, no. 31, pp. 7132–5, Jul. 2011.

[122] C. L. Muhich, J. Y. Westcott, T. C. Morris, A. W. Weimer, and C. B. Musgrave, "The E ff ect of N and B Doping on Graphene and the Adsorption and Migration Behavior of Pt Atoms," 2013.

[123] J. Liang, Y. Jiao, M. Jaroniec, and S. Z. Qiao, "Sulfur and nitrogen dual-doped mesoporous graphene electrocatalyst for oxygen reduction with synergistically enhanced performance.," *Angew. Chem. Int. Ed. Engl.*, vol. 51, no. 46, pp. 11496–500, Nov. 2012.

2 Experimental Methods

The use of nanomaterials is inherently challenging because of their size. Fortunately, several advanced characterization techniques are available to examine the structure, morphology, and chemical and electronic nature of materials. In this chapter, a number of those methods are outlined which are applicable to the studies in this thesis. Since an exhaustive description of characterization methods would be well beyond the scope of this report, emphasis will be placed on studies of carbon nanomaterials and Pt/carbon structures used as electrocatalysts. For each case, a limited description of background fundamentals is given.

2.1 Materials Synthesis and Preparation

2.1.1 Chemical Vapor Deposition

Chemical vapor deposition (CVD) is a method of growing materials using gas-phase precursors. Typically, gases are introduced to a reaction chamber at some elevated temperature and react with a substrate either directly or with the aid of a catalyst. One advantage of CVD is that it has chemically selectivity, as opposed to physical vapor deposition (PVD) methods such as sputtering, which deposit material over the entire substrate regardless of its characteristics. CVD has become one of the most popular ways to grow CNTs. A vapor-phase carbon source such as a gaseous hydrocarbon can be used in conjunction with a metallic catalyst, especially iron or nickel [1]. NCNTs can be grown by a similar method using precursors that also contain nitrogen [2].

In Chapter 3, we used the so-called floating catalyst method to deliver Fe catalyst particles to the substrate. A schematic of the CVD system used is shown in Figure 2-1. The reaction chamber is a quartz tube with 25 mm diameter. The precursor materials and catalyst are held separately but in the same location in the tube. The catalyst is melted and evaporated near the entrance of the furnace where the temperature is roughly 200°C. The precursors are also melted and as they begin to evaporate the vapors are carried by inert

gas to the center of the tube where it deposits on the substrate, which could be carbon paper or alumina. Ar was used as the carrier gas and the flow rate was controlled by a typical rotameter (Matheson Tri-Gas). After the furnace was turned off and the system was allowed to cool to room temperature, material was collected by scraping the soot from the substrate.

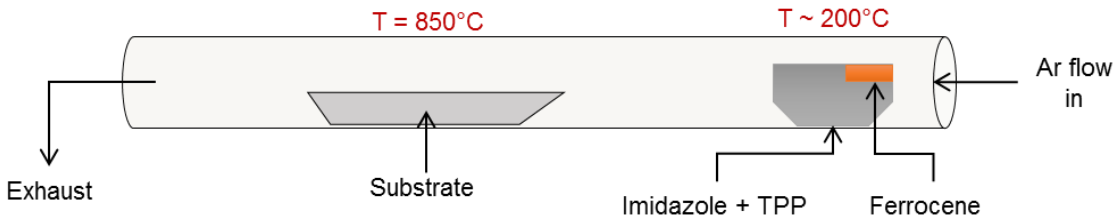

Figure 2-1. Schematic of the experimental setup for floating catalyst CVD of phosphorus and nitrogen co-doped CNTs.

2.1.2 High Temperature Gas Phase Treatment

Powder samples can be heat treated using a quartz tube as reaction chamber and a conventional tube furnace for temperature control. Normally, the furnace is used in a horizontal orientation, however when treating powders with a gas, this is not an optimal setup for mass transport of gas through the sample, nor for holding the powder. Commonly, in chemical engineering, fluid bed reactors are used for mixtures of gas and solid phase materials [3]. Adapting this, in an elementary way, this system was designed to improve mass flow of gases through powder samples and support the sample directly. A fritted porous quartz disk was used as a filter which allowed gases to pass through but not the fine powder. A photograph of this experimental setup and a closer photo of the quartz filter is shown Figure 2-2. In my experiments, gas was flowed from the bottom of the tube towards the powder. The length of the tube above the quartz disk was >40 cm, and the gas kept at low flow-rates, which ensured minimal powder was lost. The temperature of the system was controlled using built-in furnace control. Ar and NH_3 gas flow was controlled using basic rotameters.

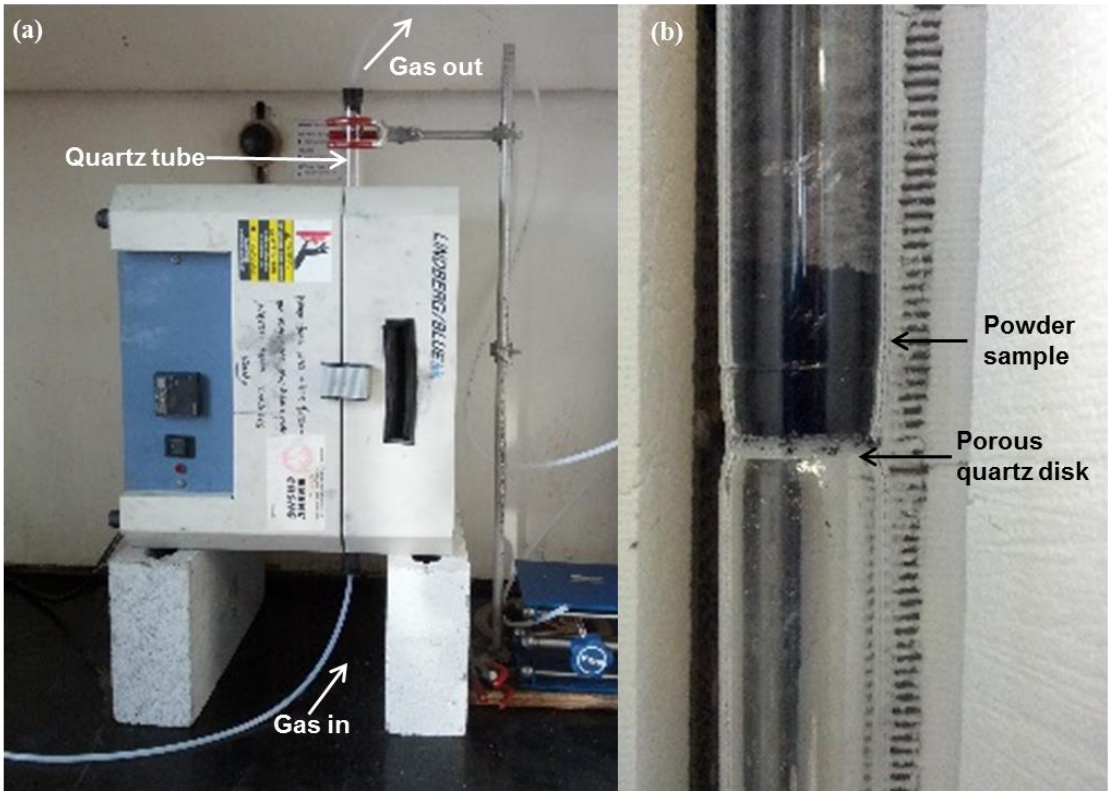

Figure 2-2. Experimental setup for ammonia treatment of carbon nanomaterials. (a) Tube furnace with inlet and outlet gas lines visible at the bottom and top of the quartz tube. (b) Image of a carbon powder sample in the center of reaction tube, supported on a fritted quartz disk.

2.1.3 Atomic Layer Deposition

Atomic layer deposition (ALD) is a process akin to chemical vapour deposition (CVD), which introduces precursor chemicals that react and deposit onto a substrate of choice. In a typical CVD process, reactants are flowed continuously for the duration of the deposition process. In ALD, two or three precursor chemicals are used and are fed to the chamber in sequence, with a purge between. The result is a series of cyclic, self-limiting reactions that allow for very fine control of the deposition [4]. For example, during the deposition of aluminum oxide (Al_2O_3), tri-methyl-aluminum (TMA) is first pulsed into the chamber where it reacts with active OH surface sites on the substrate. After a short reaction time the chamber is purged and evacuated. Removing the excess reactants from the first

half-reaction ensures that only a single atomic layer is deposited [5]. Next, H_2O is introduced as the 2nd precursor and reacts with of the monolayer of TMA which uniformly covers the substrate surface, forming Al_2O_3. The H_2O is then pumped out, concluding the first ALD cycle.

Ozone treatment using ALD was done in a similar manner with repeated cycles consisting of the following three steps: (1) an ozone pulse of 200 ms, (2) a 10s exposure of the sample to the O3, and (3) a 1s pulse of N_2 and 10s delay to purge excess ozone and any gaseous by-products that may have been created [6].

2.1.4 Microwave Assisted Polyol Process for Pt nanoparticle Growth and Deposition

Synthesizing Pt nanoparticles and depositing them on to support materials is an important capability needed to prepare PEMFC catalysts. One of the most common methods for producing metallic nanoparticles is a solution based reduction of the metal salt. In the case of Pt chloroplatinic acid (H_2PtCl_6•$6H_2O$) is often used. Microwave-assisted polyol method has been used previously to grow colloidal Pt nanoparticles from chloroplatinic acid [7], [8]. Though myriad reducing agents are available, previous literature has shown that weaker reducing agents, such as sodium citrate or ethylene glycol (EG), can produce smaller and more evenly dispersed Pt nanoparticles than strong reducing agents such as sodium borohydride [9]. We used EG as both the solvent and reducing agent. Besides being a mild reducing agent, EG also has a higher viscosity than aqueous solutions, which hinders agglomerations of small colloidal nanoparticles [10]. Adjusting the pH of the solution will also affect the reducing rate of the metal particles and it has been shown that adjusting the pH to above 10 is an effective way to control the size, and in some cases the shape, of Pt nanoparticles [7]. The advantage of using microwave heating, as opposed to conventional heating elements or hot plates, has also been recognized. In particular, microwave heating can accelerate reactions significantly over conventional heating and provide localized, short term heating for lower total energy usage [7], [11].

Our procedure is briefly described here. 150 mL of EG was added to 50 mg of support carbon in a glass beaker. For a catalyst of 40 wt. % loading, 88.9 mg of $H_2PtCl_6 \cdot 6H_2O$ was added (the salt has 37.5% Pt content). This solution was then sonicated for 2 hours to ensure an excellent dispersion of both support and salt. During this time, a concentrated solution of NaOH in EG was used to bring the pH of the sample solution to 11. The pH was adjusted at least one hour prior to heating. The beaker was placed in a commercial microwave oven (1100 W, Panasonic) and heated for 2 minutes, until bubbles were just visible. The mixture was then allowed to cool to room temperature. Once cooled, the solution was stirred and reagent grade HCl (37%) added dropwise to bring the pH <2. Stirring continued for 15 minutes before finally filtering and washing with pure H_2O. Finally, the washed product was dried in a vacuum oven at 60°C for 24 hours.

2.2 Physical Characterization

It is imperative for any materials research efforts to be able to accurately characterize the materials made. This may involve imaging the material structure, identifying its elemental composition, or probing its electronic properties. Herein, a number of the experimental techniques used for this thesis work are described.

2.2.1 Scanning Electron Microscopy (SEM)

A scanning electron microscope (SEM) was used for visually examining synthesized materials. The instrument used is a high-resolution Hitachi S-4800 field emission SEM, shown in Figure 2-3(a). It is normally operated under vacuum conditions of ~$1x10^{-7}$ torr, with either 5 kV or 10 kV acceleration and 15 μA current. The SEM was operated in secondary electron (SE) mode using both the upper and backscattered (mixed) electron collectors. By using mixed collectors, added contrast can be see between elements with different atomic numbers. This is particularly useful for imaging Pt on carbon samples where the Pt will appear brighter compared to the carbon support, as can be seen in Figure 2-3(b). Powder samples were deposited on carbon tape and excess blown away with

compressed air. As the samples had good conductivity, no additional sample preparation was needed.

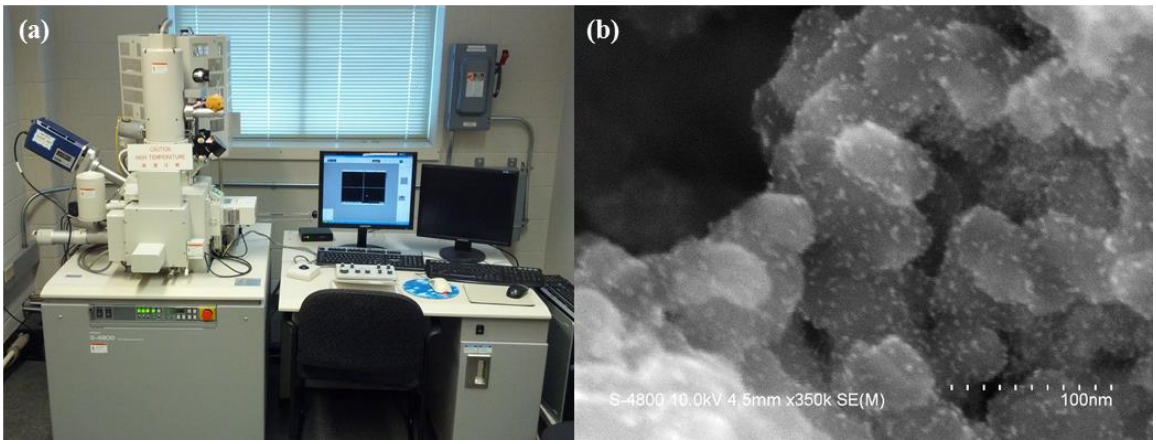

Figure 2-3. (a) Photograph of Hitachi S-4800 SEM instrument at UWO. (b) Typical SEM image of Pt on carbon black catalyst using 10 kV acceleration voltage and mixed detectors in SE mode to enhanced the elemental contrast.

2.2.2 Transmission Electron Microscopy (TEM)

Transmission electron microscopy (TEM) is a useful tool for imaging samples at very high resolutions. TEM has a resolution well under 1 nm, which is notably better than SEM. As the name suggests TEM creates an image by collecting electrons which have passed through a sample. Therefore, only extremely small and conductive samples can be imaged using TEM. The result is sub-nanometer resolution that allows for simple determination of particle size, observation of material architectures, and identification of amorphous and crystalline phases including the ability to directly measure lattice spacing. A TEM instrument requires very high vacuum conditions, a large energy source for accelerating electrons at very high voltages, and a column of advanced electron optics consisting of magnets and lenses [12]. A schematic of the inner parts of a TEM column is shown in Figure 2-4(b).

TEM imaging was performed by a technician on a field-emission TEM (JEOL 2010F) at the Canadian Center for Electron Microscopy (CCEM) at McMaster University.

Operating voltage of 200 kV was used. A photograph of the instrument is shown in Figure 2-4(a). Normally, complicated sample preparation is one of the challenges of doing TEM. However, since all of the samples which were analyzed by TEM for this thesis were powder based, their preparation was straightforward. A small amount (~0.5 mg) of sample was sonicated in high-purity methanol to disperse it well. Subsequently, a single drop of that solution was dropped onto a holey carbon TEM grid and allowed to dry in air. The grid was then checked using our TEM at UWO to ensure its quality before imagining at CCEM.

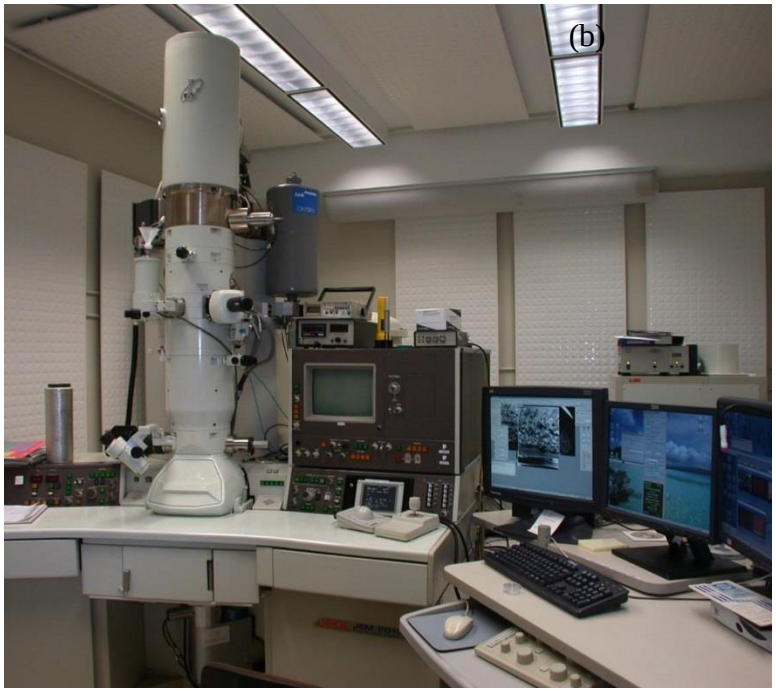

Figure 2-4. (a) Photograph of the JEOL 2010F instrument at the Canadian Center for Electron Microscopy.

2.2.3 Gas-Sorption

Gas sorption is a technique for determining the surface area and pore size of materials. It is often referred to simply as BET, after the scientists who developed the method: Brunauer, Emmett, and Teller [13]. This method works by measuring the adsorption of nitrogen molecules onto a sample surface at set pressures. A sample of known weight is brought to a precise temperature and near-vacuum pressure. Then, gaseous N_2 is

added to the sample cell in known amounts and the pressure change is recorded. N_2 molecules physically adsorb to the surface and cover a known area (~16 $Å^2$). An isotherm of the adsorption and then desorption of N_2, the latter as the pressure is reduced again to vacuum levels, is recorded at set points throughout the test. By measuring the amount of N_2 adsorbed and the pressure change, the total surface area of the sample can be determined. Knowing the weight of the sample to good precision allows for calculation of the specific surface are of the sample in m^2/g. Two important assumptions made when using this method. The first is the only one N_2 molecule can occupy a surface site on the sample. Unfortunately this is not entirely true as multilayer adsorption can take place. The second assumption is that there is no interaction between adjacent molecules of N_2. Again, the assumption is not perfectly correct. Despite the discrepancies between the assumed model and real physical phenomenon, gas sorption remains a highly reproducible method and an excellent tool for determining material surface area and pore size.

Conducting a gas-sorption analysis involves several steps. The sample weight must be accurately known. To do this, the empty cell is first measured, then measured again after the material is added. Following this, degassing is done to remove any residual contaminants, especially water, from the sample so that it is dry and clean before analysis. Degassing is done at elevated temperature under vacuum or an inert gas blanket. Finally, the sample and cell are weighed again after degassing to get the true sample weight. The instruments used for measurement was a Micrometrics TriStar II Series porosity analyzer for chapter 4, and a Quantachrome Nova 2000e surface area & pore size analyzer in chapter 5. Specifics on the degassing conditions is given in each chapter.

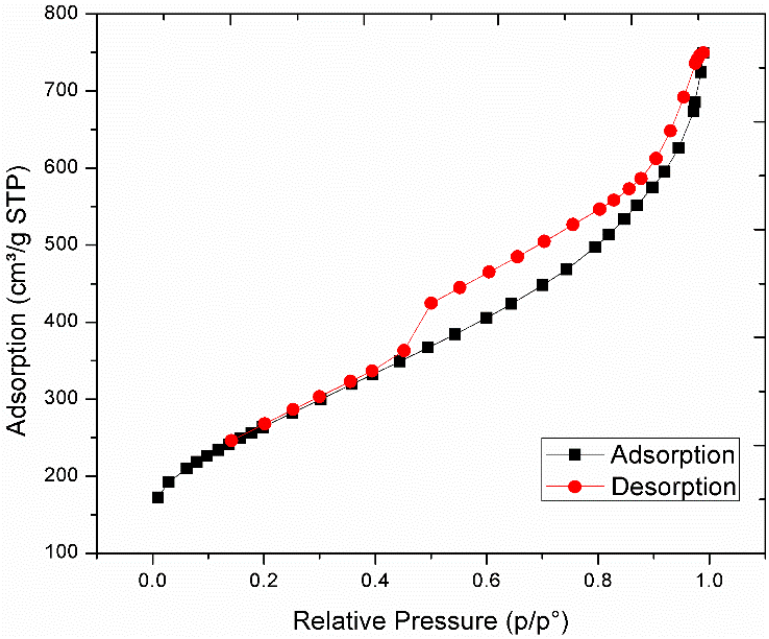

Figure 2-5. Typical N_2 gas sorption isotherm of a high surface area material with adsorption points in black and desorption in red. The hysteresis during desorption is a result of micropores.

2.2.4 Raman Spectroscopy

Raman is a spectroscopic technique that measures light scattering due to molecular vibrations in a sample. The vibrations occur as a result of excitation from incident light, typically in the visible or infrared range. The incident photons from the laser cause molecular vibrations between molecules in the sample. As those high energy vibrations relax, they emit a photon of lesser energy than the incident photon ($E_{emit} < E_{inc}$), this is called Stokes scattering [12]. Alternatively, the scattered light may be of higher energy than the incident ($E_{emit} > E_{inc}$), which is called anti-Stokes scattering. In reality, a third mechanism, Raleigh scattering, where the emitted photons are of equal energy to the incident ($E_{emit} = E_{inc}$), is the most prevalent and thus the most intense. However, Raman only measures Stokes or anti-Stokes scattering. This is important because it means that only polarizable molecules can be imaged by Raman [12].

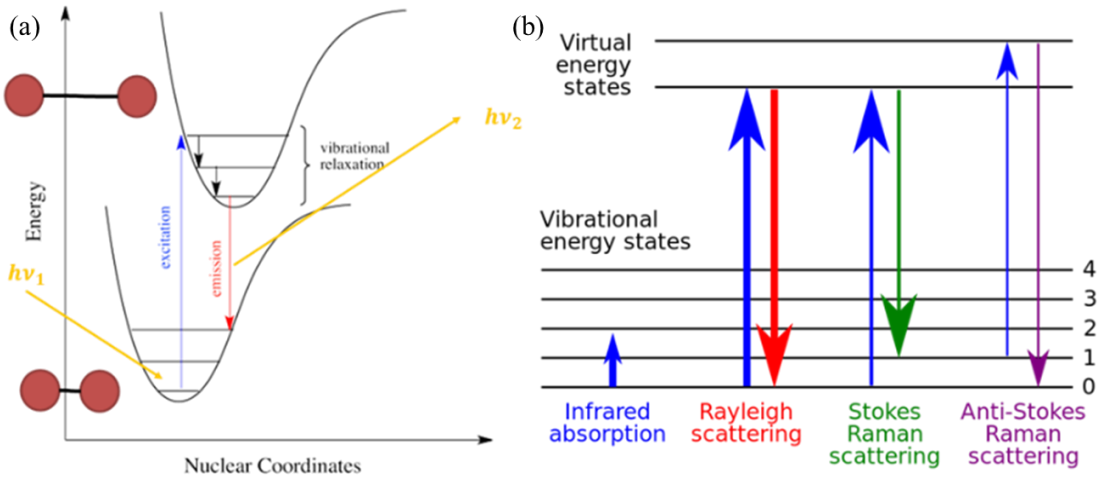

Figure 2-6. (a) Molecular vibrational energy states of a molecule in high and low energy states, showing incident and emitted photons. (b) Photon absorption and emission energies for different scattering mechanisms.

Similar to other spectroscopic techniques, a Raman scan produces a spectrum of intensity vs wavenumber, which is the inverse of the wavelength (cm^{-1}). The plotted spectrum, then, has characteristic peaks for different kinds of molecular species in a sample that can be identified as fingerprints. Some Raman spectra of different carbon samples is shown in Figure 2-7. Of specific importance for studying carbon materials are the G-band and D-band, which appear around 1585 and 1350 cm^{-1}, respectively. The G-band corresponds to sp^2, or highly graphitic carbon such as that which might be found in CNTs or graphene. The D-band, meanwhile, corresponds to defects or disorder in the sp^2 lattice, or to sp^3 carbon. An important metric is the I_D/I_G value which is the ratio of the areas under each peak. This value quantifies the relative amount of defects compared to ordered carbon and can be used to compare materials.

The instrument in our lab is a HORIBA Scientific LabRAM spectrometer. Samples are placed on clean glass slide under the optical microscope for measurement. Calibration is done with a piece of pure Si which has a well-known peak. A 532 nm laser is used for excitation. The power of the laser, the exposure time, and the number of accumulations (i.e. number of scattering spectra recorded) can all affect the results and tuning these is necessary to reduce noise and get reliable signals. With carbon samples, a low laser power

is generally good meaning more accumulations must be used to get a good signal to noise ratio.

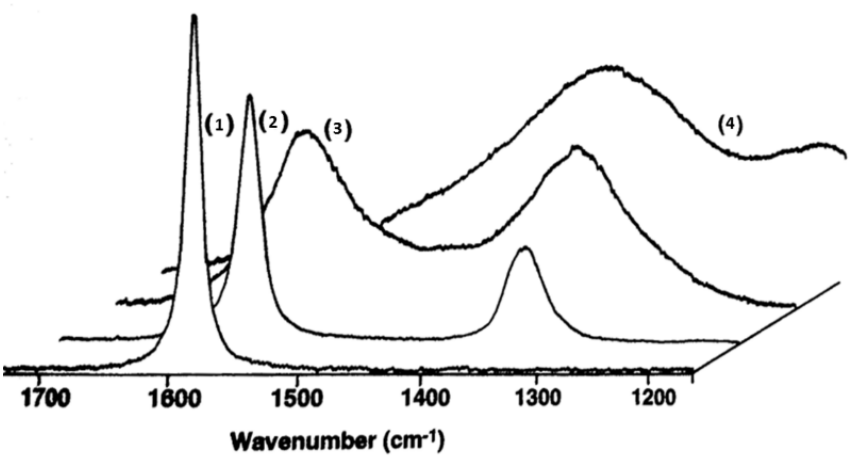

Figure 2-7. (a) Raman spectra for (1) highly ordered graphite, (2) polycrystalline graphite, (3) amorphous carbon, (4) diamond-like carbon [14]. The D- and G-bands at 1350 and 1590 cm^{-1}, respectively, are noticeable especially in (2) and (3).

2.2.5 X-Ray Diffraction (XRD)

X-ray diffraction (XRD) gives crystallographic information about materials by measuring the phase shifts caused by X-ray light with the material. X-rays are generated in an X-ray tube where high energy electrons are accelerated at a metal target, causing the emission of high energy photons that we know as X-rays [12]. Our instrument is a Bruker D8 Advance X-ray diffractometer which uses a Cu Kα X-ray source with a wavelength of 0.1542 nm. The output of an XRD scan is a spectrum with the y-axis being the intensity and x-axis is 2θ, where θ is the angle of incident X-rays on the sample. Certain peaks arise because of the phase shift of the diffracted X-ray due to the lattice spacing of the material. The diffraction follows Bragg's law:

$$n\lambda = 2d\ sin\theta \qquad \textbf{(2-1)}$$

Where n is an integer, λ the wavelength of the light, d is the spacing between crystal planes in the material, and θ is the angle of the incident light. For a certain lattice spacing, d, light reflected will be in or out of phase. If it is out of phase it interferes with itself destructively resulting in a weak signal. If the diffracted light is in phase it will constructively interfere resulting in increased intensity and a peak at that angle in the spectrum.

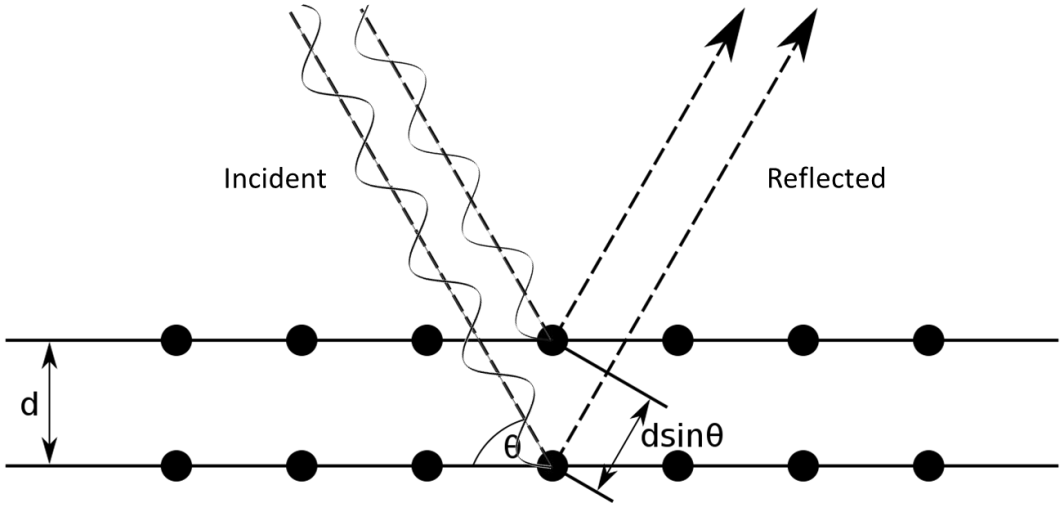

Figure 2-8. Schematic of Bragg's law with incident and reflected X-ray light from two atomic planes of a material with spacing, d.

XRD is most often used to identify the various crystal planes of elements in a sample. This can be useful to determining the state of a particular material, and the height and width of the peaks can provide further information about the relative amounts of each crystal type. In addition, the peaks can be used to determine lattice sizing or nanoparticle size using the Scherrer equation [15]:

$$d = \frac{k\lambda}{\beta \cos\theta} \qquad \textbf{(2-2)}$$

Where k is a constant, usually assumed to be ~0.9 [16], β is the full-width half-max (FWHM) of the peak of interest, and λ and θ are the same as above. Using this equation, and fitting the peak of the XRD spectrum, we can determine the average particle in sample. This is particularly useful for finding the average size of Pt nanoparticles in a catalyst sample.

2.2.6 X-Ray Photoelectron Spectroscopy

XPS is a powerful surface analysis technique that measures the energy of electrons emitted from a material upon excitation from an X-ray. An X-ray photon is directed at the sample and causes the emission of an electron from one of the atom's core shells, which are labelled K, L, M and so on. The emitted electron is called a photoelectron and it will have a very specific kinetic energy which is measured by the instrument. This energy value is the same energy that is required to eject the electron from the core and is called the binding energy [12]. Knowing the values of these binding energies, we can then identify the elements that are present in the sample by matching those of the emitted photons. Because of the relatively low energy of emitted photons, they can only escape a material if they are about 10 nm from the surface or less [12]. This is why XPS is a very surface-sensitive technique and not the ideal method for studying bulk characteristics. Low energy electron detection also requires high vacuum conditions for measurement.

The peaks at a particular binding energy for an atomic shell will be shifted to slightly higher or lower energy values when the element in question is bonded in different configurations. For instance, carbon 1s peak can occur in the range of 281-293 eV, depending on what it is bonded to [12]. Using these shifts we can identify particular bonds present in the sample. Often, a broad peak appears around the binding energies of a few bonding configurations. In this case, fitting of the peak is necessary to elucidate the exact types of bonds present, and to get quantitative data about the concentration of various elements. One example where this often proves very useful is for studying nitrogen doping in carbons. The N 1s peak occurs around eV but can be shifted depending on the bonding environment. Peaks for pyridinic, pyrrolic, and graphitic N appear at 398.1, 399.9, and 401.1 eV, respectively [17]. Fitting the measured spectrum with peaks centered at these three energies, we can determine their relative amounts from the area of each fitted peak. The fitting procedure can be very complicated so, for the sake of this thesis, all fitting and analysis of the XPS spectra was left to the surface science experts who have developed

techniques for analyzing this data. XPS analysis was done at Western Surface Science facility using a Kratos AXIS Nova spectrometer.

2.2.7 X-Ray Absorption Spectroscopy (Synchrotron)

Synchrotron radiation is a type of high energy light that arises from the motion of rapidly accelerating electrons. This change in motion causes the emission of a high energy X-ray photon. The wavelength (λ) and energy of the emitted light can be controlled by controlling the speed and motion of the electron from which it is emitted. Synchrotron radiation has several advantages over traditional X-ray excitation techniques including specific wavelength selection, super-high brightness, polarizability, short pulse times, and the ability to study samples in solid, liquid, or gas phase [18]. Generally, a particular beam-line is dedicated to either "soft X-rays" ($0.1 \leq \lambda \leq 10\ nm$), or "hard X-rays" ($0.01 \leq \lambda \leq 0.1\ nm$) [19]. As a rule of thumb, lower energy soft X-rays are suitable for studying lighter elements and high energy hard X-rays are suitable for studying heavier elements such as transition metals [20].

Though synchrotron radiation can be used for a number of analysis techniques, in the context of this thesis, the most important technique is X-ray absorption spectroscopy (XAS). XAS is the study of the change in absorption coefficient of a material with indecent X-ray photons of varying energies [21]. For an X-ray energy equal to that of the binding energy of an electron, a large change in the absorption coefficient is seen as a prominent absorption edge in the XAS spectrum. The absorption edge for a material corresponds to an atomic orbital of that element. At energies much greater than the absorption edge, scattering of the emitted photoelectron results from interactions with neighbouring atoms. This region, well beyond the absorption edge, is the extended X-ray absorption fine structure (EXAFS) region. However, energies at the pre-edge, the absorption edge, and just past the edge constitute the X-ray absorption near edge structure (XANES) region [22]. The regions where XANES and EXAFS information is extracted in shown in Figure 2-9. Notice the x and y axis are the X-ray energy and absorption coefficient, respectively. XANES analysis gives information about an atom's oxidation state, spin state, and electron

vacancies [21]. XANES analysis is done by subtracting the baseline absorption peak of a reference sample and comparing the intensity and area under the whiteline curve [23]. Mathematical methods can be used to calculate quantitative whiteline parameters but this is beyond the scope of this thesis. XANES measurements for this thesis were done at Advanced Light Source at Berkley and analysis done with the help of Dr. Mohammed Norouzi-Banis.

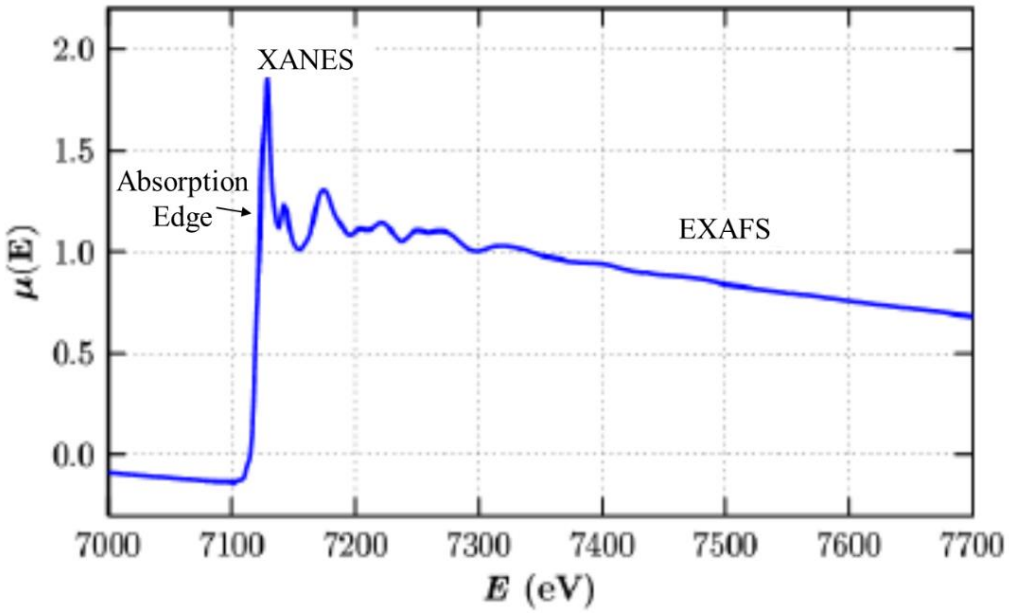

Figure 2-9. XAS spectra showing the XANES and EXAFS specific regions and highlighting the absorption edge. The vertical axis is the absorption coefficient and the horizontal axis is the x-ray energy.

2.3 Electrochemical Characterization

Cyclic voltammetry is an electrochemical measurement technique wherein the current is measured from an electrode of interest while a range of potentials is applied at a chosen rate. As outlined in the introduction section of this thesis, a three electrode cell is a common experimental apparatus used for cyclic voltammetry. In our case, the working electrode (WE) is a glassy carbon disk (diameter: 0.5 cm, Pine). The reference electrode (RE) is a mercureous sulfate electrode with saturated potassium sulfate electrolyte,

Hg/Hg_2SO_4 (K_2SO_4). The counter electrode (CE) is a Pt wire. A photograph of the three-electrode electrochemical cell used is shown in Figure 2-10.

Impurities can be one of the leading causes of poor results in electrochemical work. To minimize this, the cell was cleaned frequently with aqua-regia to remove any contaminants, followed by washing with copious amounts of ultrapure (18.2 MΩ) water. In fact, only ultrapure water is used for all aspects of the electrochemical experiments. Before testing any new catalyst, the glassy carbon electrode was polished with a dispersion of 0.05 μm alumina until a mirror-like finish was achieved. The electrolyte was prepared using high-purity sulfuric acid (99.999%, Sigma), or KOH, and ultrapure water to produce a solution of 0.5 M H_2SO_4. The RE and CE were washed with copious amounts of ultrapure water prior to placing in the cell. Both the CE and RE were placed in the cell a minimum of 30 minutes prior to any measurements to ensure the system was at equilibrium.

Inks were prepared consisting of catalyst powder, ultra-pure water, isopropanol, and a small amount of 5 wt. % Nafion solution. A new ink was sonicated 60 minutes in an ultrasonic bath before use. It should be noted that inks older than one week were never used since they are prone to particle agglomeration and generally perform poorly compared to fresh ink. Once ready, small aliquots (typically 10 μL) of ink were dropped onto the polished glassy carbon electrode and allowed to dry in air under a heat lamp.

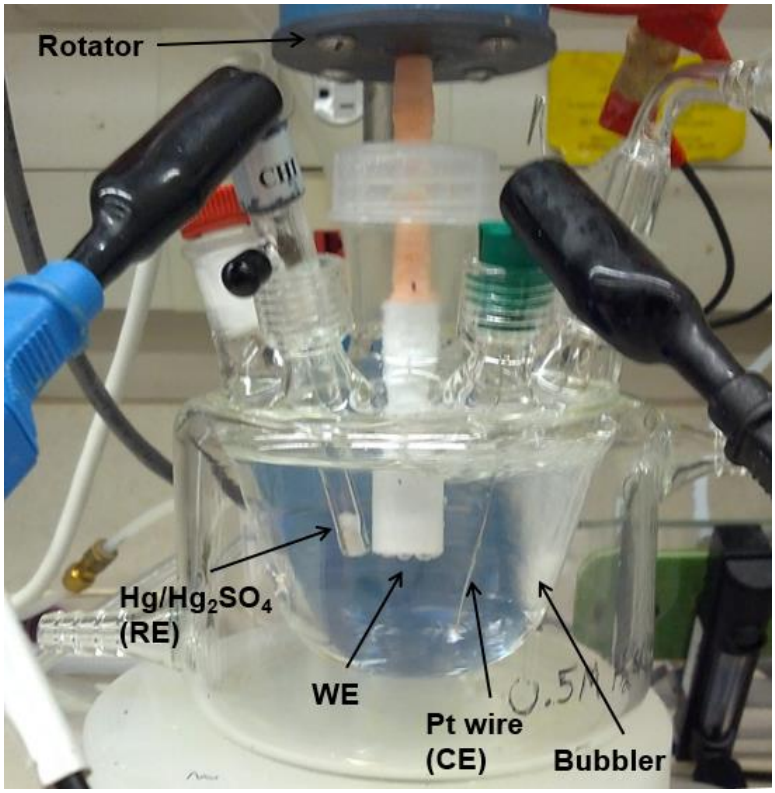

Figure 2-10. (a) Three-electrode electrochemical setup

CV measurements are first done with N_2 saturation. N_2 gas is bubbled into the electrolyte for at least 30 minutes prior to any measurements to ensure no air is in the cell. Checking for a stable open circuit voltage confirms that the cell is in a steady-state. For Pt-catalysts, 40 or more cycles are used to activate and clean a freshly made electrode. This step removes unwanted organics from the Pt surface by the repeated formation and reduction of an oxide layer and the adsorption and desorption of hydrogen. These activation cycles ensure the best possible activity measurements. Specific CV scan profiles are given in each chapter of this thesis but typically a potential window from roughly 0-1.2 V vs RHE is used with a scanning rate of 10 or 20 mV/s. To record CVs and ORR polarization curves in O_2 saturation, pure O_2 is bubbled for at least 30 minutes to ensure saturation. Again, the open circuit potential can be monitored to ensure steady state is reached in the cell. For an ORR polarization curve, using the rotating disk electrode (RDE) is the preferred method. More specifics for the electrochemical measurements made in each chapter are given in the experimental sections of that chapter.

2.4 References

[1] M. Kumar and Y. Ando, "Chemical vapor deposition of carbon nanotubes: a review on growth mechanism and mass production.," *J. Nanosci. Nanotechnol.*, vol. 10, no. 6, pp. 3739–3758, 2010.

[2] J. Liu, Y. Zhang, M. I. Ionescu, R. Li, and X. Sun, "Nitrogen-doped carbon nanotubes with tunable structure and high yield produced by ultrasonic spray pyrolysis," *Appl. Surf. Sci.*, vol. 257, no. 17, pp. 7837–7844, Jun. 2011.

[3] J. Werther, "Fluidized-Bed Reactors," in *Ullmann's Encyclopedia of Industrial Chemistry*, no. 52, 2007.

[4] R. W. Johnson, A. Hultqvist, and S. F. Bent, "A brief review of atomic layer deposition: from fundamentals to applications," *Mater. Today*, vol. 17, no. 5, pp. 236–246, Jun. 2014.

[5] O. Sneh, R. B. Clark-Phelps, A. R. Londergan, J. Winkler, and T. E. Seidel, "Thin film atomic layer deposition equipment for semiconductor processing," *Thin Solid Films*, vol. 402, no. 1–2, pp. 248–261, Jan. 2002.

[6] A. Lushington, J. Liu, Y. Tang, R. Li, and X. Sun, "Surface modification of nitrogen-doped carbon nanotubes by ozone via atomic layer deposition," *J. Vac. Sci. Technol. A Vacuum, Surfaces, Film.*, vol. 32, no. 1, p. 01A124, 2014.

[7] S. Komarneni, D. Li, B. Newalkar, H. Katsuki, and A. S. Bhalla, "Microwave - Polyol process for Pt and Ag nanoparticles," *Langmuir*, vol. 18, no. 15, pp. 5959–5962, 2002.

[8] F. Bonet, V. Delmas, S. Grugeon, R. Herrera Urbina, P. Y. Silvert, and K. Tekaia-Elhsissen, "Synthesis of monodisperse Au, Pt, Pd, Ru and Ir nanoparticles in ethylene glycol," *Nanostructured Mater.*, vol. 11, no. 8, pp. 1277–1284, 1999.

[9] A. Guha, W. Lu, T. a. Zawodzinski, and D. a. Schiraldi, "Surface-modified carbons as platinum catalyst support for PEM fuel cells," *Carbon N. Y.*, vol. 45, no. 7, pp. 1506–1517, 2007.

[10] Z. Liu, J. Y. Lee, W. Chen, M. Han, and L. M. Gan, "Physical and Electrochemical Characterizations of Microwave-Assisted Polyol Preparation of Carbon-Supported PtRu Nanoparticles," *Langmuir*, vol. 20, no. 1, pp. 181–187, 2004.

[11] A. B. A. A. Nassr, I. Sinev, M. M. Pohl, W. Grünert, and M. Bron, "Rapid microwave-assisted polyol reduction for the preparation of highly active PtNi/CNT electrocatalysts for methanol oxidation," *ACS Catal.*, vol. 4, no. 8, pp. 2449–2462, 2014.

[12] Y. Leng, *Materials characterization: introduction to microscopic and spectroscopic methods*. Chichester, UK: John Wiley & Sons, Ltd, 2008.

[13] S. Brunauer, P. H. Emmett, and E. Teller, “Adsorption of Gases in Multimolecular Layers,” *J. Am. Chem. Soc.*, vol. 60, no. 2, pp. 309–319, 1938.

[14] H. G. M. Edwards, “Raman Microscopy: Developments and Applications,” *Measurement Science and Technology*, vol. 7, no. 11. Academic Press, 2009.

[15] A. L. Patterson, “The scherrer formula for X-ray particle size determination,” *Phys. Rev.*, vol. 56, no. 10, pp. 978–982, 1939.

[16] U. Holzwarth and N. Gibson, “The Scherrer equation versus the ‘Debye-Scherrer equation’.,” *Nat. Nanotechnol.*, vol. 6, no. 9, p. 534, 2011.

[17] I. Bertóti, M. Mohai, and K. László, “Surface modification of graphene and graphite by nitrogen plasma: Determination of chemical state alterations and assignments by quantitative X-ray photoelectron spectroscopy,” *Carbon N. Y.*, Dec. 2014.

[18] “What is a Synchrotron?,” *Canadian Light Source, The University of Saskatchewan*, 2015. [Online]. Available: http://www.lightsource.ca/education/whatis.php.

[19] A. Thompson and D. Vaughan, Eds., *X-Ray Data Booklet*, 2nd ed. Lawrence Berkeley National Laboratory, 2009.

[20] G. V. Marr, Ed., “Handbook of Synchrotron Radiation - Volume 2.” North-Holland, 1987.

[21] D. C. Koningsberger and R. Prins, “X-ray absorption: principles, applications, techniques of EXAFS, SEXAFS, and XANES,” 1988.

[22] V. Briois, C. Giorgetti, F. Baudelet, A. M. Flank, M. S. Tokumoto, S. H. Pulcinelli, and C. V Santilli, “Applications of X-Ray Absorption Spectroscopy in Materials Science,” in *Spectroscopy of Emerging Materials SE - 2*, vol. 165, E. Faulques, D. Perry, and A. Yeremenko, Eds. Springer Netherlands, 2005, pp. 15–30.

[23] A. N. Mansour, J. W. Cook, and D. E. Sayers, “Quantitative technique for the determination of the number of unoccupied d-electron states in a platinum catalyst using the L2,3 x-ray absorption edge spectra,” *J. Phys. Chem.*, vol. 88, no. 11, pp. 2330–2334, 1984.

[24] Bard and Faulkner, *Electrochemical Methods: Fundamentals & Applications*, 2nd ed. John Wiley & Sons, 2001.

[25] K.-L. Hsueh, E. R. Gonzalez, and S. Srinivasan, “Electrolyte effects on oxygen reduction kinetics at platinum: A rotating ring-disc electrode analysis,” *Electrochimica Acta*, vol. 28, no. 5. pp. 691–697, 1983.

[26] K. E. Gubbins and R. D. Walker, “The Solubility and Diffusivity of Oxygen in Electrolytic Solutions,” *J. Electrochem. Soc.*, vol. 112, no. 5, p. 469, 1965.

3 Synthesis of Phosphorus and Nitrogen Co-doped Carbon Nanotubes for Metal-Free Oxygen Reduction Catalysts

Heteroatom doping in nanostructured carbon materials has become increasingly popular. Doping carbon nanotubes (CNTs) can introduce mechanical, electrical, and chemical properties that are not otherwise observed in pristine CNTs. Nitrogen doping has been by far the most popular choice for researchers as a result of the excellent functionality of N-CNTs, especially in electrochemical applications. More recently there has been some interest in doping CNTs with two or more elements, to understand the synergistic effects of co-doping. Herein we synthesize phosphorus and nitrogen co-doped CNTs (PNCNT) grown via chemical vapour deposition. Several synthesis parameters are varied to study the effects on tube morphology and the physical characteristics of the PNCNTs are studied via TEM, Raman, and XPS. It is shown that gas flow rate affects the PNCNT length and concentration of phosphorus precursor affects tube diameter. Studies by XPS, and Raman confirm the presence of phosphorus and show a modified carbon structure with both dopants compared to only nitrogen. Finally, some preliminary electrochemical results are presented indicating that PNCNTs have improved ORR activity compared to NCNTs in alkaline media, with 62% increase in current density at 0.8 V. The improved activity is attributed to the combined effect of both P and N dopants. Koutecky-Levich analysis suggests the PNCNTs catalyze ORR via a mixture of both two- and four- electron pathways.

3.1 Introduction

Electrochemical energy devices such as fuel cells and metal-air batteries are excellent candidates for addressing the ever-growing demands for reliable and renewable energy. These devices, in particular, rely on the oxygen reduction reaction (ORR) which is inherently sluggish and thus requires catalysis to meet performance standards for commercial application. Typical ORR catalysts consist of Pt or other noble metals, though these render fuel cells prohibitively expensive for many applications. Metal-free catalysts have been a long sought-after alternative to noble metal catalysts, though they have historically been unable to match the incredible catalytic activity of materials like platinum.

Doped carbons have become one of the leading family of candidate materials for metal free catalysts. Nitrogen doping, in particular, has been extensively studied over the last several years [1] and it is now widely accepted that N-doping enhances the properties of carbons especially towards ORR catalysis via modification of the physical and electronic structure of the material [2], [3]. Meanwhile, boron, sulfur and phosphorus doping have also been studied for electrochemical devices [4]. Phosphorus is one of the more difficult of these elements to dope, due in part to its large atomic radius compared with carbon. Compared to N or B, for instance, the strain induced by a P atom in an sp^2 carbon lattice is considerable due to the long P-C bond length, which may result in an out-of-plane protrusion of the P atom [5]. On the other hand, phosphorus has an electron donating nature which makes it attractive as a dopant for catalytic activities, where modification of the carbon electron structure has been shown to be one advantage of N-doped carbons [6]. On its own, phosphorus has been studied as a dopant in CNTs [7], [8] graphene [9], [10], and mesoporous carbons [11], [12]. In several of these cases it has been shown that P-doping can effectively improve the ORR activity of the carbon compared with an un-doped counterpart.

Co-doping nitrogen and phosphorus has been very recently studied in several instances. Few groups have reported the synthesis of co-doped P and N graphene [13], [14]. Cruz-Silva performed density functional theory analysis of P and N co-doped CNTs and showed that the presence of an N dopant atom adjacent to a P-dopant can act to reduce the lattice strain in the carbon, potentially making co-doping easier than doping only phosphorus [5].

The same group [15], and others [16], [17] have synthesized PNCNTs. Here we report synthesis of PNCNTs and examine the effects of CVD process parameters. The morphology and physical structure of PNCNTs is studied by scanning electron microscopy (SEM), transmission electron microscopy (TEM), and Raman spectroscopy. XPS results show the presence of phosphorus and nitrogen at the surface of PNCNTs and provide concentrations of each. Finally, the ORR activity of the PNCNTs in alkaline media was tested and compared to that of NCNTs in order to determine the effect of phosphorus on the activity of these metal-free catalysts. Koutecky-Levich analysis shows a mixed two and four electron ORR pathway catalyzed by PNCNTs.

3.2 Experimental

3.2.1 Sample Preparation

PNCNTs were prepared via floating catalyst CVD method using ferrocene (98%, Aldrich) as the catalyst with triphenyl-phosphine (TPP) (99%, Sigma) and imidazole (99%, Sigma) as the P and N sources, respectively. Both precursors also provided the carbon for CNT growth. Imidazole and TPP (0.5, 1.5, 2.5, and 5.0 wt.%) were placed in a small quartz crucible for 2000 mg total precursor mixture. 20 mg of ferrocene was placed in a small holder, separate from the precursors, on the quartz crucible. The substrate alumina crucible was placed in the center of a quartz tube in a tube furnace. The precursors were placed near the opening of the furnace and Ar gas was flowed through the tube for 20 minutes to remove air. The temperature was raised to 850°C, at which point the ferrocene and the precursors were evaporated and transferred to the substrate by the Ar flow. The substrates were kept at the set temperature for 10 minutes and then cooled to room temperature with continued Ar flow. The PNCNTs were scraped from the soot built up on the substrate. NCNTs were prepared by the same method with only 2000 mg imidazole.

3.2.2 Physical Characterization

The morphology and structure of the nanomaterials were studied using scanning electron microscope (Hitachi S-4800 field-emission - SEM) and transmission electron

microscope (JOEL 2010F - TEM). X-ray diffraction (XRD) pattern was obtained using a Bruker D8 Advance using a Cu-Kα source. Raman spectrum was measured using a HORIBA Scientific LabRAM HR Raman spectrometer system with a 532.4 nm laser at room temperature.

3.2.3 Electrochemical Measurements

Catalyst ink consisted of 3 mg of the prepared catalyst plus 588 µL of isopropanol and 12 µL of 5 wt. % Nafion solution (Ion Power) for a 5 mg/mL solution. The ink was sonicated for 60 minutes in an ultrasonic bath at room temperature. Four 5 µL aliquots of the catalyst ink were dropped onto a polished glassy carbon (GC) electrode (Pine, 5 mm diameter) and dried under a heat lamp. After the last aliquot had dried, a small amount of ultrapure water was dropped onto the electrode to improve wetting in the electrochemical cell. The prepared GC electrode with catalyst served as the working electrode. A Pt wire and $Hg/HgSO_4$ electrode were used as the counter and reference electrodes, respectively. A correction of -0.658 V vs. RHE was used for the $Hg/HgSO_4$ electrode and all potentials henceforth are given with respect to RHE. Measurements were done using a standard potentiostat (AutoLab). All measurements were done at room temperature using 0.1 M KOH electrolyte prepared with Milli-pure water (18.2 $M\Omega/cm^2$) and high purity KOH (>99.9%, Aldrich). CVs were measured under high purity N_2 or O_2 saturation, cycled from 0.05-1.2 V at 10 mV/s. ORR curves were taken under O_2 saturation which was achieved by bubbling O_2 for a minimum of 20 minutes. The electrode was rotated at 1600 RPM and potential scanned from 0.05-1.2 V at 10 mV/s.

3.3 Results

Synthesis of PNCNTs was carried out using a floating catalyst CVD method as described previously [18]. Based on this setup several parameters were found to play important roles on the formation of PNCNTs. The flow of Ar gas carries both catalyst and precursor to the substrate, making it an important parameter for tube growth. We varied the inlet gas flow between 0.85 and 1.72 SLPM to find good growth conditions. Figure 3-1 shows bundles of PNCNTs made at different gas flow rates. The tubes grown at 0.85 SLPM

are very short compared to those at higher rates, suggesting that a higher rate is needed to ensure good mass transport to the substrate. The yield was also extremely low at 0.85 SLPM. At higher flow rates the length is >50 μm and bundles with widths from 5-40 μm were common in each case. Ar flow above 1.72 SLPM led to a build-up of excess precursor vapour at the exhaust end of the tube, resulting in poor nanotube growth. The length of tubes appears to be a function of the gas flow rate, as seen in Figure 3-2(a).

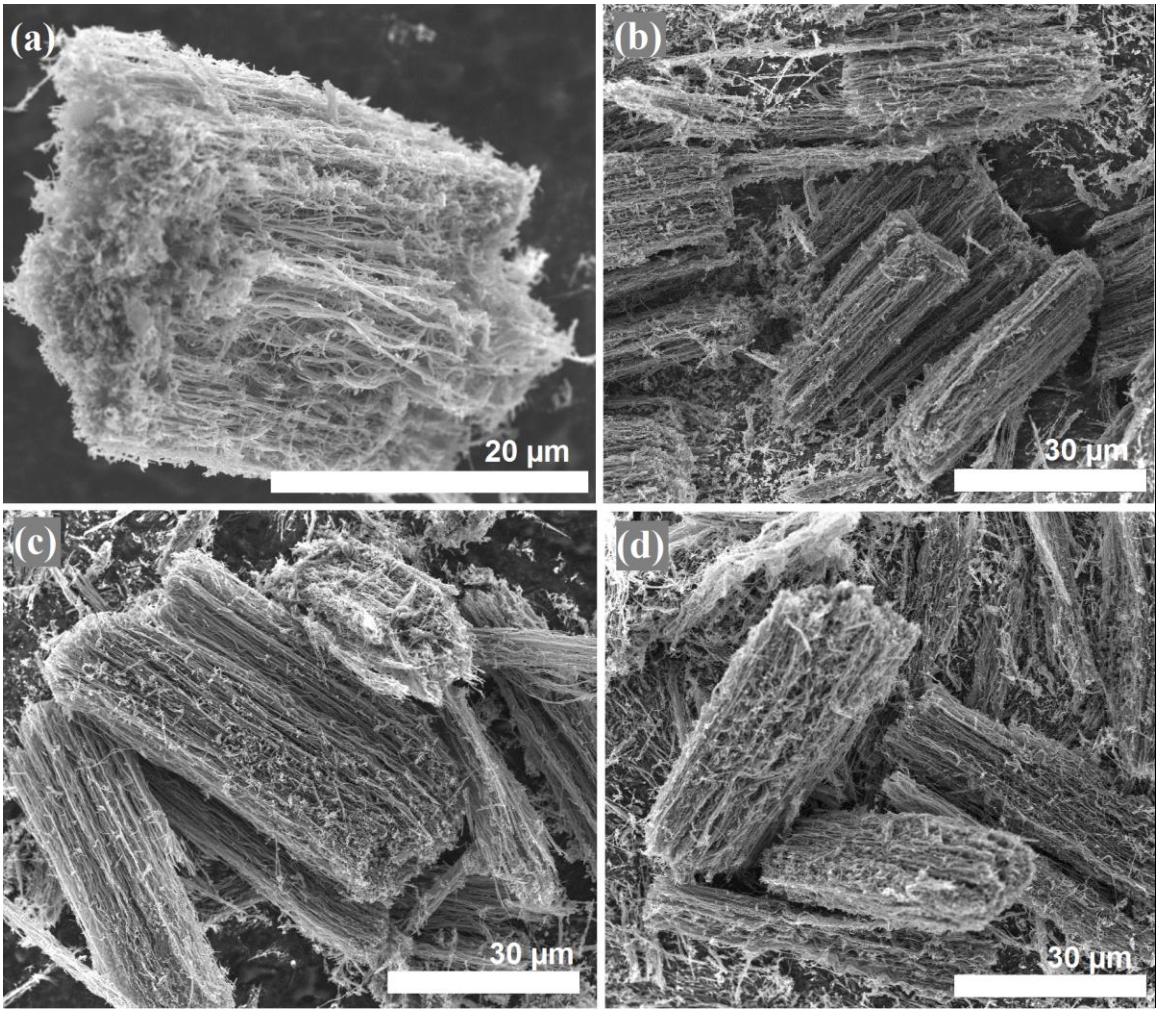

Figure 3-1. PNCNTs synthesized with Ar flows of 0.85 (a), 1.17 (b), 1.46 (c), 1.72 (d) SLPM.

The length of tubes roughly increases with the flow rate, with a maximum of 61 μm at 1.46 SLPM, and a slightly decrease to 54 μm at 1.72 SLPM. This result is intuitive as the increased gas flow improves mass transport of the vaporized precursor materials. On the other hand, the gas flow has no apparent effect on the diameter of the tubes (Figure 3-2(a)). This can be understood because the tube diameter is related mainly to the catalyst particle

size and the nature of the precursor's chemical structure [19]. Despite the slightly longer tube length at 1.46 SLMP, we chose to use 1.72 SLPM for subsequent experiments because the overall yield was better at this flow rate.

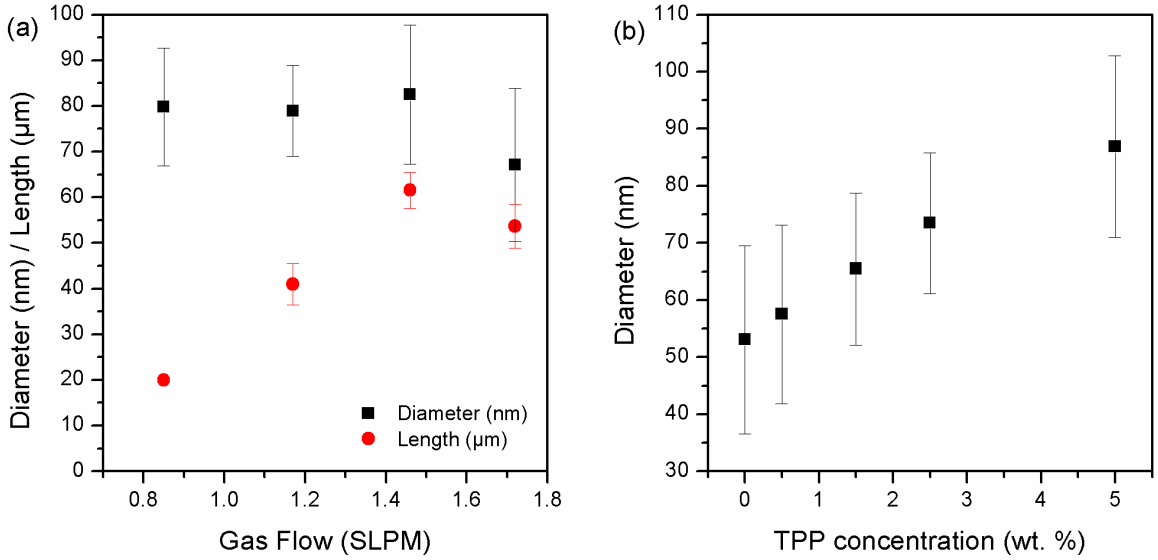

Figure 3-2. (a) Average PNCNT diameter (in nm) and length (in μm) for various Ar flow rates with precursor TPP concentration of 2.5 wt. %. (b) Average diameter of PNCNTs as a function of the TPP concentration in the precursor mixture, grown with 1.72 SLPM Ar flow.

With the chosen gas flow rate, we proceeded to synthesize PNCNTs with varying amounts of TPP precursor, from 0-5 wt. %. The effect of TPP precursor on the quality and diameter of nanotubes was studied by examining more than 200 nanotubes for each concentration under SEM. The results indicated that increasing the concentration of TPP resulted in an increase in the average tube diameter, as seen in Figure 3-2(b). Error bars represent one standard deviation. This increase may be a result of increased wall thickness, as others have observed [16], [18]. At 5 wt. % TPP, the quality of nanotubes was very poor compared to lower concentrations, with SEM images showing significant amorphous carbon. PNCNTs referred to herein were prepared with 2.5 wt. % TPP at 1.72 SLPM.

TEM images of NCNTs and PNCNTs are shown in Figure 3-3. The bamboo-like structure, which is characteristic of NCNTs [20], [21], is clearly seen in the TEM images

of those and the PNCNTs. Interestingly, there appear to be two types of tubes in Figure 3-3(b), one with a narrow channel and very thick walls (centered and right), and a second type with a wider channel (left side of image). This phenomenon also recently observed by Nicolls et al [16]. Thick walls and a thin channel are seen in Figure 3-3(c) which also shows some amorphous carbon build-up on the PNCNT. A high-magnification image of the wall of a PNCNT is shown in Figure 3-3(d). The wall thickness is ~30 nm and appears to have only short range order. Furthermore, the carbon planes are not perfectly parallel and have varying interplanar distances greater than that of pristine sp^2 carbon, indicative of disorder in the carbon lattice likely caused by the presence of heteroatoms.

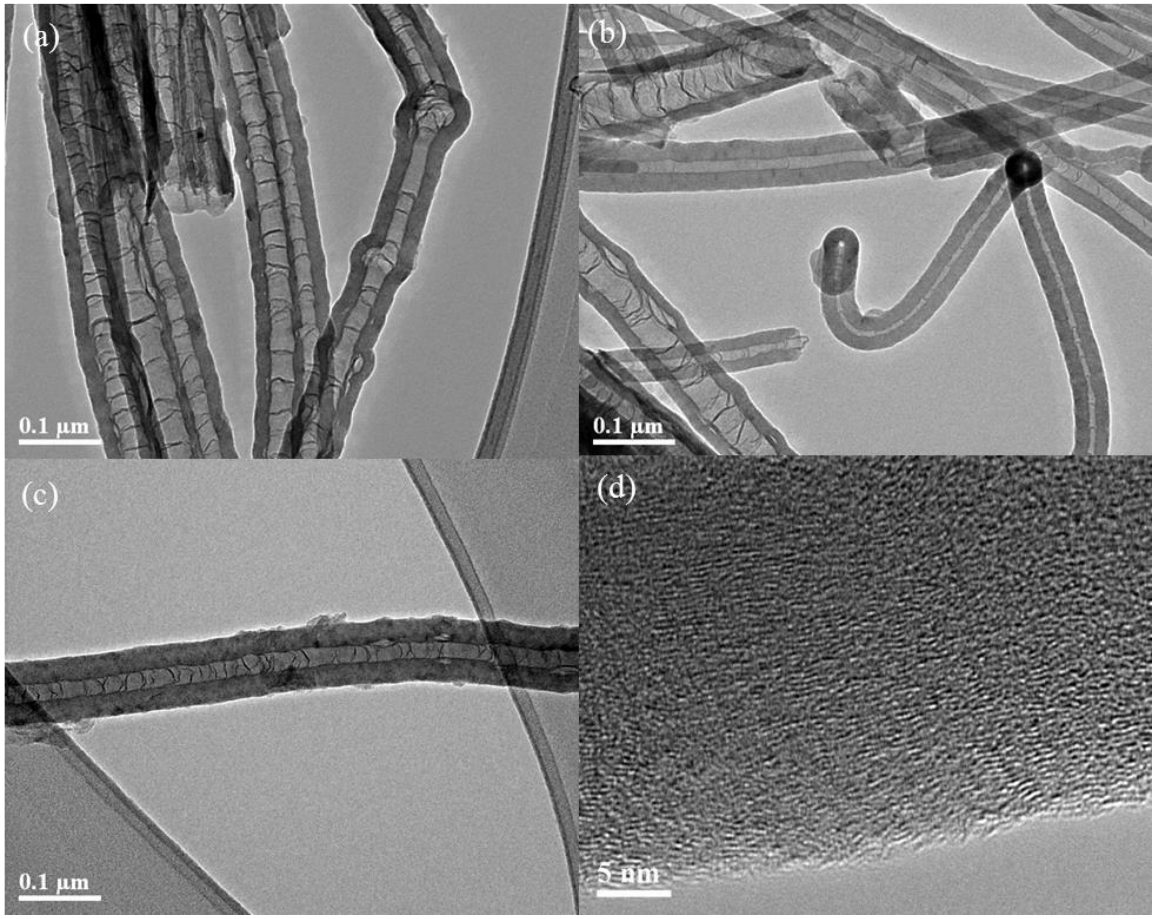

Figure 3-3. TEM images of (a) NCNTs and (b,c) PCNTs. (d) HR-TEM image of the nanotube wall in PCNTNs.

Raman spectroscopy was used on the PNCNTs and NCNTs to better understand the effects of the dopants on the carbon structure of the nanotube and determine their relative

amounts of ordered and disordered carbon. The spectra of PNCNTs and CNTs are shown in Figure 3-4. The G-band intensity, which normally occurs around 1582 cm^{-1} in pristine CNTs, correlates to highly ordered, sp^2-type carbon resulting from the lateral vibrations of C-C bonds in a ring. The D-band, around 1350 cm^{-1}, correlates to disordered carbon. In order to find a relative amount of amorphous to ordered carbon, one can compare the ratios of the D and G-band peak areas to find the value I_D/I_G. The I_D/I_G ratio for NCNTs and PNCNTs are 2.08 and 2.70, respectively. From this result, it appears that P dopants increase the disordered nature of the CNTs, including the amount of amorphous carbon, compared to N-only doping. In addition, the G-band is down-shifted from 1580 cm^{-1} in NCNTs to 1565 cm^{-1} in PNCNTs, which may be due to the additional stretching of C–C bonds in the vicinity to the large phosphorus atoms compared to the distortions caused by only nitrogen dopants, and may be indicative of changes to the electronic bonding structure [22].

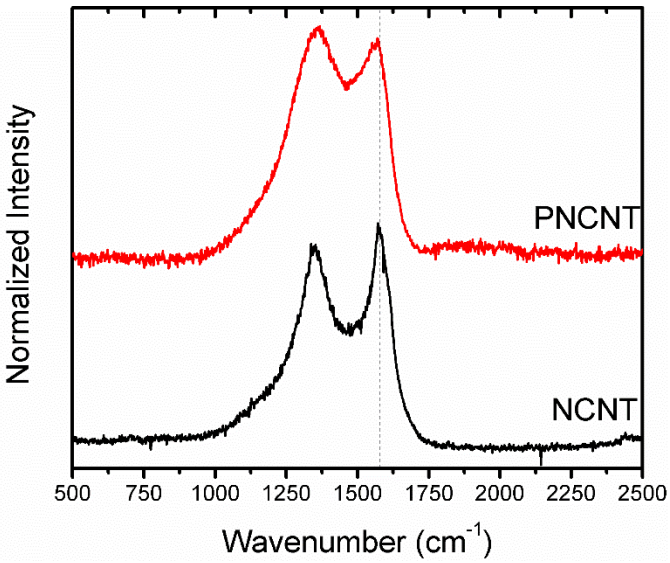

Figure 3-4. Raman spectra of NCNTs and PNCNTs

An X-ray photoelectron spectroscopy (XPS) survey was done to determine the chemical composition of NCNTs and PNCNTs. The spectra for each are shown in Figure 3-5(a). The concentrations of various elements in each species is given in Table 3-1. The nitrogen content in each sample is the same (6.2 at. %) suggesting that other differences in the chemical and electrochemical properties of the PNCNTs may be attributed to the presence of the phosphorus, of which there is 1.1 at. %. This phosphorus content is in line

with aforementioned literature values for similarly doped carbon nanomaterials. A fitting method was used to deconvolute the N 1s and P 2p peaks in each sample. By doing so it is possible to determine the bonding nature of nitrogen and phosphorus, respectively. The high-resolution N 1s peaks for NCNT and PNCNT are shown in Figure 3-5(b) and (c), respectively. There are two peaks within the N 1s signal. The peak centered at 398.1 eV corresponding to pyridinic N and the peak at 400.8 eV corresponding to quaternary (graphitic) N. Interestingly, the ratio of graphitic to pyridinic nitrogen is higher in the PNCNTs which suggests that the presence of the phosphorus may play a role in promoting higher energy nitrogen species during doping. A high-resolution P 2p peak from the PNCNT sample is shown in Figure 3-5(d). In this case there are two peaks each at higher and lower energy corresponding to P^0 and P–O bonding, respectively. The double peak is due to orbital splitting between $2p_{3/2}$ and $2p_{1/2}$ which is highlighted with the dashed line. Although many claim that the lower energy P 2p peak at 130-132 eV corresponds to P–C bonding, it has been importantly noted that evidence of P–C bonds from XPS data is somewhat ambiguous [23], [24]. We can say that the peak centered around 130.2 eV corresponds to a P^0 state, while that at 132.4 eV corresponds to phosphate-type P–O bonding. It may be that the slightly increase oxygen content in the PNCNTs is a result of phosphate groups at the surface.

Table 3-1. Composition of NCNT and PNCNTs determined by XPS analysis

Element	NCNT (at. %)	PNCNT (at. %)
C	90.3	88.7
O	2.8	3.8
N	6.2	6.2
P	–	1.1

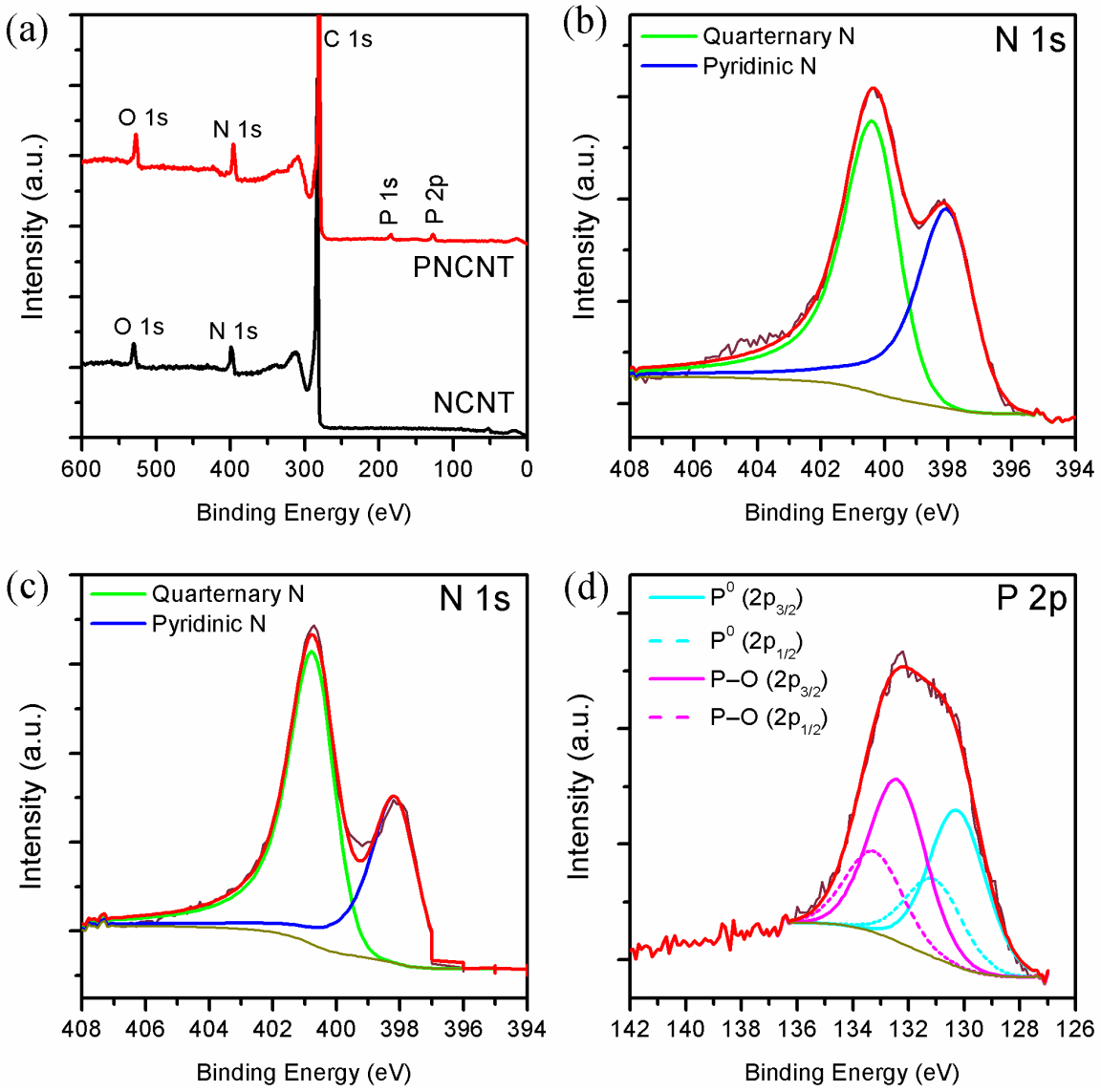

Figure 3-5. XPS survey spectra for PNCNTs and NCNTs (a). High resolution N 1s peak for NCNT (b) and PNCNT (c), and high-resolution P 2p peak for PNCNTs (d).

PNCNTs are potentially attractive materials for metal-free catalysis of ORR. To understand the difference in catalytic activity of PNCNTs and NCNTs, the two materials were tested using RDE in 0.1 M KOH electrolyte at room temperature. An equal amount of material, 0.81 mg/cm^2, was deposited onto the glassy carbon electrode for comparison. CV curves were recorded at 10 mV/s in O_2 saturated electrolyte, and are shown in Figure 3-6(a). There is an increased current density at the ORR peak around 0.62 V for the PNCNT sample compared to NCNTs, indicating higher catalytic activity. In addition, the double

layer capacitance appears slightly larger for PNCNT, as seen in the wider region of the CV below 0.5 V. This could be a result of slightly increased surface area or surface roughness. Further comparison of the two nanotube materials was done by evaluating their ORR activity by linear sweep voltammetry. The polarization curves shown in Figure 3-6(b) were recorded at 1600 RPM with a scan rate of 10 mV/s. While the two curves are similar, it can be seen that the PNCNTs show higher current density throughout. The onset potentials of NCNTs and PNCNTs are 0.85 V and 0.90 V, respectively. The higher onset potential demonstrates improved activity of the co-doped catalyst, further confirming that the presence of phosphorus and nitrogen together results in good ORR catalysis. At 0.8 V, PNCNTs have a current density of -0.21 mA/cm_2 which is 62% greater than NCNTs with a current density of -0.13 mA/cm^2 at the same potential. High current density in the kinetic region is highly desirable as it translates to a high operating potential in a fuel cell. Using the kinetic current, i_k, and normalizing to the catalyst loading, the mass activity of PNCNTs and NCNTs at 0.8 V are 0.24 mA/mg and 0.15 mA/mg, respectively, revealing a 62% improvement in mass activity for PNCNTs compared to NCNTs. In addition to the presence of additional phosphorus surface groups and synergistic effects of P and N co-doping, the higher current density compared to NCNTs may be attributed to surface heterogeneity in the PNCNTs that contribute to improved ORR catalysis.

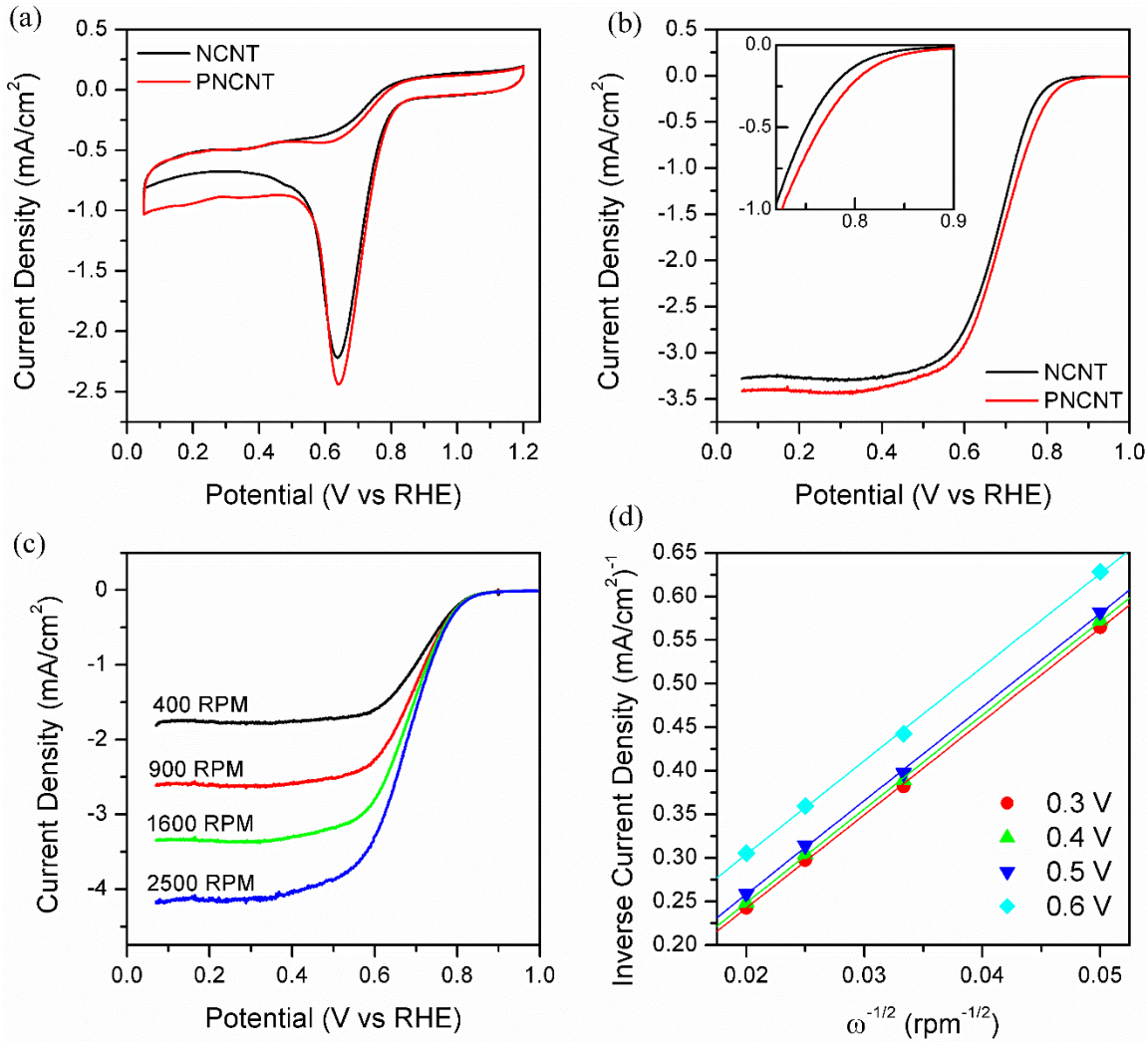

Figure 3-6. (a) CVs recorded in O_2 saturated 0.1 M KOH solution for NCNTs and PNCNT (b) ORR polarization curves for NCNT and PNCNT recorded at 1600 RPM. (c) ORR curves for PNCNT at various rotation rates. (d) Koutecky-Levich plot from data in (c).

In Figure 3-6(c) the ORR curves of PNCNTs recorded at 400, 900, 1600, and 2500 RPM are shown. The plot illustrates flat mass-transport region at each rotation rate. A Koutecky-Levich plot was prepared using the data from the ORR curves at varying rotation rates, ω, wherein the inverse current density, at several potentials is plotted against, $\omega^{-1/2}$. This is shown in Figure 3-6(d). The highly linear and parallel fit of the points for each potential value indicating first-order rate kinetics with respect to O_2 [25]. Using the same ORR data, the number of electrons transferred for each oxygen molecule, n, can be calculated using the Levich equation:

$$j_{\text{lim}} = 0.201nFACD^{2/3}\nu^{-1/6}C\omega^{1/2} \quad \textbf{(3-1)}$$

Where j_{lim} is the diffusion limiting current, F is Faraday's constant, A is the electrode area, C is the concentration of O_2 in electrolyte, D is the diffusion coefficient of oxygen in the electrolyte, ν is the kinematic viscosity of the electrolyte (assumed to be equal to water). The average value of n at 400 RPM is 3.0, while the average value of n at 2500 RPM is 2.7. This slight inconsistency may suggest a two-step reaction is taking place where the second step proceeds more slowly than the first [26]. Since the ORR reaction involves either a two or four electron transfer, these values suggests that there is a combination of ORR mechanisms at work on PNCNTs. One pathway is the direct reduction of O_2 to H_2O (4 electron), and the other is a reduction first to H_2O_2 (2 electron). Further studies with rotating ring disk electrode (RRDE) could elucidate more information on the exact ratio of H_2O to H_2O_2 production at the electrode.

3.4 Conclusions

PNCNTs were synthesized via floating catalyst CVD and grown on alumina substrates. It was found that, using this method, the length of PNCNTs could be controlled by adjusting the gas flow rate and that increased concentration of TPP in the precursor blend resulted larger tube diameters. Furthermore, PNCNTs had thicker tube walls and narrow central cavities compared to NCNTs. XPS confirmed the presence of phosphorus and Raman analysis showed an increase in disordered carbon in the co-doped sample compared to nitrogen doped only. Measurements of PNCNTs in alkaline solution showed a higher onset potential for ORR and 62% increase in current density at 0.8 V compared with NCNTs, indicating that co-doping with phosphorus and nitrogen can improve the catalytic activity of CNTs more than doping with nitrogen alone. Additional testing of the ORR activity in acidic media, and a study of PNCNTs as a Pt-catalyst support would be good candidates for future studies.

3.5 References

[1] L. F. Mabena, S. Sinha Ray, S. D. Mhlanga, and N. J. Coville, "Nitrogen-doped carbon nanotubes as a metal catalyst support," *Appl. Nanosci.*, vol. 1, no. 2, pp. 67–77, May 2011.

[2] Y. Shao, S. Zhang, M. H. Engelhard, G. Li, G. Shao, Y. Wang, J. Liu, I. a. Aksay, and Y. Lin, "Nitrogen-doped graphene and its electrochemical applications," *J. Mater. Chem.*, vol. 20, no. 35, p. 7491, 2010.

[3] L. Qu, Y. Liu, J.-B. Baek, and L. Dai, "Nitrogen-doped graphene as efficient metal-free electrocatalyst for oxygen reduction in fuel cells.," *ACS Nano*, vol. 4, no. 3, pp. 1321–6, Mar. 2010.

[4] J. P. Paraknowitsch and A. Thomas, "Doping carbons beyond nitrogen: an overview of advanced heteroatom doped carbons with boron, sulphur and phosphorus for energy applications," *Energy Environ. Sci.*, vol. 6, no. 10, p. 2839, 2013.

[5] E. Cruz-Silva, F. López-Urías, E. Muñoz-Sandoval, B. G. Sumpter, H. Terrones, J. Charlier, V. Meunier, and M. Terrones, "Electronic transport and mechanical properties of phosphorus- and phosphorus-nitrogen-doped carbon nanotubes.," *ACS Nano*, vol. 3, no. 7, pp. 1913–21, Jul. 2009.

[6] R. Czerw, M. Terrones, J. C. Charlier, X. Blase, B. Foley, R. Kamalakaran, N. Grobert, H. Terrones, D. Tekleab, P. M. Ajayan, W. Blau, M. Rühle, and D. L. Carroll, "Identification of Electron Donor States in N-Doped Carbon Nanotubes," *Nano Lett.*, vol. 1, no. 9, pp. 457–460, 2001.

[7] Z. Liu, F. Peng, H. Wang, H. Yu, J. Tan, and L. Zhu, "Novel phosphorus-doped multiwalled nanotubes with high electrocatalytic activity for O2 reduction in alkaline medium," *Catal. Commun.*, vol. 16, no. 1, pp. 35–38, Nov. 2011.

[8] D. G. Larrude, M. E. H. Maia da Costa, F. H. Monteiro, a. L. Pinto, and F. L. Freire, "Characterization of phosphorus-doped multiwalled carbon nanotubes," *J. Appl. Phys.*, vol. 111, no. 6, p. 064315, 2012.

[9] C. Zhang, N. Mahmood, H. Yin, F. Liu, and Y. Hou, "Synthesis of phosphorus-doped graphene and its multifunctional applications for oxygen reduction reaction and lithium ion batteries.," *Adv. Mater.*, vol. 25, no. 35, pp. 4932–7, Sep. 2013.

[10] R. Li, Z. Wei, X. Gou, and W. Xu, "Phosphorus-doped graphene nanosheets as efficient metal-free oxygen reduction electrocatalysts," *RSC Adv.*, vol. 3, no. 25, p. 9978, 2013.

[11] D.-S. Yang, D. Bhattacharjya, S. Inamdar, J. Park, and J.-S. Yu, "Phosphorus-doped ordered mesoporous carbons with different lengths as efficient metal-free electrocatalysts for oxygen reduction reaction in alkaline media.," *J. Am. Chem. Soc.*, vol. 134, no. 39, pp. 16127–30, Oct. 2012.

[12] D.-S. Yang, D. Bhattacharjya, M. Y. Song, and J.-S. Yu, “Highly efficient metal-free phosphorus-doped platelet ordered mesoporous carbon for electrocatalytic oxygen reduction,” *Carbon N. Y.*, vol. 67, pp. 1–8, Nov. 2013.

[13] R. Li, Z. Wei, and X. Gou, “Nitrogen and Phosphorus Dual-doped Graphene/Carbon Nanosheets as Bifunctional Electrocatalysts for Oxygen Reduction and Evolution,” *ACS Catal.*, p. 150527131058003, 2015.

[14] X. Ma, G. Ning, C. Qi, C. Xu, and J. Gao, “Phosphorus and nitrogen dual-doped few-layered porous graphene: a high-performance anode material for lithium-ion batteries.,” *ACS Appl. Mater. Interfaces*, vol. 6, no. 16, pp. 14415–22, Aug. 2014.

[15] E. Cruz-Silva, D. A. Cullen, L. Gu, J. M. Romo-Herrera, E. Muñoz-Sandoval, F. López-Urías, B. G. Sumpter, V. Meunier, J. Charlier, D. J. Smith, H. Terrones, and M. Terrones, “Heterodoped nanotubes: theory, synthesis, and characterization of phosphorus-nitrogen doped multiwalled carbon nanotubes.,” *ACS Nano*, vol. 2, no. 3, pp. 441–8, Mar. 2008.

[16] R. J. Nicholls, Z. Aslam, M. C. Sarahan, A. M. Sanchez, F. Dillon, A. a Koós, P. D. Nellist, and N. Grobert, “Morphology - composition correlations in carbon nanotubes synthesised with nitrogen and phosphorus containing precursors.,” *Phys. Chem. Chem. Phys.*, vol. 17, no. 3, pp. 2137–42, Jan. 2015.

[17] D. Yu, Y. Xue, and L. Dai, “Vertically Aligned Carbon Nanotube Arrays Co-doped with Phosphorus and Nitrogen as Efficient Metal-Free Electrocatalysts for Oxygen Reduction,” *J. Phys. Chem. Lett.*, vol. 3, no. 19, pp. 2863–2870, Oct. 2012.

[18] J. Liu, H. Liu, Y. Zhang, R. Li, G. Liang, M. Gauthier, and X. Sun, “Synthesis and characterization of phosphorus–nitrogen doped multiwalled carbon nanotubes,” *Carbon N. Y.*, vol. 49, no. 15, pp. 5014–5021, Dec. 2011.

[19] H. Dai, “Carbon nanotubes: synthesis, integration, and properties.,” *Acc. Chem. Res.*, vol. 35, no. 12, pp. 1035–44, Dec. 2002.

[20] K. Gong, F. Du, Z. Xia, M. Durstock, and L. Dai, “Nitrogen-doped carbon nanotube arrays with high electrocatalytic activity for oxygen reduction.,” *Science*, vol. 323, no. 5915, pp. 760–4, Feb. 2009.

[21] Z. Chen, D. Higgins, H. Tao, R. S. Hsu, and Z. Chen, “Highly Active Nitrogen-Doped Carbon Nanotubes for Oxygen Reduction Reaction in Fuel Cell Applications,” *J. Phys. Chem. C*, vol. 113, no. 49, pp. 21008–21013, Dec. 2009.

[22] M. S. Dresselhaus, A. Jorio, M. Hofmann, G. Dresselhaus, and R. Saito, “Perspectives on carbon nanotubes and graphene Raman spectroscopy.,” *Nano Lett.*, vol. 10, no. 3, pp. 751–8, Mar. 2010.

[23] J. C. Han, a. P. Liu, J. Q. Zhu, M. L. Tan, and H. P. Wu, “Effect of phosphorus content on structural properties of phosphorus incorporated tetrahedral amorphous carbon films,” *Appl. Phys. A*, vol. 88, no. 2, pp. 341–345, 2007.

[24] F. Claeyssens, G. M. Fuge, N. L. Allan, P. W. May, and M. N. R. Ashfold, “Phosphorus carbides: theory and experiment.,” *Dalton Trans.*, no. 19, pp. 3085–3092, 2004.

[25] N. Anastasijević, V. Vesović, and R. Adžić, “Determination of the kinetic parameters of the oxygen reduction reaction using the rotating ring-disk electrode: Part I. Theory,” *J. Electroanal. Chem.*, vol. 229, pp. 305–316, 1987.

[26] S. Treimer, A. Tang, and D. C. Johnson, “A consideration of the application of Koutecky-Levich plots in the diagnoses of charge-transfer mechanisms at rotated disk electrodes,” *Electroanalysis*, vol. 14, no. 3, pp. 165–171, 2002.

4 Effects of Ammonia and Ozone Treatment for Carbon Black Supported Pt Electrocatalysts

The long term commercial success of proton exchange membrane fuel cells is still heavily dependent on reducing their costs and improving performance. The platinum catalyst still accounts for a large portion of fuel cell system costs and is one that will not decrease with large scale manufacturing. Tremendous research efforts have bene made towards lowering costs and increasing the utilization of Pt, especially at the cathode, where sufficient Pt is necessary to catalyze the otherwise sluggish oxygen reduction reaction (ORR). Using modified carbon support materials has been shown to offer several benefits include several benefits including improved Pt stability and corrosion resistance. Herein, we compare a commercial Pt on carbon black (Pt/CB) sample to similar catalyst supported by ozone treated (O3-CB) and ammonia treated carbon black (NH3-CB). SEM, TEM, and XRD analysis of Pt nanoparticles deposited on each support show good distribution and small size on both modified CBs, while gas-sorption and XPS confirm the presence of functional groups on the supports. Half-cell electrochemical tests confirm the mass activity of the modified CB supported catalysts increases in the order Pt/CB < Pt/NH3-CB < Pt/O3-CB, with an 18% increase in mass activity for Pt/O3-CB over Pt/CB. Further, Pt/O3-CB offers improved durability in the fuel cell operating potential range compared to Pt/CB, with only 7% mass activity loss after durability testing. This work demonstrates a facile, one-step treatment method for modifying a low-cost CB support to be used as Pt-supported catalyst with improved catalytic activity and durability.

4.1 Introduction

Lowering the cost of proton exchange membrane fuel cells (PEMFC) is one of the paramount challenges to the long-term success of the energy-converting technology. Because of the sluggish kinetics of the cathodic oxygen reduction reaction (ORR), platinum (Pt) based catalysts are used in PEMFCs to achieve acceptable performance. While significant reductions in Pt loadings have been made in the last decade, the catalyst still accounts for a significant portion of the FC cost; one that will not decrease with projected economies of scale [1]. Additionally, the long-term operation of the FCs is critical for their role in vehicle powertrains, where lifetimes of roughly 5000 hours is needed with minimal performance loss. Some of the main mechanisms of catalyst activity loss in PEMFCs include support corrosion, particle agglomeration, and Pt dissolution [2]. In this respect, considerable research efforts have been made for increasing the activity of Pt catalysts and improving their stability [3]. Despite the many catalyst architectures proposed, Pt nanoparticles supported on carbon black remain the state-of-the-art for PEM fuel cell catalysts. The role of the support has been studied in depth [4], [5] and a variety of other materials including carbon nanotubes (CNTs) [6], graphene [7], and metal oxides [8], have been shown to be good candidates. To date, however, none of these advanced nanostructured supports has been extensively used in commercial FC stacks because their cost and difficult synthesis compared to carbon black remains a barrier.

Typically, carbon black is prone to corrosion at high electrode potentials when oxidation to CO and CO_2 are observed [9]. This is especially problematic during start-up and shut-down of the FC when electrode potentials can reach up 1.5 V or higher. With advances in FC controls and engineering systems, the corrosion of carbon supports during start-up and shut-down can be mitigated to some extent. An excellent review of these system strategies for reducing carbon corrosion has been published [10], and more recently, Yu and colleagues present a table of the FC system strategies employed by major fuel cell companies for limiting carbon corrosion and cell reversal [11]. Besides carbon corrosion, Pt dissolution and particle migration will occur in the potential range from 0.6-1.0 V which is the operating range of a PEMFC [12]. Hence, there remains a need for developing catalysts which are more immune to Pt dissolution and migration. The use of novel support

materials with increased interactions between the particles and support material have been shown to be effective in this regard [13]–[15].

Modification of the carbon support surface with functional groups can be an effective way to improve catalyst activity and durability. Previous studies have shown that the ozone treatment can increase the acidity of carbon surfaces [16], which promotes good deposition and adhesion of Pt particles due to interactions between the surface groups and precursor Pt salt [17], [18]. It has also been reported that increasing the surface heterogeneity of a carbon sample can improve the dispersion of Pt particles on its surface [19]. Recently, our group used atomic layer deposition (ALD) to treat nitrogen-doped CNTs (NCNT) with ozone and found that a non-destructive surface treatment could be applied by varying the temperature and number of cycles [20].

Meanwhile, nitrogen doping has been thoroughly studied especially for graphene [21] and carbon nanotubes [22], [23], and to some extent, carbon black [24]–[26]. Nitrogen doped carbons have proven to be effective catalyst supports because of their density of high energy binding sites for Pt [28], and for the electronegative nature of nitrogen which can promote good activity towards ORR. Ammonia treatment of carbon black has been shown to increase the catalytic activity of the carbon itself towards the oxidation of sulfuric acid [27]. Further, carbon black treated with urea and selenourea was shown to have good ORR activity in acidic solution [25]. Carbon black functionalized via pyrolysis with polyaniline has been studied as a metal-free catalyst in methanol fuel cells [24]. Another group used 4-aminomethypyridine to functionalize Vulcan carbon and found the product to be a good support for small and disperse Pt particles.

Herein we report the modification of a commercially available, high surface area carbon black via one step treatment with either ozone or ammonia. The purpose of this study was to evaluate pre-treatment of carbon black using either ammonia or ozone and its effects on the carbon surface, the dispersion of Pt nanoparticles, and any changes in the ORR activity and catalyst durability. Gas phase ammonia treatment was done at via high temperature annealing, while ozone treatment was done via pulsed exposure in an ALD system. These carbons were characterized via N_2 gas-sorption and X-ray photoelectron

spectroscopy (XPS). Subsequently, Pt nanoparticles were deposited on the carbon samples via microwave-assisted polyol method in ethylene glycol (EG). The prepared catalysts were examined by scanning electron microscopy (SEM), transmission electron microscopy (TEM), and X-ray diffraction spectroscopy (XRD) to determine the Pt particle size, distribution, and crystal information. X-ray absorption near edge structure (XANES) analysis was also done at the Pt L_3-edge to identify any effects of support treatment on the electronic state of Pt. Finally, the catalysts were tested via thin-film rotating disk electrode (RDE) in a half-cell reaction to determine their catalytic activities towards ORR, and subjected to accelerated stress tests (AST) to study their durability in the load-cycle potential range. Using a one-step treatment and a low-cost, widely available support material is attractive for commercial purposes and any improvements as a result of such treatment could be a value-added step in the preparation of new PEMFC catalysts.

4.2 Experimental

4.2.1 Sample Preparation

NH3-CB was prepared by thermal treatment of high surface area carbon black (AkzoNobel) under Ar flow with NH_3 at 950°C for 15 minutes. O3-CB was prepared via pulsed ozone treatment using an atomic layer deposition system (Gemstar, Arradiance). 200 cycles of ozone were applied at 250°C with each cycle consisting of a 200 ms pulse of ozone with 10 s exposure, then a 1 s pulse of N_2 and 10 s exposure to purge the system before the next cycle.

Pt on CB catalysts with 40 wt.% nominal loading were prepared by a microwave-assisted polyol method similar to those previously described [29], [30]. Briefly, 175 mL of EG (ReagentPlus ≥99%, Sigma), 50 mg of O3-CB (or NH3-CB) and 88.9 mg of $H_2PtCl_6{\cdot}6(H_2O)$ (reagent grade, Sigma Aldrich) were sonicated for 2 hours in a room temperature sonic bath. NaOH in EG solution was used to bring the pH of the mixture above 10. The solution was then heated in a consumer microwave (1100 W, Panasonic) for two minutes. After cooling, HCl (37%) was added drop wise to the solution, while stirring, to adjust the pH to <2. The addition of acid has been shown to improve the deposition of

Pt on the substrate surface for this synthesis [31]. The solution was then filtered, washed with ultra-pure water, and dried overnight in a vacuum oven at 60°C. The Pt/C catalyst used for comparison was 46 wt. % Pt on unmodified CB from TKK (TEC10E50E).

4.2.2 Electrochemical Measurements

Catalyst ink consisted of 3 mg of the prepared catalyst plus 3 mL of 80:20 (wt. /wt.) solution of ultrapure water and isopropanol plus 30 µL of 5 wt. % Nafion solution (Ion Power). This was sonicated for 60 minutes in an ultrasonic bath at room temperature. Two 10 µL aliquots of the catalyst ink were dropped onto a polished glassy carbon (GC) electrode (Pine, 5 mm diameter) and dried under a heat lamp. After the second aliquot had dried, a small amount of ultrapure water was dropped onto the electrode to improve wetting in the electrochemical cell. The prepared GC electrode with catalyst served as the working electrode. A Pt wire and $Hg/HgSO_4$ electrode were used as the counter and reference electrodes, respectively. A correction of -0.658 V vs. RHE was used for the $Hg/HgSO_4$ electrode and all potentials henceforth are given with respect to RHE. Measurements were done using a standard potentiostat (AutoLab). All measurements were done at room temperature using 0.5 M H_2SO_4 electrolyte prepared with Milli-pure water (18.2 MΩ/cm^2) and high purity H_2SO_4 (99.999%, Aldrich). Initially, the working electrode was cycled a minimum 40 times from 0.05-1.0 V at 100 mV/s to condition and activate the fresh catalyst. CVs were measured under N_2 (99.999%) saturation, cycled from 0.05-1.0 V at 20 mV/s. Electrochemical surface area (ECSA) values were calculated by integrating the peak of the CV curve in the hydrogen under-potential deposition (H_{UPD}) region (0.05~0.3 V), using the current of the double layer (taken at 0.4 V) as a baseline and a charge of 210 µC/cm^2, representing the charge of a monolayer of hydrogen adsorbed on the Pt surface. ORR curves were taken under O_2 saturation which was achieved by bubbling O_2 (99.99%) for a minimum of 20 minutes. The electrode was rotated at 1600 RPM and cycled from 0.05-1.0 V at 20 mV/s. The reported polarization curves use the anodic scan, with baseline correction from the N_2 saturated CV. Mass and specific activities are reported at 0.9 V, using the kinetic current, i_k, which is determined from the ORR curves using the equation:

$$i_k = \frac{(i \times i_{\lim})}{(i_{lim} - i)} \quad \textbf{(4-1)}$$

where i_{lim} and i the limiting current and working electrode current, respectively. The limiting current was taken as the current at 0.4 V. ASTs were done by scanning from 0.6-1.0 V at 50 mV/s for 4000 cycles in N_2 saturated electrolyte. CVs were recorded at various points in the 4000 cycles to monitor the loss of ECSA over the duration of the AST. ORR activity was measured before and after the AST.

4.2.3 Physical Characterization

Gas sorption was carried out using a Micrometrics TriStar II Series porosity analyzer using high purity N_2 gas as the adsorbate. Before measurement, samples were degassed at 90° for one hour then 300°C for three hours under an Ar purge. Specific surface area was calculated using the multi-point Brunnaeur, Emmet and Teller (BET) method. X-ray diffraction (XRD) spectroscopy was performed using a Bruker D8 Advance using a Cu-Kα source (40 kV, 40 mA). Scanning electron microscopy was done with a Hitachi S-4800 field-emission SEM at 5-10 kV in secondary electron mode. Transmission electron microscopy (TEM) and high-resolution TEM were done using a JEOL 2010F at the Canadian Center for Electron Microscopy. To prepare samples for TEM after AST, the RDE tip with thin catalyst layer was sonicated in high purity methanol for several seconds to disperse the catalyst. A drop of this solution was then deposited onto a holey carbon TEM grid and allowed to dry in air.

4.3 Results

4.3.1 Modified Carbon Characterization

Untreated carbon black sample (CB), was compared with carbon after ammonia treatment (NH3-CB) and ozone treatment (O3-CB). A physical characterization of the

modified CB supports before deposition of Pt was done to identify differences in the properties of the carbons which could be correlated to differences in their Pt-support characteristics or catalytic performance. Gas-sorption at 77 K using N_2 was used to study the surface area of the three CB samples and the isotherms for each are shown in Figure 4-1. The specific surface area of these catalyst are 780, 759, and 904 m^2/g for CB, O3-CB, and NH3-CB. These results indicate a surface area increase of 16% with ammonia treatment and decrease of 3% with ozone treatment. A small decrease in surface area after ozone treatment of carbon black has been observed previously [16], [32]. The increased surface area with ammonia treatment is expected and has been shown in other nanostructure carbon materials [33]. Ammonia treatment at high temperature will etch some carbon [34] and reduce oxygen containing surface groups [27], [35].

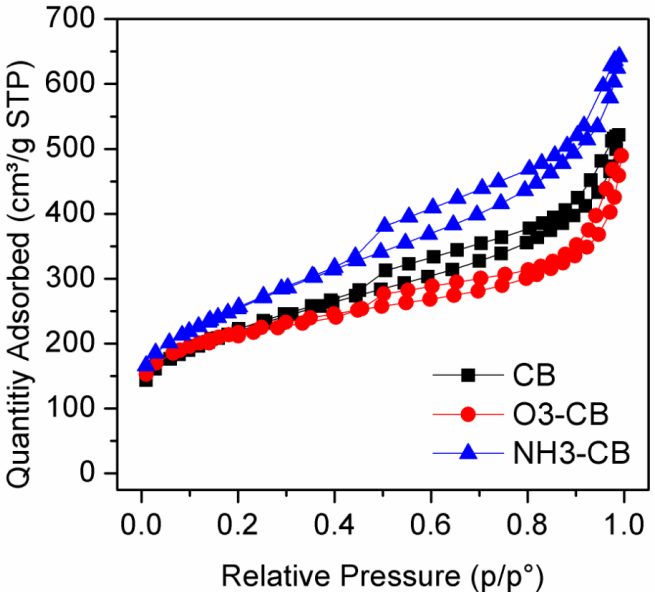

Figure 4-1. Gas sorption isotherms taken at 77 K for CB, O3-CB, and NH3-CB.

X-ray photoelectron spectroscopy (XPS) surveys were done to study the surface groups on each CB sample and the concentrations of oxygen and nitrogen. Each sample showed similar surveys with only carbon, oxygen, and nitrogen detected. The high resolution C 1s peaks for each sample are shown in Figure 4-2(a). Each shows a dominant C=C bond character with a peak at 283 eV, as is expected for carbon black. An important difference between the unmodified and modified CB samples is seen in the shoulder at the higher binding energy (left) side of the C 1s peak, from 285~287 eV. In NH3-CB, and to a

greater extent in O3-CB, this shoulder appears as a result of higher energy functional groups at the sample surface. Fitting analysis suggests a mixed signal from several oxygen containing structures which could include a mixture of alcohols, ethers, and double bonded oxygen species. Oxygen containing groups make up 19.1 % of the C 1s peak area for O3-CB, compared to 15.7 and 16.1 % for NH3-CB and CB, respectively, pointing to increased oxygen functionality in O3-CB as a result of the ALD ozone treatment. The total oxygen concentrations in CB, O3-CB, and NH3-CB were 1.4, 2.4, and 1.6 at. %, respectively. The O 1s peak of O3-CB is shown in Figure 4-2(b). The peak is well defined and confirms the presence of highly aromatic system of bound oxygen species consisting or ethers, quinones, and carboxylic groups. Nitrogen was found in concentrations of 0.1, 0.2, and 0.7 at. % in CB, O3-CB, and NH3-CB. The N 1s peak was hardly present in CB or O3-CB, compared to NH3-CB, which is shown in Figure 4-2(c) below. The peak is made up of two smaller peaks at 400.2 and 398.3 eV, corresponding to pyrrolic and pyridinic nitrogen groups, respectively [36]. There appears to be a higher density of the pyridinic nitrogen, part of a six sided ring, compared to the five sided pyrrolic nitrogen. These results confirm the modification of O3-CB and NH3-CB surfaces with additional oxygen and nitrogen, respectively.

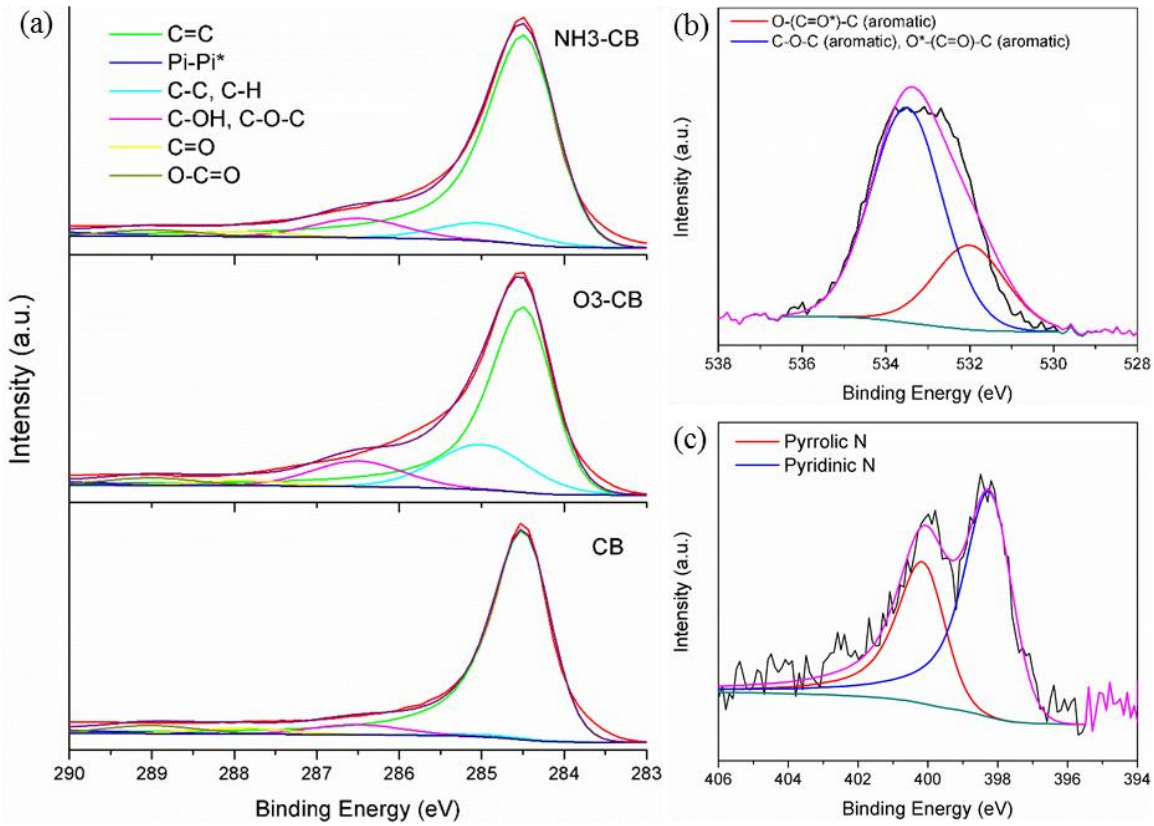

Figure 4-2. (a) High resolution C 1s peak for CB, O3-CB, NH3-CB. High resolution O 1s peak in O3-CB (b) and N 1s peak in NH3-CB (c).

4.3.2 Characterization of Pt Catalysts

SEM and TEM were used to examine the catalyst morphology and the distribution and size of Pt particles. Images from these techniques are shown in Figure 4-3. The SEM images show an even distribution of particles and relatively uniform particle size for each catalyst. Though an accurate particle size analysis is not possible using SEM images, it is apparent that the particles are <5 nm in each sample. The SEM results confirm that the reduction of Pt-salt and deposition on the carbon supports was highly successful. Others have pointed out that using EG as the solvent and reducing agent can be advantageous because of its high viscosity compared to aqueous or alcoholic solutions, and its relative weakness as a reducing agent [37]. The high viscosity retards the agglomeration of small particles and the slower reduction allows for more nucleation of the salt, resulting in very small and uniform Pt particles.

High-resolution TEM images (Figure 4-3) allow for a direct observation of particles and suggest a relatively narrow particle size distribution on each catalyst. Particle size analysis was done via manual image analysis measurements of more than 250 particles on each of the catalysts. From this method, the average particle diameter was 2.40 ±0.64 for Pt/CB, 2.13 ±0.65 for Pt/O3-CB, and 1.98 ±0.47 nm Pt/NH3-CB (± being one standard deviation). The smaller particle size of Pt/O3-CB is likely related to the acidic surface oxide groups which promote excellent dispersion of the chloroplatinic acid precursor during synthesis [18], [32], [38]. On NH3-CB, the increase in surface area by >100 m^2/g compared to CB provides myriad sites for Pt deposition to occur, resulting in the very small particle size observed.

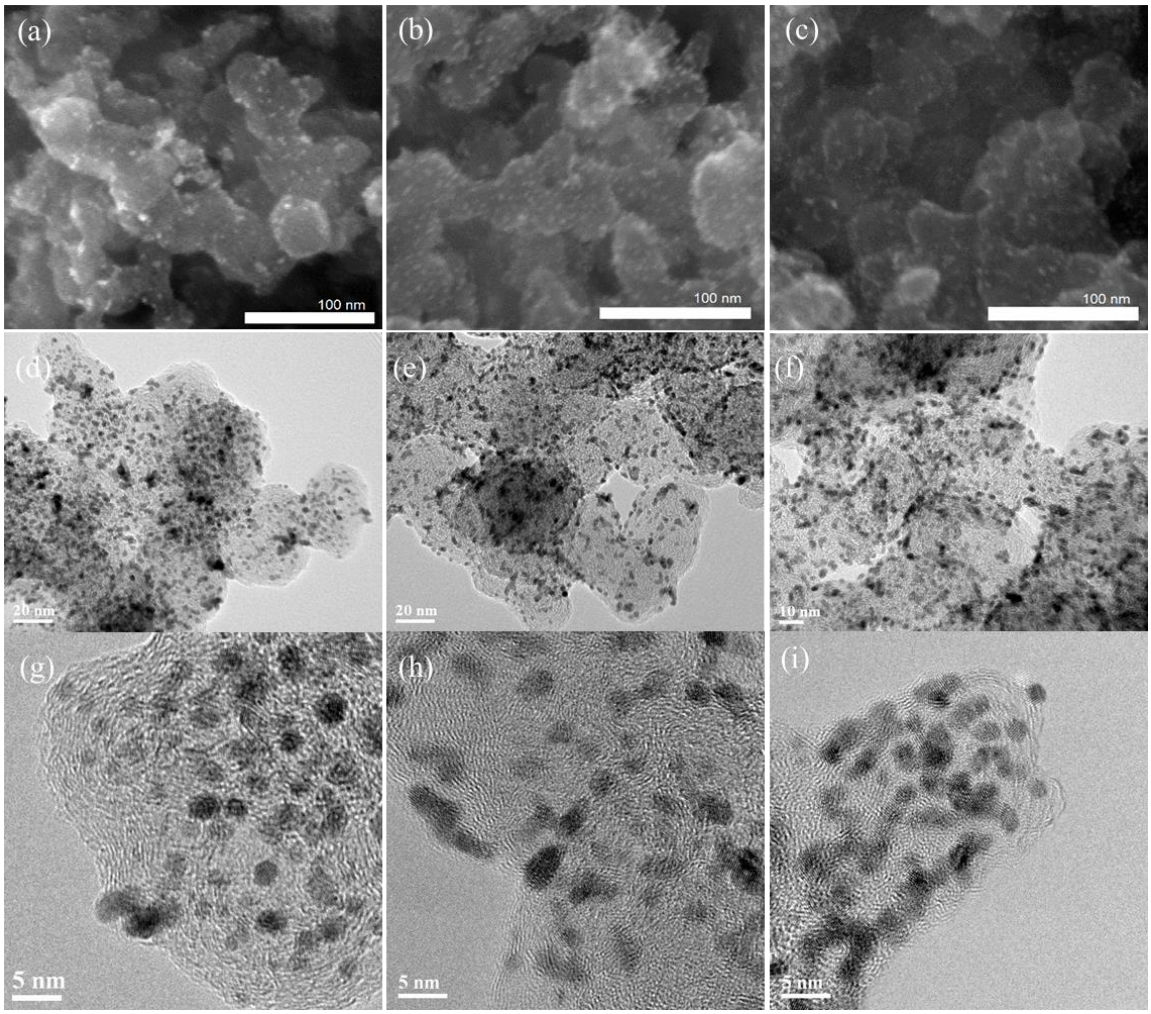

Figure 4-3. SEM, TEM, and high-resolution TEM images of Pt/CB (a, d, g) Pt/O3-CB (b, e, h) and Pt/NH3-CB (c, f, i) showing good distribution of particles and relatively homogeneous particle size.

XRD analysis confirmed the presence of Pt on each catalyst and can be used to determine the average particle size. The spectra for each catalyst in shown in Figure 4-4(a). There are clear peaks at 2θ values of 39.8, 46, and 67.5 degrees, corresponding to the (111), (200) and (220) of Pt, respectively, and at 24.8° corresponding to the carbon (002) plane from the support. The Pt peaks confirm the metallic nature of the catalyst particles and the broad Pt(111) peak in the XRD spectra of these catalysts is indicative of very small particles. Using the Scherrer equation [39], the Pt particle size, *d*, was calculated using the peak width of the (220) crystal peak, the Cu-Kα wavelength of 0.154 nm and a shape factor, *k*, of 1.0. The particle sizes are 2.86, 1.96, and 1.90 nm for Pt/C, Pt/O3-CB, and Pt/NH3-

CB (Table 4-1). The carbon (002) plane is visible at 24.8° in each spectra, as expected from the CB support. We can estimate the carbon crystallite lateral dimension, L_c, using the Scherrer equation, as CB is known to have graphitic micro-phases [40]. The carbon (002) crystallite sizes are 2.65, 1.81, and 2.00 nm for CB, O3-CB, and NH3-CB. This indicates a reduction in the size of the graphitic micro-phases in NH3-CB and O3-CB, compared with the unmodified CB. Reduction in the size of these small crystal phases also corresponds to an increased density of micro-phase boundaries which could act as higher energy sites, promoting bonding of Pt particles. This explanation would fit with the observation of decreased particle size in the modified samples. Inductively coupled plasma mass spectrometry (ICP-MS) analysis provided accurate Pt concentrations for the catalysts used in this study; the values of which are given in Table 4-1. These values are similar enough to exclude any effects from differences in Pt loading on the activity or stability of the catalyst. Furthermore, having similar loadings allows for a more straightforward comparison of Pt particle size.

Table 4-1. Properties of supported Pt catalysts.

Sample	SA_{BET} (m^2/g)*	C(002) crystallite size, L_C (nm)	Pt wt.%	d_{XRD} (nm)	d_{TEM} (nm)
Pt/CB	780	2.63	46.0	2.86	2.40
Pt/O3-CB	759	1.45	36.6	1.96	2.13
Pt/NH3-CB	904	1.42	38.7	1.90	1.98

* *Gas sorption analysis on carbons only*

In order to further understand the Pt-support interactions in the treated CB samples, high energy X-ray absorption near-edge structure (XANES) analysis was performed on the Pt L_3 edge of the catalysts. The spectra are shown in Figure 4-4(b). In each sample, there is a strong absorption edge at 11565 eV (referred to as the whiteline); the integrated intensity of which is related to the *d*-orbital vacancies in Pt [41]. A qualitative analysis of the whiteline shows higher intensity for Pt/O3-CB than for Pt/CB or Pt/NH3-CB. This is noticeable in the inset where the normalized spectra are overlaid with no offset. This points to an increased density of unoccupied 5d orbitals in Pt which suggests increased Pt-substrate interactions compared to the other two samples [42], [43]. Catalyst-support

interactions can play an important role in promoting good ORR activity and stabilizing catalyst particles.

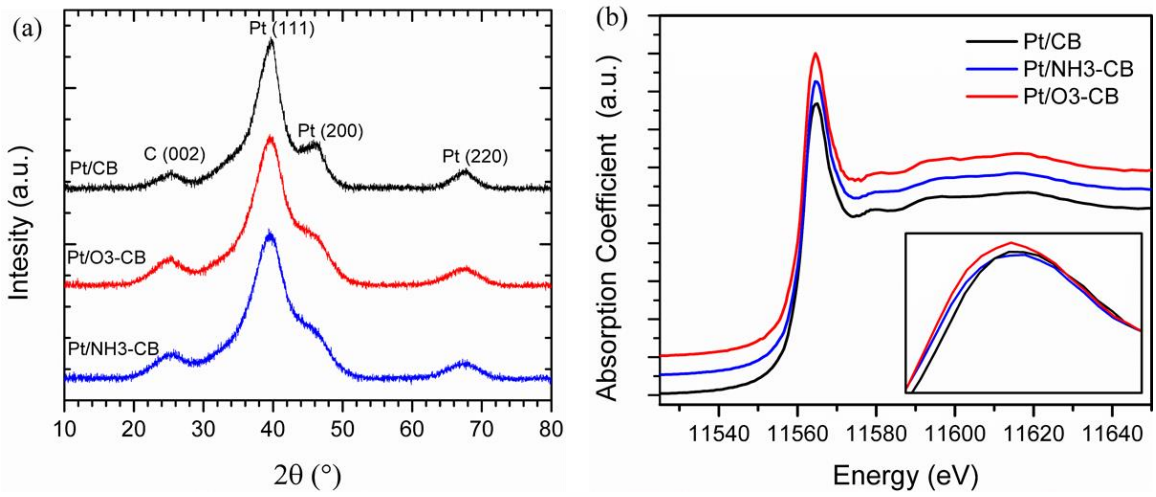

Figure 4-4. XRD (a) and XANES (b) and spectra of Pt/CB (black), Pt/O3-CB (red), and Pt/NH3-CB (blue). The inset is (b) is a highlight of the XANES absorption edge at 11565 eV.

4.3.3 Electrochemical Characterization

CV was used to determine the activity and durability of the three catalysts in an electrochemical half-cell setup. The overlaid CV curves from 0.05-1.0 V for each catalyst, taken under N_2 saturation, are shown in Figure 4-5(a). The ECSA of Pt/C, Pt/O3-CB, and Pt/NH3-CB were 68.2, 72.2, and 71.4 respectively. ECSA values are similar for each catalyst, though Pt/CB has the lowest of the three catalysts. There is little change in shape of the H_{UPD} regions as expected from the similar particle size and metallic nature of each Pt in each sample indicating minimal effects of either modified CB support on the adsorption of hydrogen. The slightly smaller catalysts particles in the two modified carbons can explain the small increased in ECSA for both, compared to Pt/CB. The current density of the ORR peak is slightly increased for Pt/NH3-CB and even more for Pt/O3-CB, with respect to Pt/CB (Figure 4-5(a)). ORR polarization curves recorded at 20 mV/s with rotation of 1600 rpm is shown in Figure 4-5(b). The shape of each curve is typical of supported Pt catalysts. A limiting current around 5 mA/cm^2 with 0.5 M H_2SO_4 electrolyte is consistent with literature [44]. In the kinetic and mixed kinetic/diffusion region above

~0.8 V, there is an obvious increase in current density for both Pt/NH3-CB and Pt/O3-CB. Mass activity (MA) for Pt/O3-CB was 38.8 mA/mg_{Pt} compared to 36.5 and 33.0 mA/mg_{Pt} for Pt/NH3-CB and Pt/CB, respectively. Both modified CB supports show improvement compared to untreated CB, with ALD ozone treatment and high temperature ammonia treatment resulting in 18% and 11% increase in initial MA, respectively. As the XANES analysis data suggested, Pt supported on the O3-CB showed a higher degree of unoccupied density of states, which may account for the increased in ORR activity [42]. Furthermore, the increased limiting current seen in the Pt/O3-CB may be attributed to increased hydrophilicity of the oxygenated surface which allows electrolyte, and hence protons, to reach the catalyst surface. NH3-CB supported Pt likely shows the slight improvement in ORR activity due to the high support surface area and decreased Pt particle size compared to CB, with some improvement potentially the result of N-dopants at the surface.

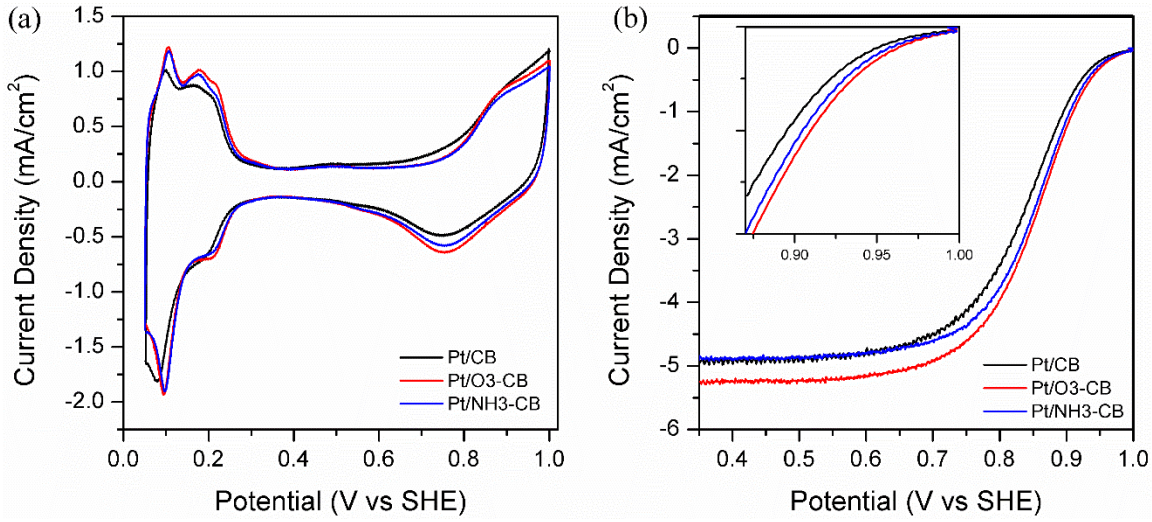

Figure 4-5. CV curves normalized to Pt loading (a) and ORR polarization curves at rotation rate of 1600 RPM for Pt/CB, Pt/O3-CB, Pt/NH3-CB. Recorded in N_2 (a) and O_2 (b) saturated 0.5 M H_2SO_4 with a scan rate of 20 mV/s.

To study the durability of the catalyst with prolonged use, an AST was done consisting of 4000 potential cycles from 0.6-1.0 V in N_2 saturated H_2SO_4. This potential

window is commonly used for RDE ASTs and is meant simulate the operating range of a PEM fuel cell. The AST primarily targets catalyst degradation via Pt dissolution. CVs recorded throughout the AST were used to determine the ECSA, and the results are shown in Figure 4-6(a). The Pt/CB, Pt/O3-CB, and Pt/NH3-CB retain 73, 84, and 70% of their original ECSAs, respectively. Complementing the AST data, HR-TEM images were acquired each catalyst after the AST to investigate changes in the Pt particle size after cycling. The particle sizes for Pt/CB, Pt/O3-CB, and Pt/NH3-CB increased to 3.36, 2.39, and 2.84 nm from their original sizes corresponding to a 40, 12, and 43% increase. Post-AST images for Pt/CB and Pt/O3-CB are shown in Figure 4-6(c and d), including inset histograms of the particle size distribution before and after AST. The order of relative particle size increase in the three catalysts corresponds to the order of ECSA loss (Pt/O3-CB < Pt/CB < Pt/NH3-CB). These results indicate a good ECSA retention during AST and stable, small particles in Pt/O3-CB compared to the other two samples. The reduced surface area of the carbon may have some part to play in the durability of the Pt/O3-CB but this effect should be minimal considering the relatively small difference from untreated CB. Rather, the improved particle stability may be ascribed to the increased density of oxygen-containing surface functional groups, which others have pointed to as having stabilizing effects on dispersed Pt particles due to increased surface homogeneity and because their presence creates an energy barrier to particle migration [18], [19]. NH3-CB appears to have poor ECSA retention after AST, losing slightly more of its original than the untreated CB. The reason for this may be the higher surface area of the ammonia treated carbon and the initial Pt particle size which was smallest on Pt/NH3-CB. The very small original size has high surface energy and thus increased potential for particle growth. It appears that high surface area of the NH3-CB and the relatively low concentration of N-functionality did little to prevent that growth. Pt/CB experiences considerable growth despite having the largest original particle size, suggesting poor stability of the Pt particles on the unmodified CB surface.

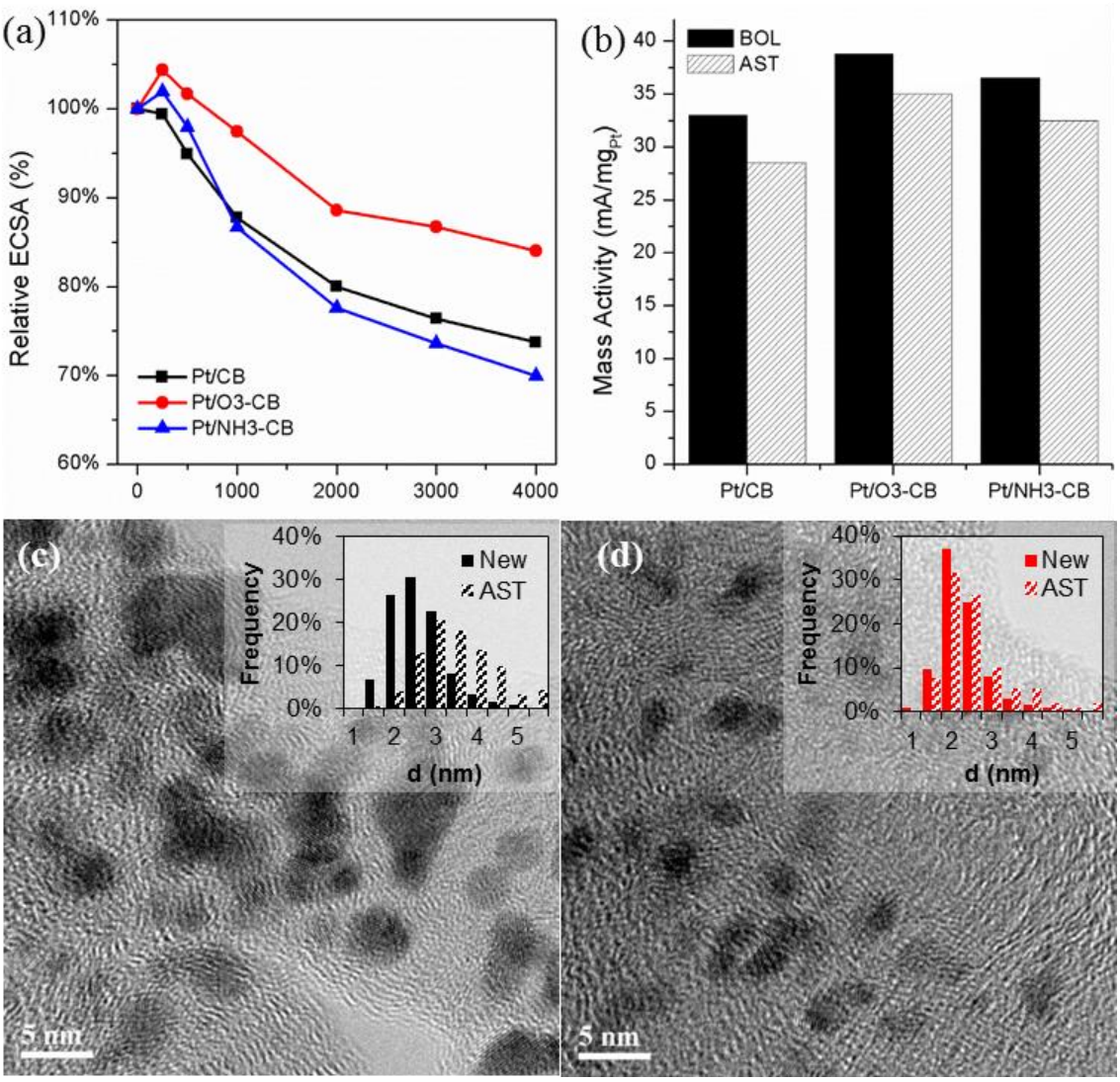

Figure 4-6. Relative ECSA values during AST cycling (a) and MA before and after AST (b) for Pt/CB, Pt/O3-CB, and Pt/NH3-CB. TEM images of Pt/CB (c) and Pt/O3-CB (d) after AST. The insets in (c) and (d) show histograms of the particle size distribution before and after AST. Cycling was done from 0.6-1.0 V in N_2 saturated 0.5 M H_2SO_4 at room temperature.

ORR polarization curves were taken at the beginning of life (BOL) and end of the AST to determine how well each catalyst retained its original MA. The MA for each catalyst at BOL and AST are shown in Figure 4-6(b). Pt/O3-CB and Pt/NH3-CB have losses in MA of 7% and 11% after 4000 cycles. Meanwhile, Pt/CB loses 15% of initial MA after cycling. Despite losing slightly more of its original ECSA, Pt/NH3-CB retains a larger fraction of its original MA after AST compared to Pt/CB. Although the improvement in

MA is small, the results may be due to an increase in the surface-area specific activity in Pt/NH3-CB because of more buried Pt atoms, compared to surface atoms. The average particle size after AST for Pt/NH3-CB is 2.84 nm, compared to 3.36 nm in Pt/CB, suggesting that the MA should still be better in NH3-CB. The improved durability in the Pt/O3-CB is likely a result of the aforementioned stability of the small Pt particles on the support surface. Further, the electronic interactions between the Pt particles and support, as evidenced by XANES, lead to increased electron vacancy in the 5d orbitals. It's possible that the changed electron state of Pt supported by O3-CB has some effect on dissolution potential of the Pt [45], retarding Pt dissolution in this AST potential range.

Overall, it appears that Pt/O3-CB shows the most promise due to its combination of good mass activity and stability in the operating potential. While ammonia treatment shows good dispersion and very small particles, the stability of those particles is lacking, showing little improvement over untreated CB. Future work could be done to optimize the ozone treatment process for CB and incorporating these catalysts in MEAs for single cell testing at a larger scale.

4.4 Conclusions

A one-step treatment of CB with either ozone or ammonia was used to introduce surface functionality on the support material for improved properties for catalyst activity and durability. Gas sorption results showed a considerable increase in specific surface area after NH3 treatment, and a slight decrease after ozone treatment, compared to untreated CB. After deposition of Pt via reduction in EG, particle size analysis via TEM and XRD showed smaller Pt particles on Pt/O3-CB and Pt/NH3-CB, compared to Pt/CB. This is a result of increased high-energy sites and the acidic surface on treated CBs which promote good Pt anchoring during deposition. XANES analysis showed an increase in Pt L_3 edge absorption intensity for the Pt/O3-CB catalyst, pointing to higher density of unoccupied d-orbitals in the Pt and a higher degree of Pt-support interaction, compared to CB or NH3-CB. The ECSAs of the three catalysts do not vary considerably but there is an increase in the MA. Pt/O3-CB and Pt/NH3-CB have MA values of 38.8 and 36.5 mA/mg_{Pt},

respectively, which is 18% and 11% higher than Pt/CB (33.0 mA/mg_{Pt}). After AST, the ozone and ammonia treated CB catalysts retained 93% and 89% of initial MA, compared to Pt/C which retained 85% of initial MA. The increased durability of the Pt/O3-CB is attributed to the increased density of active sites, highlighted by XPS analysis, which hinder particle growth during cycling. This work demonstrates a simple, one-step method for modifying CB which results in stable small Pt particles, increasing ORR activity and catalyst durability in the operating range. These results are meaningful as they point to a low cost opportunity for increasing PEM fuel cell performance.

4.5 References

[1] D. L. Greene and G. Duleep, “Status and Prospects of the Global Automotive Fuel Cell Industry and Plans for Deployment of Fuel Cell Vehicles and Hydrogen Refueling Infrastructure,” 2013.

[2] P. J. Ferreira, G. J. la O’, Y. Shao-Horn, D. Morgan, R. Makharia, S. Kocha, and H. a. Gasteiger, “Instability of Pt/C Electrocatalysts in Proton Exchange Membrane Fuel Cells,” *J. Electrochem. Soc.*, vol. 152, no. 11, p. A2256, 2005.

[3] M. K. Debe, “Electrocatalyst approaches and challenges for automotive fuel cells.,” *Nature*, vol. 486, no. 7401, pp. 43–51, Jun. 2012.

[4] S. Ye, M. Hall, and P. He, “PEM Fuel Cell Catalysts: The Importance of Catalyst Support,” in *ECS Transactions*, 2008, vol. 16, no. 2, pp. 2101–2113.

[5] S. Sharma and B. G. Pollet, “Support materials for PEMFC and DMFC electrocatalysts—A review,” *J. Power Sources*, vol. 208, pp. 96–119, Jun. 2012.

[6] M. S. Saha, V. Neburchilov, D. Ghosh, and J. Zhang, “Nanomaterials-supported Pt catalysts for proton exchange membrane fuel cells,” *Wiley Interdiscip. Rev. Energy Environ.*, vol. 2, no. 1, pp. 31–51, Jan. 2013.

[7] E. Antolini, “Graphene as a new carbon support for low-temperature fuel cell catalysts,” *Appl. Catal. B Environ.*, vol. 123–124, pp. 52–68, Jul. 2012.

[8] H. Lv and S. Mu, “Nano-ceramic support materials for low temperature fuel cell catalysts.,” *Nanoscale*, vol. 6, no. 10, pp. 5063–74, May 2014.

[9] R. Borup, J. Meyers, B. Pivovar, Y. S. Kim, R. Mukundan, N. Garland, D. Myers, M. Wilson, F. Garzon, D. Wood, P. Zelenay, K. More, K. Stroh, T. Zawodzinski, X. J. Boncella, J. E. Mcgrath, O. M. Inaba, K. Miyatake, M. Hori, K. Ota, Z. Ogumi, S. Miyata, A. Nishikata, Z. Siroma, Y. Uchimoto, K. Yasuda, K. Kimijima, and N. Iwashita, “Scientific Aspects of Polymer Electrolyte Fuel Cell Durability and Degradation,” pp. 3904–3951, 2007.

[10] M. L. Perry, T. Patterson, and C. Reiser, “Systems Strategies to Mitigate Carbon Corrosion in Fuel Cells,” in *ECS Transactions*, 2006, vol. 3, no. 1, pp. 783–795.

[11] Y. Yu, H. Li, H. Wang, X.-Z. Yuan, G. Wang, and M. Pan, “A review on performance degradation of proton exchange membrane fuel cells during startup and shutdown processes: Causes, consequences, and mitigation strategies,” *J. Power Sources*, vol. 205, pp. 10–23, May 2012.

[12] J. Zhang, Ed., *PEM Fuel Cell Electrocatalysts and Catalyst Layers*. London: Springer London, 2008.

[13] J. Zhu, M. Xiao, X. Zhao, C. Liu, J. Ge, and W. Xing, "Strongly coupled Pt nanotubes/N-doped graphene as highly active and durable electrocatalysts for oxygen reduction reaction," *Nano Energy*, pp. 1–9, 2015.

[14] M. N. Groves, A. S. W. Chan, C. Malardier-Jugroot, and M. Jugroot, "Improving platinum catalyst binding energy to graphene through nitrogen doping," *Chem. Phys. Lett.*, vol. 481, no. 4–6, pp. 214–219, Oct. 2009.

[15] N. Cheng, M. Norouzi Banis, J. Liu, A. Riese, S. Mu, R. Li, T.-K. Sham, and X. Sun, "Atomic scale enhancement of metal–support interactions between Pt and ZrC for highly stable electrocatalysts," *Energy Environ. Sci.*, vol. 00, pp. 1–6, 2015.

[16] I. Sutherland, E. Sheng, R. H. Bradley, and P. K. Freakley, "Effects of ozone oxidation on carbon black surfaces," *J. Mater. Sci.*, vol. 31, no. 21, pp. 5651–5655, 1996.

[17] G. C. Torres, E. L. Jablonski, G. T. Baronetti, a. a. Castro, S. R. de Miguel, O. a. Scelza, M. D. Blanco, M. a. Pen˜a Jiménez, and J. L. G. Fierro, "Effect of the carbon pre-treatment on the properties and performance for nitrobenzene hydrogenation of Pt/C catalysts," *Appl. Catal. A Gen.*, vol. 161, no. 1–2, pp. 213–226, 1997.

[18] C. Prado-Burguete, a. Linares-Solano, F. Rodriguez-Reinoso, and C. Salinas-Martinez de Leca, "The Effect of Oxygen Surface Groups of the Support Dispersion in Pt / Carbon Catalysts on Platinum," *J. Catal.*, vol. 115, pp. 98–106, 1989.

[19] P. Ehrburger, O. P. Mahajan, and P. L. Walker, "Carbon as a support for catalysis—effect of surface heterogeneity of carbon on dispersion of platinum," *Carbon N. Y.*, vol. 14, no. 5, p. 295, Jan. 1976.

[20] A. Lushington, J. Liu, Y. Tang, R. Li, and X. Sun, "Surface modification of nitrogen-doped carbon nanotubes by ozone via atomic layer deposition," *J. Vac. Sci. Technol. A Vacuum, Surfaces, Film.*, vol. 32, no. 1, p. 01A124, 2014.

[21] H. Wang, T. Maiyalagan, and X. Wang, "Review on Recent Progress in Nitrogen-Doped Graphene: Synthesis, Characterization, and Its Potential Applications," *ACS Catal.*, vol. 2, no. 5, pp. 781–794, May 2012.

[22] M. S. Saha, R. Li, X. Sun, and S. Ye, "3-D composite electrodes for high performance PEM fuel cells composed of Pt supported on nitrogen-doped carbon nanotubes grown on carbon paper," *Electrochem. commun.*, vol. 11, no. 2, pp. 438–441, 2009.

[23] Y. Cheng, C. Xu, P. K. Shen, and S. P. Jiang, "Effect of nitrogen-containing functionalization on the electrocatalystic activity of PtRu nanoparticles supported on carbon nanotubes for direct methanol fuel cells," *Appl. Catal. B Environ.*, Apr. 2014.

[24] C. Jeyabharathi, P. Venkateshkumar, M. S. Rao, J. Mathiyarasu, and K. L. N. Phani, "Nitrogen-doped carbon black as methanol tolerant electrocatalyst for oxygen reduction reaction in direct methanol fuel cells," *Electrochim. Acta*, vol. 74, pp. 171–175, Jul. 2012.

[25] N. P. Subramanian, X. Li, V. Nallathambi, S. P. Kumaraguru, H. Colon-Mercado, G. Wu, J. W. Lee, and B. N. Popov, "Nitrogen-modified carbon-based catalysts for oxygen reduction reaction in polymer electrolyte membrane fuel cells," *J. Power Sources*, vol. 188, no. 1, pp. 38–44, 2009.

[26] S. S. Rich, J. J. Burk, C. S. Kong, C. D. Cooper, D. E. Morse, and S. K. Buratto, "Nitrogen functionalized carbon black: A support for Pt nanoparticle catalysts with narrow size dispersion and high surface area," *Carbon N. Y.*, pp. 2–10, Sep. 2014.

[27] B. Stöhr, H. P. Boehm, and R. Schlögl, "Enhancement of the catalytic activity of activated carbons in oxidation reactions by thermal treatment with ammonia or hydrogen cyanide and observation of a superoxide species as a possible intermediate," *Carbon N. Y.*, vol. 29, no. 6, pp. 707–720, 1991.

[28] M. N. Groves, a. S. W. Chan, C. Malardier-Jugroot, and M. Jugroot, "Improving platinum catalyst binding energy to graphene through nitrogen doping," *Chem. Phys. Lett.*, vol. 481, no. 4–6, pp. 214–219, Oct. 2009.

[29] Z. Liu, J. Y. Lee, W. Chen, M. Han, and L. M. Gan, "Physical and Electrochemical Characterizations of Microwave-Assisted Polyol Preparation of Carbon-Supported PtRu Nanoparticles," *Langmuir*, vol. 20, no. 1, pp. 181–187, 2004.

[30] S. Harish, S. Baranton, C. Coutanceau, and J. Joseph, "Microwave assisted polyol method for the preparation of Pt/C, Ru/C and PtRu/C nanoparticles and its application in electrooxidation of methanol," *J. Power Sources*, vol. 214, pp. 33–39, 2012.

[31] A. B. A. A. Nassr, I. Sinev, M. M. Pohl, W. Grünert, and M. Bron, "Rapid microwave-assisted polyol reduction for the preparation of highly active PtNi/CNT electrocatalysts for methanol oxidation," *ACS Catal.*, vol. 4, no. 8, pp. 2449–2462, 2014.

[32] Z.-B. Wang, G.-P. Yin, and P.-F. Shi, "Effects of ozone treatment of carbon support on Pt–Ru/C catalysts performance for direct methanol fuel cell," *Carbon N. Y.*, vol. 44, no. 1, pp. 133–140, 2006.

[33] D. Geng, S. Yang, Y. Zhang, J. Yang, J. Liu, R. Li, T.-K. Sham, X. Sun, S. Ye, and S. Knights, "Nitrogen doping effects on the structure of graphene," *Appl. Surf. Sci.*, vol. 257, no. 21, pp. 9193–9198, Aug. 2011.

[34] C. L. Mangun, K. R. Benak, J. Economy, and K. L. Foster, "Surface chemistry, pore sizes and adsorption properties of activated carbon fibers and precursors treated with ammonia," *Carbon N. Y.*, vol. 39, no. 12, pp. 1809–1820, 2001.

[35] X. Li, H. Wang, J. T. Robinson, H. Sanchez, G. Diankov, and H. Dai, "Simultaneous nitrogen doping and reduction of graphene oxide.," *J. Am. Chem. Soc.*, vol. 131, no. 43, pp. 15939–44, Nov. 2009.

[36] S. R. Kelemen, M. Afeworki, M. L. Gorbaty, P. J. Kwiatek, M. S. Solum, J. Z. Hu, and R. J. Pugmire, "XPS and 15N NMR study of nitrogen forms in carbonaceous solids," *Energy and Fuels*, vol. 16, no. 6, pp. 1507–1515, 2002.

[37] A. Guha, W. Lu, T. a. Zawodzinski, and D. a. Schiraldi, "Surface-modified carbons as platinum catalyst support for PEM fuel cells," *Carbon N. Y.*, vol. 45, no. 7, pp. 1506–1517, 2007.

[38] A. Guerrero-Ruiz, P. Badenes, and I. Rodríguez-Ramos, "Study of some factors affecting the Ru and Pt dispersions over high surface area graphite-supported catalysts," *Appl. Catal. A Gen.*, vol. 173, no. 2, pp. 313–321, 1998.

[39] A. L. Patterson, "The scherrer formula for X-ray particle size determination," *Phys. Rev.*, vol. 56, no. 10, pp. 978–982, 1939.

[40] C. R. Houska and B. E. Warren, "X-Ray Study of the Graphitization of Carbon Black," *J. Appl. Phys.*, vol. 25, no. 12, p. 1503, 1954.

[41] A. N. Mansour, J. W. Cook, and D. E. Sayers, "Quantitative technique for the determination of the number of unoccupied d-electron states in a platinum catalyst using the L2,3 x-ray absorption edge spectra," *J. Phys. Chem.*, vol. 88, no. 11, pp. 2330–2334, 1984.

[42] M. N. Banis, S. Sun, X. Meng, Y. Zhang, Z. Wang, R. Li, M. Cai, T. Sham, and X. Sun, "TiSi 2 O x Coated N-Doped Carbon Nanotubes as Pt Catalyst Support for the Oxygen Reduction Reaction in PEMFCs," *J. Phys. Chem. C*, vol. 117, no. 30, pp. 15457–15467, Aug. 2013.

[43] F. Taufany, C. J. Pan, F. J. Lai, H. L. Chou, L. S. Sarma, J. Rick, J. M. Lin, J. F. Lee, M. T. Tang, and B. J. Hwang, "Relating the composition of PtxRu100-x/C nanoparticles to their structural aspects and electrocatalytic activities in the methanol oxidation reaction," *Chem. - A Eur. J.*, vol. 19, no. 3, pp. 905–915, 2013.

[44] U. A. Paulus, T. J. Schmidt, H. a. Gasteiger, and R. J. Behm, "Oxygen reduction on a high-surface area Pt/Vulcan carbon catalyst: a thin-film rotating ring-disk electrode study," *J. Electroanal. Chem.*, vol. 495, no. 2, pp. 134–145, Jan. 2001.

[45] X. X. Wang, Z. H. Tan, M. Zeng, and J. N. Wang, "Carbon nanocages: A new support material for Pt catalyst with remarkably high durability," *Sci. Rep.*, vol. 4, pp. 1–11, Mar. 2014.

5 Accelerated Stress Testing By Rotating Disk Electrode for Carbon Corrosion in Fuel Cell Catalyst Supports

Reproduced with permission from *J. Electrochem. Soc*. 2015 **162**:F783-F788; doi:10.1149/2.0911507jes

Durability is one of the key remaining challenges to widespread adoption of proton exchange membrane fuel cells (PEMFCs). The durability and continued high performance of a PEMFC using carbon supported catalysts is highly dependent on the stability of the carbon support. Presently, there are a multitude of accelerated stress test (AST) protocols using rotating disk electrode (RDE) voltammetry to study the corrosion of carbon catalyst support materials, though it remains unclear whether all of these tests provide meaningful reproduction of in-situ membrane electrode assembly (MEA) test results. We evaluate two carbon corrosion ASTs and compare results to MEA data for three well known carbon supported catalysts. Physical characterization of each carbon type by gas sorption, XRD, and Raman, is used to elucidate the observed trends in corrosion resistance and the effects of testing temperature, scan rate, and upper potential limit are examined. We find that AST results are highly dependent on temperature and total testing time, concluding that the first protocol is only valid at 60°C, while the second accurately represents MEA data. This study highlights the importance of different RDE AST parameters when developing ASTs that correlate with in-situ MEA testing.

5.1 Introduction

The widespread adoption of proton exchange membrane fuel cells (PEMFCs) for both motive and stationary applications is primarily dependent on reducing costs and improving the durability of the membrane electrode assembly (MEA). Prolonged use can be highly stressful on the MEA, making the loss of performance over the lifetime of the PEMFC one of the key limitations of the technology. Thus the durability of the cathodic catalyst, which facilitates the otherwise sluggish kinetics of the ORR, is of particular importance. State of the art PEMFC catalysts use Pt nanoparticles supported by a network of conducting carbon material. These catalyst particles and the supporting carbon must endure harsh operating conditions which include high electrode potentials, acidic environment, and temperatures up to 100°C. Pt catalyst degradation may proceed by several mechanisms including dissolution, Ostwald ripening, and physical agglomeration. The latter two mechanisms are exacerbated by carbon corrosion, which results in a reduction of the overall catalyst surface area [1]–[3]. In addition to this, severe carbon corrosion can lead to physical detachment of the Pt nanoparticle catalysts from the electrode structure, resulting in a total loss of catalytic activity towards the ORR from those detached particles [1], [4], [5].

Carbon corrosion, especially by electrochemical oxidation, has been extensively studied [4], [6]–[10]. Corrosion may occur by partial oxidation to intermediate surface groups or via multi-step oxidation to gaseous CO_2. Carbon surface groups may include quinones/hydroquinones, lactones, phenols, carbonyls, and carboxyls [11]–[13]. One proposed mechanisms of oxidation is [6], [14], [15]:

$$C \rightarrow C^+ + e^- \quad \textbf{(5-1)}$$

$$C^+ + H_2O \rightarrow CO + 2H^+ + e^- \quad \textbf{(5-2)}$$

$$2CO + H_2O \rightarrow CO + CO_{2(g)} + 2H^+ + 2e^- \quad \textbf{(5-3)}$$

While the oxidation of carbon is thermodynamically possible at > 0.207 V vs SHE, the kinetics of this reaction are extremely sluggish below 0.9 V. However, in the presence of Pt carbon oxidation may take place as low at 0.6 V [8]. These conditions, plus high humidity and an acidic environment, make degradation of the support material a point of particular concern. Indeed, carbon corrosion is observed both in real fuel cell systems, especially during start-up and shutdown, and in single cell testing of the membrane electrode assembly (MEA). To reach the DOE targeted fuel cell lifetime of 5,000 and 30,000 hours for automotive and stationary power applications, respectively [16], it is necessary to use accelerated stress tests (AST) which simulate a long performance lifetime on a timescale that is practical for research and engineering purposes.

Using single fuel cell test stations to test MEAs is a highly effective method for studying the performance of catalysts, catalyst supports, and membranes [15], MEA testing can be used to demonstrate the activity and durability of a fuel cell in an integrated way because it replicates the variety of operating conditions present in a real-world system. The disadvantage of this method, however, is that it can be difficult to decouple the effects of the myriad parameters and components involved in the system which makes interpreting AST data more complex.

Cyclic voltammetry by thin film rotating disk electrode (RDE) is a convenient alternative for testing fuel cell catalysts and catalyst support materials. Compared to in-situ MEA testing, RDE is advantageous in that catalyst activity can be easily de-convoluted from other components. It requires only small amounts of catalyst material, can often be done within a day, and needs far less of the complicated equipment and infrastructure needed for MEA testing. Though RDE is limited in terms of reproducing the complex environment of a real PEMFC environment, it is highly effective for screening and comparing catalysts and its minimal material requirements make it ideal for research purposes [17], Currently, there are a wide variety of RDE test protocols employed by different research groups around the world. Due to the nature of RDE testing, variations in test procedures can often lead to vastly different results from one lab to the next [18]. Thus, there is currently a trend to move toward standardization of protocols for catalyst activity and durability to allow more direct comparison of results [17]–[21].

Herein we study the effectiveness of RDE AST protocols for evaluating fuel cell catalyst support corrosion. We use three Pt catalysts supported on well-studied carbons: high surface area carbon (HSC), Vulcan carbon (VC), and a highly graphitized, low surface area carbon (LSC). Our test procedures are based on two test protocols suggested by the United States Department of Energy (DOE) for accelerated stress testing of catalyst supports by RDE [22]. By using these protocols we hoped to identify trends in carbon corrosion based on changes in electrochemical surface area (ECSA) and mass activity. Our aim is to determine whether these protocols can predict the trends observed during in-situ MEA testing [23]. It is expected that not all RDE ASTs can accurately represent the catalyst support durability observed in real fuel cell systems. In a broader sense, the goal of this study is to highlight the disparities between the data from ASTs done in-situ (MEA) versus those done ex-situ (RDE), and to suggest that a careful selection and evaluation of RDE AST parameters is needed.

5.2 Experimental

The carbon supports used in this work were: high surface area carbon (HSC), Vulcan XC72 (VC), and low surface area, graphitized carbon (LSC). HSC and LSC were supplied by TKK and VC was supplied by Cabot. Catalysts used were 47wt. % Pt/HSC, 50 wt. % Pt/VC, and 47 wt. % Pt/LSC. Catalyst inks were prepared by mixing 3 mg of catalyst, 3 mL of an 80:20 (wt./wt.) mixture of ultra-pure H_2O to isopropyl alcohol, and 30 µl of 5 wt. % Nafion in alcoholic solution. The mixture was then sonicated to ensure good dispersion and wetting of the catalyst. Two 10 µl aliquots of ink were deposited onto a polished gold electrode (Pine, AFE5T050AUHT, 5.0 mm dia.) and allowed to dry in air. The electrodes were kept stationary during drying. All electrochemical measurements were carried out in 0.09 M H_2SO_4 electrolyte using a Pt wire as the counter electrode and a reversible hydrogen electrode as the reference electrode. All potentials reported henceforth are vs. RHE. Each catalyst was activated by cycling from 0.05 to 1.0 at 100 mV/s in N_2 until no changes were observed in the cyclic voltammetry (CV) curve. CVs were recorded scanning from 0.05 – 1.0 V at 20 mV/s in N_2. ORR activity was measured at 0.9 V on the

anodic scan in O_2. ORR and mass activity values are corrected for a baseline scan under N_2. The ECSA was calculated by integrating the area of the CV curve in the hydrogen under-potential deposition (H_{UPD}) region and using the charge value of 210 $\mu C/cm^2_{Pt}$, corresponding to a monolayer of adsorbed hydrogen atoms on Pt.

Test protocols were as follows. Protocol A: 5000 cycles, 1.0 – 1.5 V, scan rate 500 mV/s. This protocol was tested at 25, 40, 50, and 60°C. CVs in N_2 and ORR activity were recorded at 0, 1000, 3000, and 5000 cycles. Protocol B: 6000 cycles, 1.0 – 1.6 V, scan rate 100 mV/s, tested at 25°C with CVs recorded under N_2 every 1000 cycles and ORR activity recorded at 0, 1000, 2000, and 6000 cycles.

Water vapour sorption analysis was carried out on carbon samples at 40°C using a Quantachrome Hydrosorb-1000. The samples were degassed under vacuum for 18 h at 120°C before analysis. Nitrogen gas sorption data was acquired using a Quantachrome Nova 2000e surface area & pore size analyzer after a degassing at 120°C for minimum 4 hours. X-ray diffraction (XRD) spectroscopy was performed on HSC and VC using a Bruker D8 Advance (Cu-Kα source, 40 kV, 40 mA). Raman spectroscopy was performed on HSC and VC using a HORIBA Scientific LabRAM HR Raman spectrometer system with a 532.4 nm laser and optical microscope at room temperature.

5.3 Results

The MEA baseline to which we compare RDE results was reported originally by Mukundan et al [23]. MEA testing data was collected using a 50 cm^2 standard test cell at Ballard Power Systems, Inc. A potential hold at 1.2 V was used to evaluate the durability of three catalysts supported by HSC, VC, and LSC. The carbon catalyst support materials used in the study by Mukundan are the same as those used in this study, albeit with different Pt loadings. We believe that the differences in these carbons are significant enough that clearly distinct trends in durability should be observable despite differences in the Pt loadings. The absolute ECSAs of each catalyst in the present study are given below. Polarization curves were recorded for each after 0, 20, and 400 hours with the exception of

HSC which was measured after 100 hours instead of 400 due to a more rapid performance drop. The results of the MEA ASTs are shown in Figure 5-1. Each of the catalysts tested shows similar beginning of life (BOL) performance. After a 20 hour potential hold, LSC and VC catalysts remain reasonably stable while HSC catalyst shows a drastic drop in performance. At 100 hours, the performance of HSC has dropped so low as to render a longer potential hold unnecessary. Meanwhile, after 400 hours the performance of the VC drops considerably while LSC shows very little degradation.

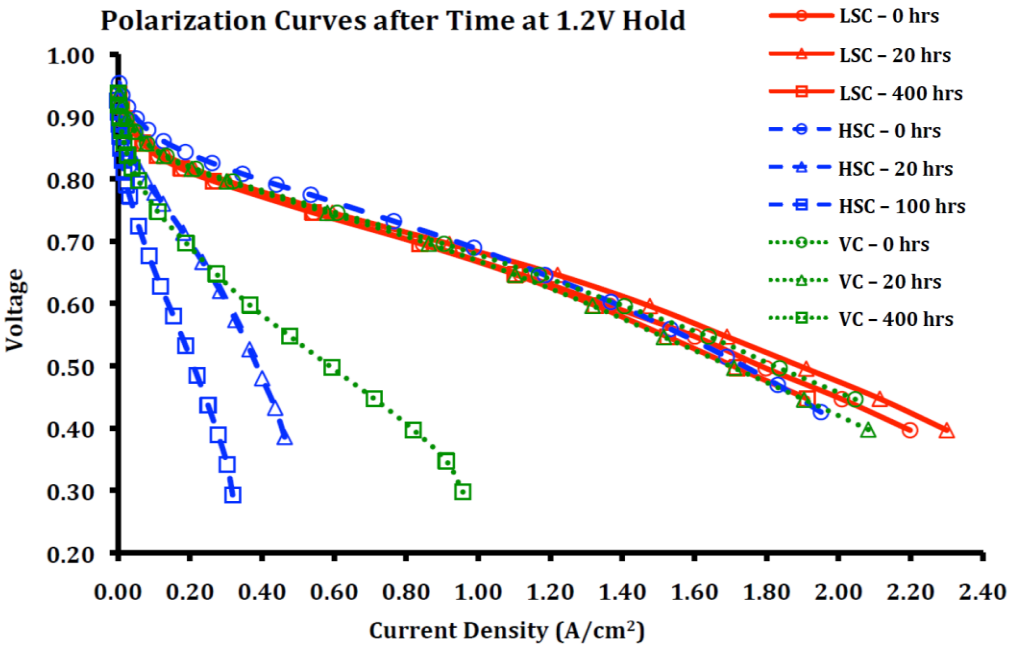

Figure 5-1. Polarization curves for catalysts supported on LSC, VC, and HSC after different hold times at 1.2 V. Tests were carried out using a 50 cm^2 fuel cell with serpentine hardware, operated at 80°C in saturated H_2/N_2 at 150 kPa absolute pressure for 400 hour

The results of the MEA ASTs are not unexpected. The decrease in performance can be correlated to trends in the durability of the carbon support with more stable carbons demonstrating better performance throughout the AST. The apparent durability of the studied catalyst supports, then, is in the order LSC > VC > HSC. These trends in durability are linked to differences in the physical properties of each carbon support, and should be reflected in a well-designed RDE AST protocol.

In order to gain insight into the MEA results, we examined physical differences in the three support carbons being studied using several methods. Water vapour and N_2 sorption analysis was performed to determine their sorption properties and surface area while Raman spectroscopy and X-ray diffraction spectroscopy were used to identify differences in their relative degrees of graphitization. Figure 5-2a shows the N_2 gas sorption isotherm for each of the carbons. The multi-point BET surface areas of HSC, VC, and LSC area are 876, 210, and 149 m^2/g, respectively. Ignoring, for a moment, the effects of hydrophobicity and crystallinity, the surface area and durability of the carbons are expected to be inversely related. The high surface area in HSC lends itself to rapid degradation as there are many potential oxidation sites. In addition to the kinetic losses associated with carbon corrosion, a further loss in performance may also occur due to increased mass transport resistance arising from the collapse and compaction of the carbon support as it oxidizes to CO_2 [23]. This compaction and resulting loss in porosity may be caused by complete oxidation of the carbon to CO_2 which can lead to loss of carbon support material through physical changes to the structure.

The relative hydrophobicity for each of the three carbons was measured using water vapour sorption analysis. A higher affinity for water can improve proton conductivity in real fuel cell systems. However, it also increases the rate of carbon corrosion by oxidation. Increased contact improves water transport which is the source of oxygen for the corrosion reaction [14]. The results of the water vapour sorption analysis are shown in Figure 5-2b. In this case the volume of adsorbed water is normalized to each material's specific surface area. This allows for a direct comparison of the hydrophobicity of each carbon material by removing the variance in surface area. The results clearly show that LSC has the lowest volume of adsorbed water, meaning that it is the most hydrophobic of the three carbons. VC and HSC showed similar hydrophobicity but HSC had the highest adsorbed water content, making it most hydrophilic. Thus, the hydrophobicity increases as HSC < VC < LSC, which matches both the trends in surface area (Figure 5-2a), and durability (Figure 5-1). The hydrophobicity of LSC may be related to its higher degree of graphitization compared to the other two carbons.

XRD and Raman spectroscopy were also done for HSC and VS, and are shown in Figure 5-2(c) and Figure 5-2(d). As shown in Figure 5-2©, the (002) peak and (100) peak are clearly visible for both carbon materials. While the XRD spectra are similar, the (002) peak is broader for the HSC material, which points to less crystallinity compared with VC. Raman spectroscopy is another powerful tool for analyzing carbon samples. The results of Raman analysis on HSC and VC are shown in Figure 5-2(d). The most meaningful range of wavenumbers for carbon black is between 1000 and 1800 $cm^{-1}$where the D-band and G-band appear [24]. For the carbon samples, the D-band occurs around ~1345 cm^{-1} and corresponds to amorphous carbon while the G-band, which appears at ~1580 cm^{-1} corresponds to sp^2 carbon (i.e. more graphitic). Others have examined carbon black using Raman spectroscopy and used the ratio of the integrated intensities of the D and G bands, I_D/I_G, as a measure of the level of crystallinity in the sample [24]. HSC was measured to have a I_D/I_G value of 1.89, with D- and G-band peaks at 1338 and 1585 cm^{-1}, respectively. VC had an I_D/I_G value of 1.83 and D- and G-bands centered at 1347 and 1578cm^{-1}, respectively. The higher an I_D/I_G value in HSC indicates a slightly more disordered carbon, although the values are similar.

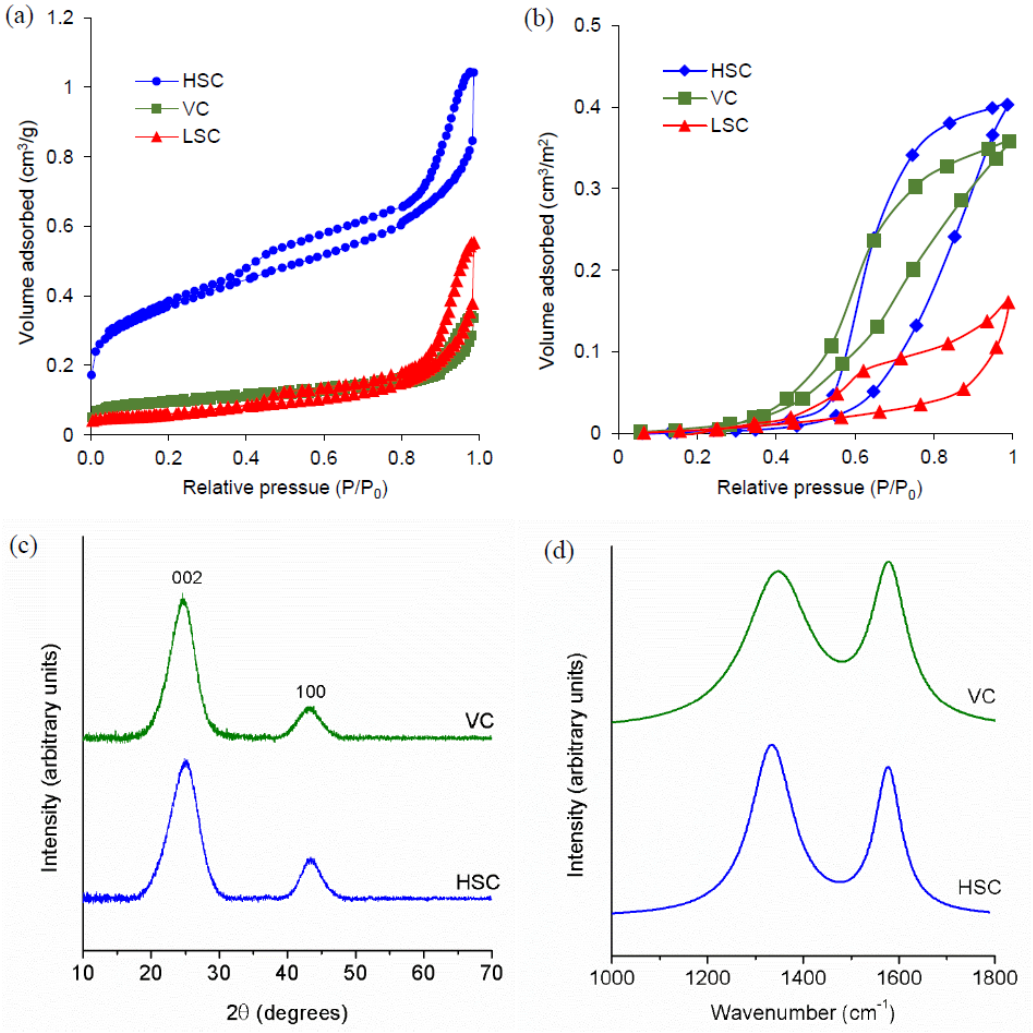

Figure 5-2. (a) Sorption isotherms of H2O (a) and N_2 (b) on HSC, VC, and LSC (exclusive of Pt). (c) XRD and (d) Raman spectra of HSC and VC.

Taken together, the N_2 and H_2O sorption data (Figure 5-2(a) and (b)), XRD data (Figure 5-2(c)) and Raman data (Figure 5-2(d)) clearly explain the in-situ durability trend observed for the three catalysts (Figure 5-1). This is important, as the ultimate goal of this study was to evaluate the ability of RDE ASTs to accurately predict in-situ MEA trends in catalyst durability. Clearly, any reliable RDE AST should demonstrate the following trend in catalyst stability: HSC < VC < LSC.

Many previous studies have used RDE to perform ASTs on carbon supported catalysts for PEMFCs. Some have investigated the effect of potential range on the oxidation of carbon [25], others have used RDE ASTs for potential cycling coupled with

CO_2 monitoring or electron microscopy to investigate the support corrosion [26], [27]. Very recently, a protocol comparable to one used in this study has been used to compare HSC with a ceramic catalyst support to highlight the excellent durability of the latter [28]. The AST protocols selected for this work were suggested by the US Department of Energy [22], and will herein be referred to as protocol A and protocol B. Protocol A consists of cycling under N_2 from 1.0–1.5 V vs. RHE at 500 mV/s for 5000 cycles at 60°C. Protocol B consists of cycling under N_2 from 1.0–1.6 V vs. RHE at 100 mV/s for 6000 cycles at 25°C. The former is done at elevated temperature, but with a lower upper potential limit (UPL) of 1.5 V compared to a UPL of 1.6 V in the protocol B. The two protocols are alternatives, with one requiring a single 8-hour working day (protocol A), and one which takes roughly 24 hours to complete (protocol B). The chosen potential range above 1.0 V prevents the reduction of formed Pt oxide, minimizing the effect of Pt dissolution caused by repeated redox reactions, and isolating the effects of carbon corrosion [29]. Although others have shown the presence of Pt to enhance carbon oxidation in PEMFCs [8], [30], the carbon materials in this study are significantly different, as seen in the physical characterization data, to reliably illustrate the different trends seen during in-situ durability studies.

Using protocol A, we first tested the durability of each carbon at 25°C. The CVs obtained for Pt/HSC at 0, 1000, 3000, and 5000 cycles are shown in Figure 5-3(a). As is clear, there is almost no change in the CV curves before and after the AST at 25°C. The initial ECSA values of Pt/HSC, Pt/VC, and Pt/LSC at 25°C were 75.1, 39.6, and 45.5 m^2/g, respectively. These values very closely agree with those reported for the catalysts tested in Figure 5-1. (HSC: 74 m^2/g, LSC: 44 m^2/g, VC: not explicitly stated). The inset in Figure 5-3(a) shows a highlight of the capacitive double layer region from roughly 0.4 –0.6 V for the 25°C AST. Even with this expanded view there is very little change seen in the curves, suggesting good support durability. This result is surprising, given that HSC demonstrated rapid performance loss in MEA testing. It is apparent from the results of the AST that, at 25°C, this protocol is not aggressive enough to accurately reproduce the results seen in-situ. In order to improve the predictive capabilities of the AST, we repeated protocol A at 60°C; the CV curves from this test are shown in Figure 5-3b. There is considerably more degradation of the carbon sample at 60°C than at 25°C, as seen in the change in CV curves

with cycling. The HUPD region from roughly 0.05–0.4 V decreases in size with cycling especially for the 60°C AST, pointing to a decreasing ECSA. The inset in Figure 5-3b highlights the capacitive double layer region for the 60°C case, showing notable changes in the double layer capacitance. At the elevated temperature, the double layer capacitance increases from 0 to 1000 to 3000 cycles, finally decreasing at 5000 cycles. The increase in the double layer charging current is likely due to both an increase in the pseudo-capacitive groups on the surface of the carbon, as well as an increase in the carbon surface area, which may arise due to the creation of micropores as CO_2 is formed. After 5000 cycles the double layer appears to have reduced, which may indicate the removal of surface species and loss of carbon material. Indeed, it has been previously reported that severe oxidation may result in some surface species being removed, hence lowering the columbic charge in the double layer region [7]. The changes in the double layer region for the 60°C AST reflect the extreme degradation seen in MEA testing for HSC.

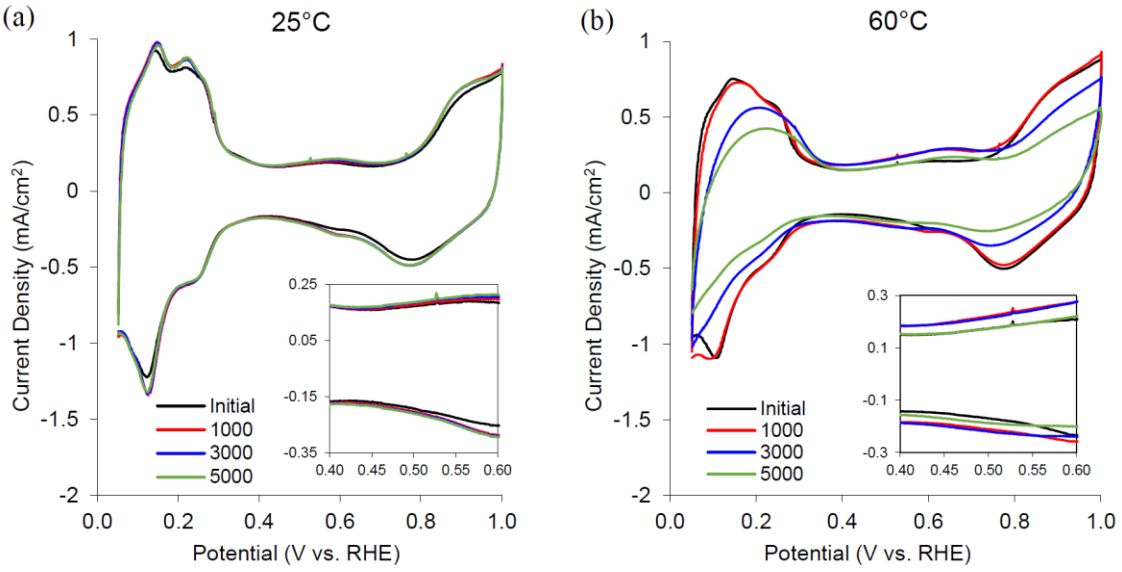

Figure 5-3. Cyclic voltammograms of HSC catalyst at different cycles for (a) 25°C and (b) 60°C. Cycling at 500 mV/s from 1.0 – 1.5 V vs. RHE in 0.09 M H2SO4.

Pt/VC and Pt/LSC were also tested using protocol A at 25°C and 60°C, and their ECSA values are plotted, along with those of Pt/HSC, in Figure 5-4. For the AST at 25°C, Pt/LSC, Pt/VC, and Pt/HSC each retains 96% of their original ESCA after testing. This result is surprising and clearly not in agreement with MEA data. When the same protocol

is carried out at 60°C, the ECSA values drop from their original value to 91%, 61%, and 44% for Pt/LSC, Pt/VC, and Pt/HSC after cycling. This trend of degradation matches much more closely to that seen in the MEA data. These results indicate a strong dependence on testing temperature for AST RDE protocols.

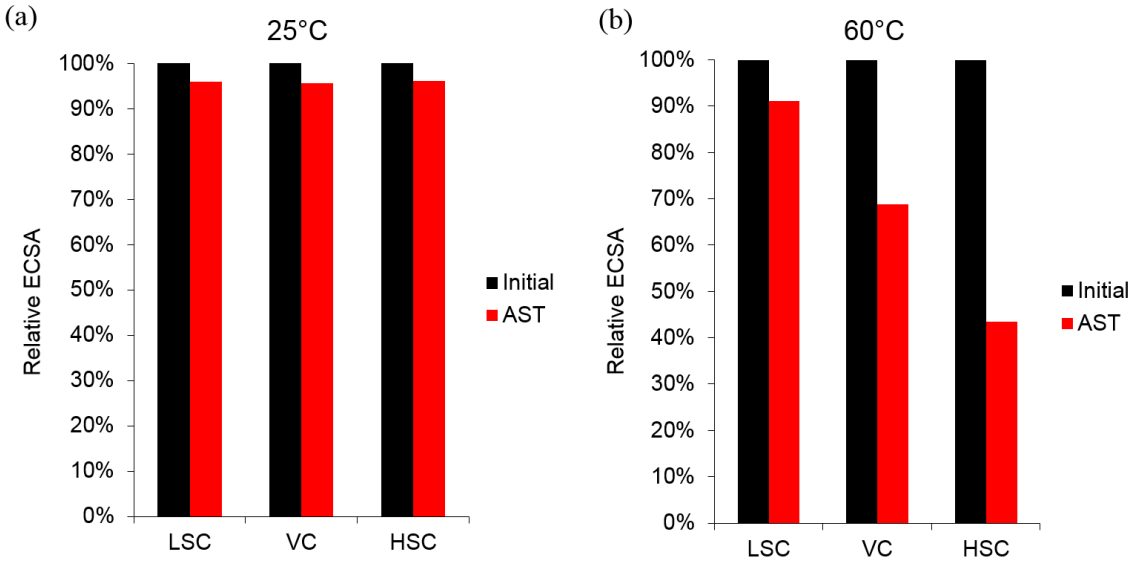

Figure 5-4. Calculated ECSA at BOL and after 5000 cycles for catalysts on HSC, VC, and LSC at 25°C (a) and 60°C (b). 5000 cycles at 500 mV/s from 1.0 – 1.5 V vs. RHE in 0.09 M H2SO4.

To further examine the influence of temperature on carbon corrosion during ASTs, protocol A was done using Pt/HSC at several temperatures between 25 and 60°C. The results of these tests are shown in Figure 5-5. There is a clear trend of decreasing ECSA and mass activity with increasing temperature after the AST. After 5000 cycles the ECSA decreases from initial values to 91%, 79%, 70%, and 44% for tests at 25, 40, 50, and 60°C, respectively. Mass activity shows a similar trend with post-AST activities of 88%, 68%, 61%, and 44% of initial values for the 25, 40, 50, and 60°C tests, respectively. We have found that at 25°C the AST does not accurately predict the in-situ MEA data. This suggests the need for elevated temperature, or a more aggressive AST protocol when using ambient temperature, in order to accurately represent in-situ PEMFC degradation.

While performing protocol A at 60°C does appear to reliably predict in-situ MEA trends in catalyst stability, it is desirable to have an RDE AST protocol that can be run at room temperature. This is because many RDE electrodes cannot be used at temperatures >25°C. Protocol B uses a lower scan rate of 100 mV/s and is carried out at 25°C, with an UPL of 1.6 V. For Pt/HSC, the ESCA value recorded after 4000 cycles is just 17% of the original, and after the full 6000 cycles, the carbon has degraded so much that calculation of the ESCA from the CV curve double layer region is not meaningful. Furthermore, the mass activity for Pt/HSC dropped by 75% after this AST. Meanwhile, for Pt/LSC, reasonably good durability is seen with ESCA values at 4000 and 6000 cycles of 90% and 86% of the original, respectively. Pt/LSC exhibited a reduction in mass activity of 34% after AST. Importantly, the results of these tests align well with in-situ MEA data for the HSC and LSC supported catalysts.

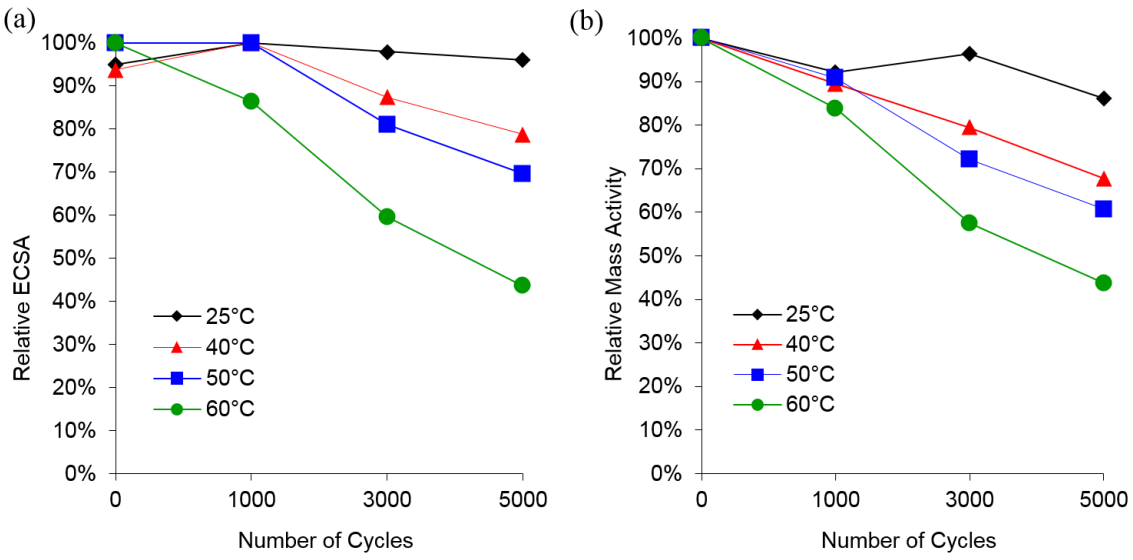

Figure 5-5. ECSA (a) and mass activity (b) after AST cycling at 25, 40, 50, and 60°C for Pt/HSC. Cycling at 500 mV/s from 1.0 – 1.5 V vs. RHE in 0.09 M H_2SO_4.

The two protocols originally suggested have different UPL and different scan rates. Both parameters can affect the outcome of an AST. Figure 5-6 shows the ECSA (a) and MA (b) of Pt/HSC tested at 25°C by a modified protocol A with UPL of 1.6 V, rather than 1.5 V, and protocol B. The modified Protocol A, with scan rate of 500 mV/s and 5000 cycles has a total cycling time of 200 minutes. Protocol B has a scan rate of 100 mV/s and

6000 cycles for a total cycling time of 1200 minutes. It is clear from Figure 5-6 that the longer, slower AST is considerably more aggressive on the carbon supported catalysts. For protocol B, the hydrogen adsorption region became almost negligible beyond 4000 cycles so that no ECSA values could be reported. If we examine the ECSAs after the first 200 minutes it appears that the faster scan rate of protocol A is more aggressive. After 200 minutes, the ECSA of Pt/HSC drops to 83%, having cycled 5000 times at 500 mV/s. During the same time in protocol B, having only completed 1000 cycles at 100 mV/s, the ESCA of Pt/HSC remains unchanged. We can say, then, that a faster scan rate and increased cycle number is more aggressive, if the total test time is kept constant. However, for a given number of cycles, a slower scan rate of 100 mV/s and correspondingly longer time is drastically more aggressive than a high scan rate or 500 mV/s with less total test time. This can be explained by the amount of time spent at high potentials between 1.0-1.6 V where carbon oxidation is favourable. These results imply that time spent holding the catalyst in this potential range is more effective in corroding the carbon support than repeated, rapid cycling. Each of these test protocols was also performed on Pt/LSC with minimal degradation noted. Even with a UPL of 1.6 V, the more accelerated, high scan rate protocol does not produce the same trend of degradation as seen in the MEA data or in the 60°C test with UPL of 1.5 V.

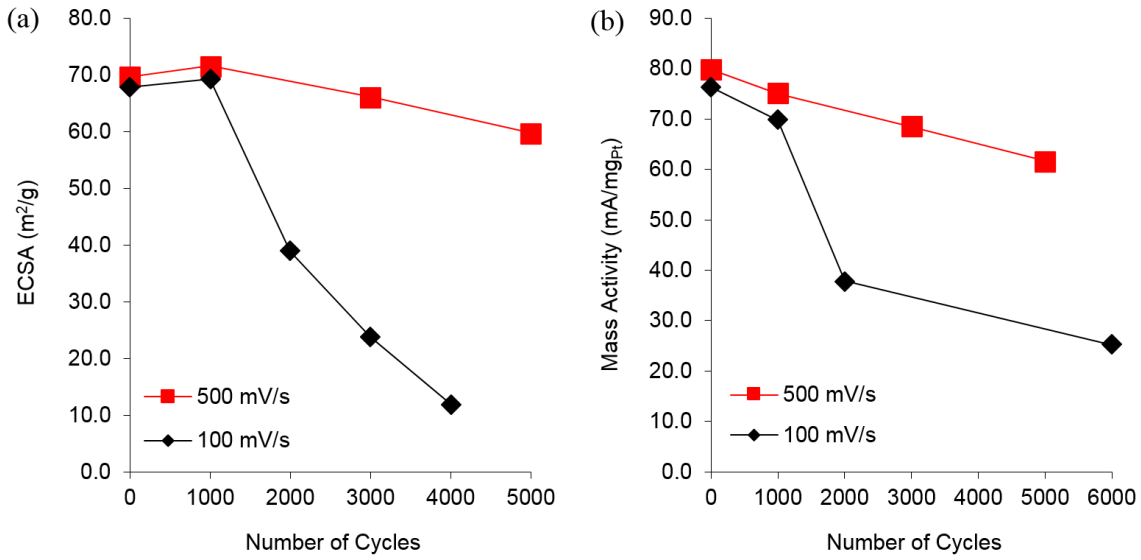

Figure 5-6. ECSA (a) and mass activity (b) of HSC catalyst at 25°C, cycling from 1.0 – 1.6 V vs RHE at 100 mV/s and 500 mV/s, respectively.

The importance of temperature, scan rate, and total scanning time has been discussed. In terms of reproducing the support corrosion data seen in MEA testing, protocol A is appropriate only when used at elevated temperature (60°C) and not at room temperature. Protocol B reproduces the results from the MEA testing well. While the comparison with the MEA data is only qualitative, it is the trend in support degradation that is of importance. This study may be useful for further development of RDE ASTs not only for carbon corrosion but for overall catalyst degradation. When selecting AST parameters, careful consideration should be given to temperature, potential window, scan rate, UPL, and total scanning time. This study highlights the need for efforts towards standardized RDE testing and ensuring that the technique is accurately representing real PEMFC data.

5.4 Conclusions

AST protocols designed to study catalyst support corrosion by RDE were evaluated using three representative carbon types which have been well studied in previous literature. The objective of this study is to bring to attention the drastic inconsistencies between MEA (in-situ) and RDE (ex-situ) carbon durability data that may arise if the RDE protocol is not

carefully considered. As there are many AST protocols being used by various labs, it is worth highlighting this potential difference as the trends observed from RDE data may not accurately represent the durability of catalyst supports in real fuel cell systems. This is especially important for screening catalyst support materials which are likely much more similar than those studied here. It was determined that for protocol A, 5000 cycles from 1.0-1.5 V at 500 mV/s, elevated temperature of 60°C is necessary to reproduce the degradation observed in MEA tests. When performed at 25°C, this particular AST showed no noticeable signs of degradation to an HSC supported catalyst which is otherwise known to have poor durability. Thus, temperature is shown to have a considerable effect on the durability of carbon supports during RDE ASTs. Protocol B (6000 cycles from 1.0-1.6 V at 100 mV/s) results in carbon corrosion data which agrees well with MEA data even when performed at room temperature. Additionally, potential scan rate is also shown to affect support durability protocols insofar as they result in longer exposure to high potentials, which accelerates corrosion. The drastic differences in end of test ECSAs and activities following these ASTs provide further evidence that carbon support durability is critical to overall catalyst durability. Importantly, it is found that not all RDE AST protocols can accurately represent the durability of carbon supports in fuel cell systems. Hence, a careful selection of parameters is needed to produce meaningful results via the RDE method.

5.5 References

[1] P. J. Ferreira, G. J. la O', Y. Shao-Horn, D. Morgan, R. Makharia, S. Kocha, and H. a. Gasteiger, "Instability of Pt/C Electrocatalysts in Proton Exchange Membrane Fuel Cells," *J. Electrochem. Soc.*, vol. 152, no. 11, p. A2256, 2005.

[2] J. Zhang, Ed., *PEM Fuel Cell Electrocatalysts and Catalyst Layers*. London: Springer London, 2008.

[3] X. Yu and S. Ye, "Recent advances in activity and durability enhancement of Pt/C catalytic cathode in PEMFC," *J. Power Sources*, vol. 172, no. 1, pp. 145–154, Oct. 2007.

[4] L. M. Roen, C. H. Paik, and T. D. Jarvi, "Electrocatalytic Corrosion of Carbon Support in PEMFC Cathodes," *Electrochem. Solid-State Lett.*, vol. 7, no. 1, p. A19, 2004.

[5] S. Swathirajan and B. Merzougui, "Rotating Disk Electrode Investigations of Fuel Cell Catalyst Degradation Due to Potential Cycling in Acid Electrolyte," in *ECS Transactions*, 2007, vol. 2, no. 8, pp. 21–36.

[6] J. Thomas, "Reactivity of carbon: some current problems and trends," *Carbon N. Y.*, vol. 8, no. 4, pp. 413–421, 1970.

[7] K. Kinoshita and J. Bett, "Potentiodynamic analysis of surface oxides on carbon blacks," *Carbon N. Y.*, vol. 11, pp. 403–411, 1973.

[8] K. Kinoshita and J. a. S. Bett, "Determination of carbon surface oxides on platinum-catalyzed carbon," *Carbon N. Y.*, vol. 12, no. 5, pp. 525–533, Oct. 1974.

[9] D. Lowde, J. Williams, and B. McNicol, "The characterisation of catalyst surfaces by cyclic voltammetry," *Appl. Surf. Sci.*, vol. 1, pp. 215–240, 1978.

[10] J. Willsau and J. Heitbaum, "The influence of Pt-activation on the corrosion of carbon in gas diffusion electrodes—A dems study," *J. Electroanal. Chem. Interfacial Electrochem.*, vol. 161, no. 1, pp. 93–101, Feb. 1984.

[11] H. Boehm, "Some aspects of the surface chemistry of carbon blacks and other carbons," *Carbon N. Y.*, vol. 32, no. 5, pp. 759–769, 1994.

[12] F. Rodríguez-reinoso, "The role of carbon materials in heterogeneous catalysis," *Carbon N. Y.*, vol. 36, no. 3, pp. 159–175, Jan. 1998.

[13] M. Tarasevich, V. A. Bogdanovskaya, and N. M. Zagudaeva, "Redox reactions of quinones on carbon materials," *J. Electroanal. Chem. Interfacial Electrochem.*, vol. 223, no. 1–2, pp. 161–169, May 1987.

[14] K. H. Kangasniemi, D. a. Condit, and T. D. Jarvi, "Characterization of Vulcan Electrochemically Oxidized under Simulated PEM Fuel Cell Conditions," *J. Electrochem. Soc.*, vol. 151, no. 4, p. E125, 2004.

[15] S. Maass, F. Finsterwalder, G. Frank, R. Hartmann, and C. Merten, "Carbon support oxidation in PEM fuel cell cathodes," *J. Power Sources*, vol. 176, no. 2, pp. 444–451, Feb. 2008.

[16] M. K. Debe, "Electrocatalyst approaches and challenges for automotive fuel cells.," *Nature*, vol. 486, no. 7401, pp. 43–51, Jun. 2012.

[17] Y. Garsany, J. Ge, J. St-Pierre, R. Rocheleau, and K. E. Swider-Lyons, "Analytical Procedure for Accurate Comparison of Rotating Disk Electrode Results for the Oxygen Reduction Activity of Pt/C," *J. Electrochem. Soc.*, vol. 161, no. 5, pp. F628–F640, Mar. 2014.

[18] Y. Garsany, J. Ge, J. St-Pierre, R. Rocheleau, and K. Swider-Lyons, "Standardizing Thin-Film Rotating Disk Electrode Measurements of the Oxygen Reduction Activity of Pt/C," *ECS Trans.*, vol. 58, no. 1, pp. 3–14, Oct. 2013.

[19] Y. Garsany, O. a Baturina, K. E. Swider-Lyons, and S. S. Kocha, "Experimental methods for quantifying the activity of platinum electrocatalysts for the oxygen reduction reaction.," *Anal. Chem.*, vol. 82, no. 15, pp. 6321–8, Aug. 2010.

[20] S. Kocha, "Best Practices and Benchmark Activities for ORR Measurements by the Rotating Disk Electrode Technique," *Natl. Renew. Energy Labs*, vol. Dept. of E, 2014.

[21] S. S. Kocha, J. W. Zack, S. M. Alia, K. C. Neyerlin, and B. S. Pivovar, "Influence of Ink Composition on the Electrochemical Properties of Pt/C Electrocatalysts," *ECS Trans.*, vol. 50, no. 2, pp. 1475–1485, Mar. 2013.

[22] S. S. Kocha, Y. Garsany, and D. Myers, "Testing Oxygen Reduction Reaction Activity with the Rotating Disc Electrode Technique," *DOE Webinar*, 2013.

[23] R. Mukundan, G. James, D. Ayotte, J. R. Davey, D. Langlois, D. Spernjak, D. Torraco, S. Balasubramanian, A. Z. Weber, K. L. More, and R. L. Borup, "Accelerated Testing of Carbon Corrosion and Membrane Degradation in PEM Fuel Cells," *ECS Trans.*, vol. 50, no. 2, pp. 1003–1010, Mar. 2013.

[24] T. Jawhari, A. Roid, and J. Casado, "Raman spectroscopic characterization of some commercially available carbon black materials," *Carbon N. Y.*, vol. 33, no. 11, pp. 1561–1565, Jan. 1995.

[25] H.-S. Choo, T. Kinumoto, M. Nose, K. Miyazaki, T. Abe, and Z. Ogumi, "Electrochemical oxidation of highly oriented pyrolytic graphite during potential cycling in sulfuric acid solution," *J. Power Sources*, vol. 185, no. 2, pp. 740–746, Dec. 2008.

[26] H. R. Colón-Mercado, H. Kim, and B. N. Popov, "Durability study of Pt3Ni1 catalysts as cathode in PEM fuel cells," *Electrochem. commun.*, vol. 6, pp. 795–799, 2004.

[27] F. Xu, M. Wang, Q. Liu, H. Sun, S. Simonson, N. Ogbeifun, E. a. Stach, and J. Xie, "Investigation of the Carbon Corrosion Process for Polymer Electrolyte Fuel Cells Using a Rotating Disk Electrode Technique," *J. Electrochem. Soc.*, vol. 157, p. B1138, 2010.

[28] J. Parrondo, T. Han, E. Niangar, C. Wang, N. Dale, K. Adjemian, and V. Ramani, "Platinum supported on titanium-ruthenium oxide is a remarkably stable electrocatayst for hydrogen fuel cell vehicles.," *Proc. Natl. Acad. Sci. U. S. A.*, vol. 111, no. 1, pp. 45–50, Jan. 2014.

[29] J. Wang, G. Yin, Y. Shao, S. Zhang, Z. Wang, and Y. Gao, "Effect of carbon black support corrosion on the durability of Pt/C catalyst," *J. Power Sources*, vol. 171, no. 2, pp. 331–339, Sep. 2007.

[30] E. Passalacqua, P. L. Antonucci, M. Vivaldi, A. Patti, V. Antonucci, N. Giordano, and K. Kinoshita, "The influence of Pt on the electrooxidation behaviour of carbon in phosphoric acid," *Electrochimica Acta*, vol. 37. pp. 2725–2730, 1992.

6 Conclusions & Outlook

This thesis includes three original research articles (chapters 3-5) related to carbon nanomaterials and their use as FC catalysts and supports. The first is a study of co-doped CNTs with nitrogen and phosphorus, with physical properties and electrochemical activity compared to nitrogen doped CNTs. The second report examines two methods for treating commercial carbon black, with ammonia or ozone, in order to improve its properties as a Pt support. The final study is an evaluation of the effectiveness of two AST protocols. The goal of this was to determine whether these ASTs done in a half-cell configuration could reliably predict the degradation phenomena seen in real FC MEAs.

It was found that phosphorus could be successfully introduced into CNTs by a one-step CVD method for growth and doping of PNCNTs, using TPP as a precursor. Variation of the carrier gas flow rate used for CVD showed increased yield at higher flows and a dependence on the nanotube diameter was seen with changing TPP concentration. P concentration of 1 at.% was found, along with 6.2% nitrogen, which was the same concentration found in NCNTs. Further, the ratio of pyrrolic to pyridinic N was higher in the PNCNT sample, suggesting that the presence of P may influence N doping. PNCNTs showed a higher degree of disorder in the carbon compared to NCNTs, as well as increased wall thickness with relatively narrow channels. Electrochemical tests showed that PNCNTs have a 62% higher current density in the kinetic region (taken at 0.8 V vs RHE) compared to NCNTs and Koutecky-Levich analysis suggest a mixed 2 and 4 electron transfer process for the ORR catalyzed by PNCNTs.

In the 4th chapter, CB with either ammonia treatment (NH3-CB) or ozone treatment (O3-CB) are compared to untreated CB for use as a Pt support. Physical characterization of the carbons before Pt deposition show an increased in surface area for NH3-CB, and a slight decrease in surface area but increase in pore size for O3-CB. Surface N and O concentrations of 0.7 at% and 2.4 at.% were found on NH3-CB and O3-CB, respectively, compared to N and O concentrations of 0.1 and 1.4 at.% for CB. The particle size of Pt deposited by microwave assisted polyol method decreased in the order Pt/CB > Pt/O3-CB > Pt/NH3-CB and is attributed to acidic surface groups in O3-CB and increased surface

area and nitrogen active sites in NH3-CB. XANES analysis suggested some electronic interactions between the Pt and O3-CB support, which was not seen in either of the other two supports. ORR testing by RDE revealed that mass activity increased in the order Pt/CB < Pt/NH3-CB < Pt/O3-CB and durability cycling tests in the Pt-dissolution range showed good retention of ECSA, particle size, and mass activity for Pt/O3-CB compared to Pt/NH3-CB and Pt/CB. This is attributed to the functional groups and surface homogeneity, plus modified electronic structure of Pt, on the ozone treated CB. Pt/NH3-CB showed no considerable improvement in stability after AST compared to untreated CB. Thus, ALD ozone treatment of the commercial carbon black is shown to increase ORR activity, and improve Pt particle stability compared to an untreated CB support.

Finally, the third report of this thesis highlights several important considerations for performing accelerated durability tests using RDE. Two protocols were proposed by the DOE for studying carbon corrosion: protocol A (5000 cycles, 1.0-1.5 V, 0.5 V/s) and protocol B (6000 cycles, 1.0-1.6 V, 0.1 V/s). Using three well known carbon black supports it was shown that protocol A was unsuitable for predicting MEA degradation patterns when used at room temperature, but was suitable at 60°C. At room temperature, protocol A resulted in no observable loss in ECSA for a catalyst supported on high surface area carbon which is well known to have poor corrosion resistance. Additionally, a clear temperature dependence was shown for the protocol A when measured at several temperatures from 30-60°C. Protocol B appeared to match the MEA durability data well. Scan rate was seen to affect AST results as longer time spent at high potentials (above 1.0 V) results in more carbon corrosion. The results of the study are important because they highlight the need to carefully choose the parameters of RDE AST protocols. A number of factors should be considered including temperature, scan rate, and upper potential limit. RDE ASTs are frequently used in catalyst research to compared durability of catalysts, though their goal should also be to predict trends in durability that will be true at the MEA level. Thus, they need to be accurately benchmarked and planned.

The three studies in the thesis share a common theme of nanoscale carbon support materials for fuel cells. The first study addresses the long-term goal of metal-free catalysts where the co-doped PNCNTs are themselves the catalysts. For the second study, the

research shifted slightly towards more industrially relevant solutions, offering a potential for improved catalyst activity and durability after a low-cost, one-step carbon pre-treatment. The last study was carried out entirely at Ballard Power Systems under direction of the scientific team there. That research is important for the community in terms of understanding the need for robust testing protocols for RDE durability studies, and furthered my own experience with carbon corrosion and included investigating state-of-the-art catalyst support materials. Taken together, my research suggests that modified carbon nanomaterials show tremendous promise for increasingly functional FC catalyst supports. As a Pt support and as metal-free catalyst, doping and functionalization of nanostructured carbon endows these already exciting materials with even more remarkable properties. Further, this research supports ongoing efforts towards standardizing RDE protocols for rapid catalyst evaluation by highlighting the need for carefully chosen parameters to produce results that reasonably represent MEA-level behavior.

6.1 Future work

Further work in this field could take many forms. Regarding the study of co-doped phosphorus and nitrogen CNTs there are several logical next steps that could be pursued. One is to test their ORR activity in acidic media, which would provide an indication of their usefulness in PEM fuel cells. Though it is expected that this activity will be extremely low compared to any Pt-containing catalyst, it would be interesting to see if the reaction proceed more quickly than on pristine CNTs or NCNTs. A more promising path for potential commercial use would be to compare NCNTs and PNCNTs as Pt nanoparticle supports. NCNTs are known to provide good ORR enhancement and stability, compared to CNTs. Certainly, examining the effect of added phosphorus dopants on the deposition of Pt particles and comparing the ORR activity and durability to Pt/NCNTs would be both novel and of considerable interest. Of course, RRDE studies can also elucidate more information on the nature of the ORR mechanism on PNCNTs.

Obvious next steps for the pre-treated carbon black would be an optimization of the ozone treatment to produce the best ORR activity and reasonable durability. For

thoroughness a comparison between ALD ozone treatment and a high-temperature gas phase ozone treatment would be interesting, from the perspective of its effects on the carbon black and on any resulting differences in the Pt supporting properties or catalytic activity. Regarding the carbon corrosion AST study, a comprehensive study could be done using 2-3 protocols at the MEA level and 2-3 protocols by RDE and evaluating their comparability and whether they can be repeated at difference facilities. As stated in the introduction section, several researchers at the US DOE and some national labs have already begun the process of benchmarking the most common catalyst materials with rigorous standards and ensuring their repeatability. Any further work towards this goal would be welcomed by academia and industry alike.

Looking ahead, the long term goals for fuel cells dictate that either ultra-low Pt-group metal (PGM) content, or PGM free catalysts will be needed to make FCs affordable at high volume manufacturing levels. Several strategies for achieving this via core-shell and alloyed catalysts seem to show good potential. Re-thinking the electrode structure is another area for potentially break-through research. 3M did this years ago with their nanostructure thin-film architecture. Combining the novel alloys or catalyst materials structures with emerging synthesis and fabrication techniques such as ALD may also prove highly successful. ALD has shown potential already in terms of synthesizing single-atom catalyst materials. As the tools for manipulating and controlling nanoscale materials continue to improve and become more commonplace, synergistic approaches to preparation of the catalyst structure and MEA as a whole may lead to improved FC performance and reduced manufacturing costs.

Several of the world's largest automakers have already deployed their first generation FC vehicles in places like California, Japan, and Europe. As the number of FC vehicles increases and the hydrogen infrastructure grows to support them, the development of high performance and low cost FC catalysts will become even more urgent. Whatever form the catalyst takes in the long term, FCs are poised to become an important part of the energy spectrum. Combined heat and power options, quiet operation, and clean, renewable fuel make the FCs attractive for providing future energy solutions with a high level of resilience.

Permissions

Guidelines for Use of Materials from ECS Publications

Before using ECS material or requesting to reproduce ECS material, please see the ECS Transfer of Copyright Form for the rights retained by authors and employers. **For example, authors may use their own tables and figures in other scholarly research papers that they write, without writing to ECS for permission.** Full credit to the original source should be given, for example, "Reproduced with permission from *J. Electrochem. Soc.*, **150**, H205 (2003). Copyright 2003, The Electrochemical Society." Permission is not needed if figures and/or tables from one ECS publication will be reused in another forthcoming ECS publication.

TRANSFER OF COPYRIGHT AGREEMENT (revised September 2005)

The Electrochemical Society (ECS)
65 South Main Street, Pennington, NJ 08534-2839, USA
Fax: 1.609.730.0629

Thank you for submitting your Work for publication. In order to expedite the publishing process and enable ECS to disseminate your work to the fullest extent, we need to have this Agreement signed and returned to us as soon as possible. If the Work is not accepted for publication this Agreement shall be null and void.

Article entitled (the "Work"): _____

_____ ECS System Tracking # _____

Submitted by the following author(s) (list all authors) ("Author(s)"): _____

_____

for publication in (check one):

❑ *Interface* ❑ *ECS Transactions* ❑ *Journal of The Electrochemical Society* (JES) ❑ *ECS Journal of Solid State Science and Technology* (JSS)

❑ *Electrochemical and Solid-State Letters* (ESL) ❑ *ECS Electrochemistry Letters* (EEL) ❑ *ECS Solid State Letters* (SSL)

1. **Transfer** — In consideration of ECS agreeing to publish the Work, the Authors grant to ECS for the full term of copyright in the Work and any extensions to the term, the exclusive right to (a) publish, reproduce, distribute, display, and store the Work in all forms, formats, and media now known or later developed (including without limitation in print, digital, and electronic form) throughout the world; (b) translate the Work into other languages, create adaptations, summaries or extracts of the Work or other derivative works based on the Work and exercise all of the rights set forth in (a) above in such translations, adaptations, summaries, extracts, and derivative works; and (c) license others to do any or all of the above. All accepted Works become the property of ECS and may not be published elsewhere without prior written permission of ECS, except as noted in Section 2 below.
2. **Rights of Authors** — The Author(s), and in the case of a Work Made for Hire as defined in the U.S. Copyright Code, 17 U.S.C. §101, the employer named below, shall retain the following nonexclusive rights (the "Author Rights"):
   a. All other proprietary rights not transferred to ECS, such as patent rights.
   b. The nonexclusive right, after publication by ECS, to give permission to third parties to republish print versions of the Article or a translation thereof, or excerpts therefrom, without obtaining permission from ECS, provided the ECS-formatted version is not used for this purpose and provided the Article is not to be published in another journal. If the ECS version is used, permission from ECS must be obtained.
   c. The right, after publication by ECS, to use all or part of the Article without revision or modification, including the ECS-formatted version, in print compilations or other print publications of the author(s)' and/or the employer's own works, and on the author(s)' and/or the employer's website, and to make copies of all or part of the Article for the author(s)' and/or the employer's use for lecture or classroom purposes; provided that the copyright notices are not removed and provided that copies are not offered for sale and are not distributed in a commercial way outside of Author(s)'s employing institution.
   d. The right to post and update the Article on e-print servers as long as files prepared and/or formatted by ECS or its vendors are not used for that purpose. Any such posting made or updated after acceptance of the Article for publication shall include a link to the online abstract in the ECS publication of origin or to the entry page of that publication.
   e. If the Article was prepared under a U.S. Government contract, the government shall have the rights under the copyright to the extent required by the contract.

Curriculum Vitae

Name: Adam Riese

Post-secondary Education and Degrees
B.A.Sc., (Honors) Nanotechnology Engineering
University of Waterloo
Waterloo, Ontario, Canada
2008-2013

Honours and Awards:
Queen Elizabeth II Graduate Scholarship in Science & Technology (formerly OGS)
2014-2015

Western University Graduate Scholarship
2013-2015

NSERC Undergraduate Student Research Award
Process Research Ortech
2011

University of Waterloo President's Scholarship
2008

Related Work Experience:
Teaching Assistant
The University of Western Ontario
09/2013 – 04/2015

Catalyst R&D Co-op
Ballard Power Systems, Inc.
Burnaby, Canada. V5J 5J8
05/2015 – 08/2015

Publications:
A. Riese, D. Banham, S. Ye, and X. Sun, "Accelerated Stress Testing by Rotating Disk Electrode for Carbon Corrosion in Fuel Cell Catalyst Supports," *J. Electrochem. Soc.*, 162 (7), F783-F788.

S. Lawes, **A. Riese**, Q. Sun, N. Cheng, and X. Sun, "Printing nanostructured carbon for energy storage and conversion applications," *Carbon N. Y.*, 92, 150-176

N. Cheng, M. Norouzi Banis, J. Liu, **A. Riese**, S. Mu, R. Li, T.-K. Sham, and X. Sun, "Atomic scale enhancement of metal–support

interactions between Pt and ZrC for highly stable electrocatalysts," *Energy Environ. Sci.*, 8 (5), 1450-1455

N. Cheng, M. N. Banis, J. Liu, **A. Riese**, X. Li, R. Li, S. Ye, S. Knights, and X. Sun, "Extremely Stable Platinum Nanoparticles Encapsulated in a Zirconia Nanocage by Area-Selective Atomic Layer Deposition for the Oxygen Reduction Reaction," *Adv. Mater.*, 27 (2), 277-281

Memberships: Professional Engineers Ontario
Ontario Society of Professional Engineers
Chemical Institute of Canada